UNIVERSITY OF STRATHCLYDE
DEPARTMENT OF PHYSICS

Ion acceleration in ultra-thin foils undergoing relativistically induced transparency

by

Haydn W. Powell

in partial fulfilment of the requirements for the degree of Doctor of Philosophy in Physics

2015

Copyright Declaration

Signed:

Date:

Abstract

This thesis reports on experimental and numerical investigations of ion acceleration and the underlying mechanisms of energy transfer in the interaction of intense laser pulses with ultra-thin foils undergoing relativistic induced transparency. The optimisation and optical control of the ion beam properties including the beam flux, maximum energy and energy spread is important for the development of applications of laser-driven ion beams.

Multiple laser-ion acceleration mechanisms, driven by sheath fields, radiation pressure and transparency enhancement occur in intense laser pulse interactions with an ultra-thin foil. This is experimentally and numerically demonstrated in the work presented in this thesis. Results from an experimental investigation of ion acceleration from ultra-thin (nanometer-thick) foils using the Vulcan petawatt laser facility are presented. Spatially separating the multiple beam components arising from the differing acceleration mechanisms enables the underlying physics of the individual mechanisms to be investigated.

In the case of foils undergoing relativistic induced transparency, it is shown that an extended channel and resulting jet is formed in the expanding plasma at the rear of the target, resulting in higher laser energy absorption into electrons and enhanced ion acceleration in a localised region. This results from volumetric heating of electrons by the laser pulse propagating within the channel. The measured maximum energy of the protons in the enhanced region of the jet is found to be highly sensitive to the laser pulse contrast and rising edge intensity profile of the laser. It is shown, using a controlled pre-expansion of the target, that an increase in the maximum proton energy by a factor two is achievable.

Numerical investigations of the interaction, using particle-in-cell (PIC) simu-

lations, show that an idealised sharp rising edge Gaussian laser intensity profile produces the highest proton energy, though this condition could not be achieved experimentally. The simulations show that controlled pre-expansion of the target, by variation of the rising edge intensity profile, enables better conditions for channel formation and energy coupling to electrons and thus protons.

A detailed numerical (PIC) investigation of the mechanisms of laser energy transfer to electrons and ions in thin foils undergoing relativistically induced transparency is also presented. The role of streaming instabilities in the transfer of energy between particle species is investigated. It is found that in addition to the relativistic Buneman instability, which arises from streaming of the volumetrically heated relativistic electrons with the background ions during transparency, ion-ion streaming in the expanding plasma also plays a role in enhancing the final ion energy. Enhancement of proton maximum energies via ion-ion streaming from shock-accelerated aluminium ions is observed in 1D PIC simulations and the energy exchange is demonstrated to be sensitive to the plasma density. Energy transfer between co-directional ion species is also observed in higher dimension 2D simulations. The simulations show that the greatest enhancement in proton energy is due to streaming of electrons in the region of the plasma jet formed in the expanding plasma.

Acknowledgements

The work presented in this thesis is the culmination of three years of research in collaboration with numerous people who all deserve my utmost gratitude. Foremost, I would like to thank my PhD supervisor, Paul McKenna, for his support, encouragement and the opportunities that he has given me throughout the duration of my project to take on greater responsibilities. It is with his patience, understanding and attention to detail that has enabled this thesis to be completed.

The completion of this thesis and the work presented would not have been possible without the support and help of a number of people. I would like to thank David Carroll for his patience, eagerness to share his seemingly endless experience and knowledge and teaching me the ways of experimental laser plasma research. I would also like to thank Martin King for his considerable expertise, and help in performing and interpreting the PIC simulations presented. I would additionally like to thank my friends and colleagues in the group, Ross Gray, David MacLellan, Bruno Gonzalez-Izquierdo, Rachel Dance, Robbie Wilson, Harry Padda, Nick Butler, Remi Capdessus, Dean Rusby and Adam Higginson, who ensured that there was never a dull moment over the last 4 years, be that a late night in the lab, trudging through mountains of data in the office, or in the local watering hole. A special mention must also be made to the other half of the quality polis, Graeme (Toshan) Scott.

Thanks must also be given to the collaborators who have also been involved in this work, Nick Dover, George Hicks and Zulfikar Najmudin at Imperial College London, Satya Kar and Marco Borghesi at Queens University Belfast, Luca Stockhausen and Ricardo Torres at the Centro de Lseres Pulsados(CLPU) and David

Neely at the Central Laser Facility. I would also like to thank the CLF staff and the Vulcan laser team, without whom the experimental campaigns contributing toward the data presented would not have been possible.

Finally, I would like to say a heartfelt thank you to my parents, Marion and Keith, my brothers Shaun and Aaron, and my fiance Teri, for their never ending support and encouragement over the years, and without which I would not be where I am now.

Role of the Author

The author played a leading role in the planning and execution of the experimental campaigns leading to the results presented in this thesis. He was one of the Target Area Operators for the Vulcan experiment in which most of the results were generated, in particular when Dr R. J. Gray and Dr D. A. MacLellan were absent. He was also deputy Target Area Operators on several other related Vulcan ion acceleration experiments. This involved engaging with staff members at the Central Laser Facility in the detailed planning and day-to-day running of the experiment. Key diagnostics in these experiments, including the Thomson parabola ion spectrometers and dosimetry-film stack detectors, were set up by the author. L. C. Stockhausen (CLPU), D. R. Rusby (University of Strathclyde) and B. Gonzalez-Izquierdo (University of Strathclyde) assisted in the shot-to-shot collection of the data. The processing and analysis from the Thomson parabola, RCF stack and laser transmission diagnostic was done by the author, in addition to the development of software for visualisation. He took a lead role in the analysis of data during the experiment, and consequently in leading of the scientific objectives throughout.

The author played a lead role in running and analysing the 1D and some of the 2D EPOCH simulations presented. Other 2D and 3D EPOCH simulations and the analytical modelling of streaming instabilities were performed by Dr M. King (University of Strathclyde). The detailed investigations of the sensitivity of the energy transfer via streaming instabilities to the plasma parameters were conducted by the author. He fully analysed the data presented in this thesis, and contributed to writing of the publications resulting from the work presented.

Publications

Publications resulting from work presented in this thesis

1. **Enhanced laser energy coupling to protons via a self-generated plasma channel in the relativistic-transparency regime**

   H.W Powell, M. King, R. J. Gray, D. A. MacLellan, B. Gonzalez-Izquierdo, L.C. Stockhausen, G. Hicks, N. P. Dover, D. R. Rusby, D. C. Carroll, H. Padda, R. Torres, S. Kar, R. J. Clarke, I. O. Musgrave, Z. Najmudin, M. Borghesi, D. Neely, and P. McKenna (submitted *Phys. Rev. Lett.* 2015)

2. **The role of ion-ion streaming as an energy transfer mechanism in the relativistic transparency regime**

   M. King, H. W. Powell, L. C. Stockhausen, and P. McKenna (in preparation)

Additional publication resulting from PhD project

1. **Tunable mega-ampere electron current propagation in solids by dynamic control of lattice melt**

   D. A. MacLellan, D. C. Carroll, R. Gray, N. Booth, M. Burza, M. P. Desjarlais, F. Du, D. Neely, H. W. Powell, A.P.L. Robinson, G. G Scott, X. H Yuan, C. G. Wahlstrom and P. McKenna, *Phys. Rev. Lett.* **113**, 185001 (2014)

2. **Azimuthal asymmetry in collective electron dynamics in relativistically transparent laser-foil interactions**

R. J. Gray, D. A. MacLellan, B. Gonzalez-Izquierdo, H. W. Powell, D. C. Carroll, C. D. Murphy, L. C. Stockhausen, D. R. Rusby, G. G. Scott, R. Wilson, N. Booth, D. R. Symes, S. J. Hawkes, R. Torres, M. Borghesi, D. Neely, and P. McKenna, *New Journal of Physics* **16**, 093027 (2014)

3. **Effects of target pre-heating and expansion on terahertz radiation production from intense laser-solid interactions**

   X. H. Yuan, Y. Fang, D. C. Carroll, D. A. MacLellan, F. Du, N. Booth, M. Burza, M. Chen, R. J. Gray, Y. F. Jin, Y. Li, Y. Liu, D. Neely, H. W. Powell, G. G. Scott, C. G. Wahlstrom, J. Zhang, P. McKenna and Z. M. Sheng, *High Power Laser Science and Engineering* **2**, e5 (2014)

4. **Fast electron transport patterns in intense laser-irradiated solids diagnosed by modeling measured multi-MeV proton beams**

   D. MacLellan, D. C. Carroll, R. Gray, B. Gonzalez-Izquierdo, H. W. Powell, G. G Scott, D. Neely, and P. McKenna, *Laser and Particle Beams* **31**, 475-480 (2013)

5. **Annular Fast Electron Transport in Silicon Arising from Low-Temperature Resistivity**

   D. A. MacLellan, D. C. Carroll, R. Gray, N. Booth, M. Burza, M. P. Desjarlais, F. Du, B. Gonzalez-Izquierdo, D. Neely, H. W. Powell, A. P. L. Robinson, D. R. Rusby, G. G. Scott, X. H. Yuan, C. G. Wahlstrom, and P. McKenna, *Phys. Rev. Lett.* **111**, 095001 (2013)

6. **Injection and transport properties of fast electrons in ultraintense laser-solid interactions**

   M. Coury, D. C. Carroll, A. P. L. Robinson, X. H. Yuan, C. M. Brenner, M. Burza, R. J. Gray, K. L. Lancaster, Y. T. Li, D. A. MacLellan, H. W. Powell, M. N. Quinn, O. Tresca, C. G. Whalstrom, D. Neely, and P. McKenna, *Physics of Plasmas*, **20**, 043104 (2013)

Contents

List of Figures

Chapter 1

Introduction

1.1 Laser plasma accelerators: a compact fast ion source

The acceleration of charged particles to high energies in electrostatic fields has been explored and applied since the early 20th century. One of the earliest and simplest forms of accelerator is the Van de Graaf generator which simply uses electrostatic potential generated from the build up of charges to create a potential difference between electrodes.

Today, accelerators have come to epitomise the image of 'big science' with the discovery of the Higgs boson at the large hadron collider (LHC) becoming an iconic representation that has captured the imagination of scientists, enthusiasts and the general public, and has garnered attention and publicity from popular TV shows such as The Big Bang Theory.

Modern accelerators use radio-frequency (RF) cavities to accelerate charged particles and typically take two distinct forms. There are linear accelerators in which the particles are accelerated along a linear trajectory with multiple accelerating cavities providing staged acceleration of the particles. From linear accelerators, particles can achieve energies of the order of tens of GeV for electrons, and hundreds of MeV for ions, over an accelerating length of a few kilometres. The limit on the accelerating gradient for an RF accelerator is due to the break down

that can occur within the cavity and is limited to ≈100 MV/m. The maximum energy is determined by the finite length of the acceleration structure.

The second type of accelerator involves cyclical motion, and includes synchrotrons and cyclotrons. In this case the accelerator is a ring and as well as accelerating cavities, large superconducting magnets are used to alter the trajectory of the particle beam such that it follows a circular path. One advantage of this design is that the particle can make multiple trips around the accelerator to achieve the desired energy. One of the drawbacks of this is that, particularly for electrons, the trajectory followed results in a constant change of direction of the particle and consequently acceleration resulting in photon emission known as synchrotron radiation. This emission of radiation limits the energy achievable as the particle energy increase results in increased emission.

The result is that to reach higher energies with future accelerators and the conventional technology, facilities will have to be even larger, bringing with it an even larger price tag. The largest proton accelerator, the LHC, is 27 km circumference. Physics beyond the LHC needs a different approach to acceleration.

By contrast, laser plasma based accelerators have been shown to have accelerating gradients of the order of ≈100 GV/m and acceleration of electrons have demonstrated electron beams of ≈1 GeV over an accelerating length of ≈1 cm from the interaction of an intense laser pulse with under-dense gas targets in the Laser Wake Field Acceleration (LWFA) scheme [4].

The interaction of an intense laser pulse with solid density targets creates a large current of fast electrons that can set up electrostatic ($\sim$ TVm^{-1}) fields, resulting from charge separation, that have been shown to accelerate ions up to energies of tens of MeV. The highest proton energy reported experimentally from picosecond laser pulse drive is $\sim$ 60 MeV [5], though protons energies >100 MeV have been reported in recent experiments from relativistically transparent targets [6].

Laser accelerated ion beams have particularly attractive characteristics with ions able to reach multi-MeV energies over short acceleration lengths of the order of microns, with short acceleration times (of the order of the laser pulse length)

and high beam fluxes. These properties lend themselves as a particularly attractive feature of compact and relatively inexpensive accelerator sources for a wide range of potential applications

1.2 Applications

Fast ions are of particular interest for application due to their unique stopping characteristics in matter. A comparison of the behaviour of energetic electrons, photons and ions is shown in figure 1.1.

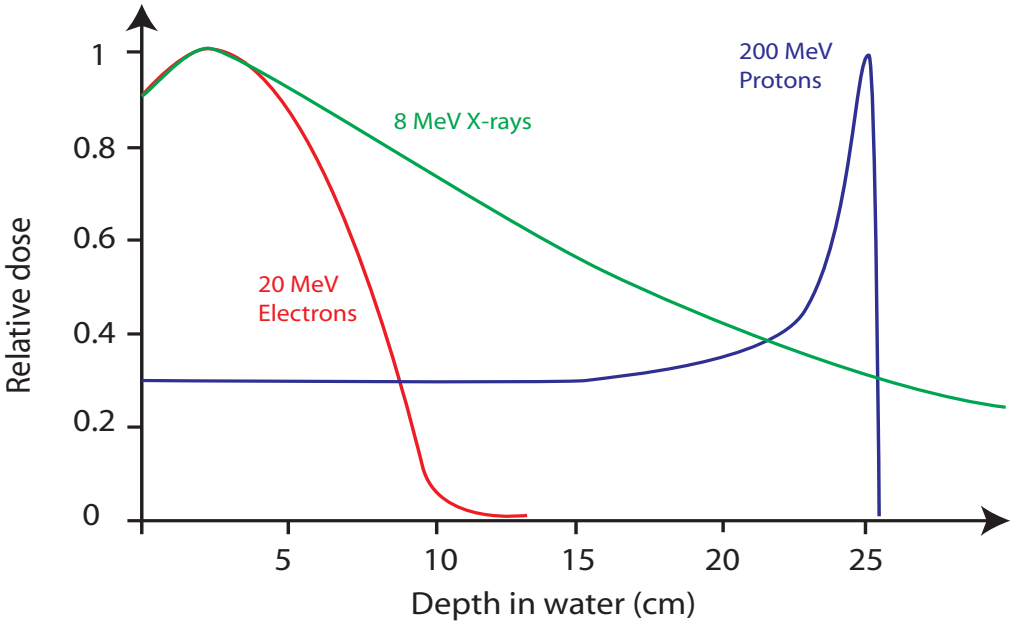

Figure 1.1: Representative stopping behaviour of 20 MeV electrons (blue), 8 MeV x-rays (green) and 200 MeV protons (red) in matter.

Ions propagating in matter will deposit the majority of their energy at a characteristic depth at the end of their range within the target material that is dependent on the material properties and the initial ion energy. The energy deposition with depth into the target is shown schematically in figure 1.1 and it can be seen that most of the energy is deposited toward the end of it's trajectory. This characteristic stopping profile is known as the Bragg peak. This feature of ions makes them particularly interesting for applications.

1.2.1 Hadron therapy

The Bragg peak behaviour of ions in matter, as shown in figure 1.1, make them particularly attractive for treatment of cancerous tumours due to the fact that less dose is deposited in surrounding healthy tissue, compared to the use of X-rays or electrons.

Using ion beams for treatment, a specific initial energy can be selected corresponding to the depth within the body that the tumour resides with minimal damage to healthy tissue surrounding. In particular this treatment could be used for deep tumours that previously would have been untreatable due to their location.

For medical applications such as this, depending on the depth proton energies of up to 250 MeV would be needed as well as a monoenergetic energy distribution [7]. For treatment with heavy ions such as carbon ions ≈400 MeV/u would be needed. Control of the ion beam properties, critically the ion energy, energy spread and flux is also essential. While this is achievable with conventional accelerators, it is less straight forward for current laser-driven ion beams with the present acceleration mechanisms. There are however a number of promising schemes that could fill this criteria and intense international effort has driven the research into alternative laser-ion acceleration schemes promising enhanced efficiency, higher energies and control of the ion beam properties.

There are currently ∼40 hadron therapy facilities worldwide that use conventional accelerators as ion beams sources. Only 0.1% of the patients that could be better treated with ions, compared to x-ray therapy, actually receive this treatment. The size of accelerator and beam steering quadrupole magnets and gantry required to deliver the ion beam from source to patient are prohibitively expensive and therefore treatment is limited. At present there is only one proton therapy centre at Clatterbridge which facilitates treatment of ocular cancers with 50 MeV protons. Two new, higher energy facilities are presently under construction, at Christie Hospital, Manchester and University College London.

Laser plasma ion beam sources would make such facilities much more compact and less expensive in comparison. With such compact sources, the ion acceler-

ation could occur in the patient room, or very close by which minimises bulky beam transport optics [8, 9]. Another proposal is for laser accelerated proton beam injection into a conventional accelerator, reducing the overall size of the accelerator [10].

1.2.2 Proton radiography

The application of proton beams for radiography was first proposed in 1968 [11] using an ion beam from a conventional accelerator to make measurement in density fluctuations. Proton beams have also been successfully used to make temporally and spatially resolved measurements of electric and magnetic fields in the probing of plasmas by proton deflectometry [12–14]. Laser-driven ion beams are favourable for such applications due to the short pulse nature and in this application, a broad energy spectrum also enables time resolved measurement due to the time of flight spreading of ions of differing ion energies. This technique has been used successfully in probing sheath field and expansion from the rear of a solid density target in the TNSA regime by using a second target foil perpendicular to the main target with a second laser pulse inducing TNSA acceleration [15].

The proton beam from the probe foil expands and passes transversely through the region of the main interaction. The presence of strong electric fields from the TNSA acceleration during the main interaction causes deflection of the probing protons, which modifies the spatial intensity profile of the beam. This technique enables the dynamics of both the spatial and temporal evolution of the sheath to be measured. A schematic of a typical set-up is shown in figure 1.2.

This technique has also been employed in measurements of plasma channel formation from relativistically self focussed laser pulses [16], magnetic field generation [17], collisionless shock propagation [18] and can be applied to numerous non-linear processes arising in laser plasmas [7]. Proton probing could also be used in the time-resoled probing of the fields associated with plasma instabilities growths.

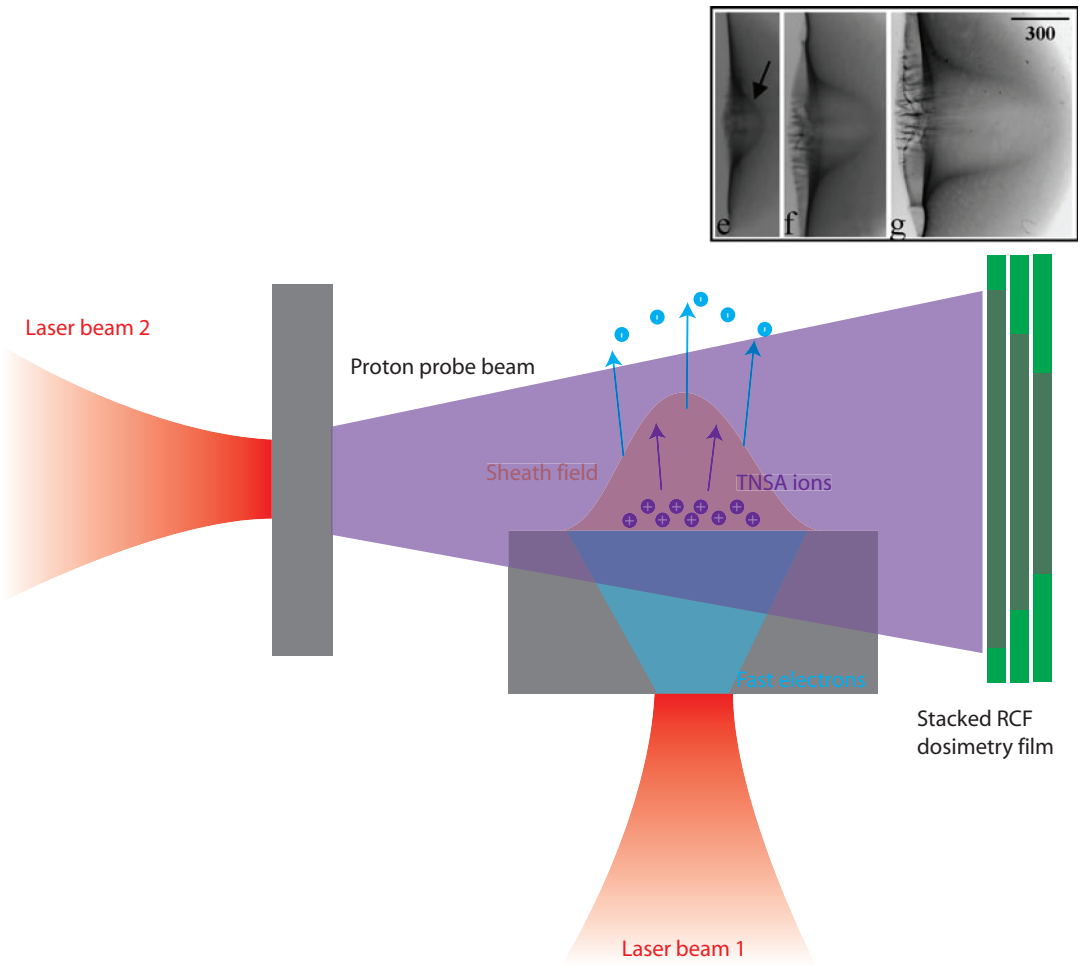

Figure 1.2: Illustration of proton probing of sheath expansion and radiograph from an experiment investigating the temporal evolution of the sheath field. Example results shown in the inset [15]

1.2.3 Fast ignition ICF

The inertial confinement fusion process requires that a capsule filled with a deuterium and tritium (D-T) mixture is imploded and compressed to the necessary densities and temperatures for fusion to take place [19]. The ignition of the fuel occurs within a central hot spot within the compressed fuel and means that the compression must be highly uniform and symmetrical. It has been shown that the fuel compression can be susceptible to hydrodynamic instabilities such as the Rayleigh-Taylor, making these requirements of uniformity and density challenging to achieve and ignition difficult to realise [20, 21].

To relax the requirements stated above and to achieve ignition with a overall

lower laser energy, it was proposed that the compression and ignition are decoupled in what is known as the Fast Ignition (FI) concept. In this scheme the D-T pellet is compressed to a lower density compared to hot-spot ignition and a separate short pulse is used to deliver energetic particles to the compressed fuel and spark ignition.

It was proposed that this could be possible using an intense short pulse to hole bore and form a plasma channel through the coronal plasma [22]. However this would require the critical density surface to be pushed a couple of hundred microns into the dense plasma to reach the optimal region for ignition [21].

Another scheme that was proposed was cone guided FI [23, 24] which enables a region void of plasma to the centre of the implosion shell for the ignition pulse to propagate. In the cone guided scheme, the ignition driver is either from energetic electrons generated from the tip or from TNSA accelerated ions.

In the ion-based FI scheme [21, 25], a thin curved convex foil positioned within the cone acts as the source of the TNSA ions and the curvature of the foil acts to focus the beam to the tip of the cone where the energy is deposited into the fusion fuel to trigger ignition. The Bragg peak ion stopping profile in matter means that the energy can be deposited in a localised spatial region within the fuel and by using protons instead of electrons the complications of electron transport within the dense fuel is reduced.

It has also been proposed to use energetic carbon ions generated in the relativistic transparency regime by the breakout afterburner mechanism as a source for ion FI due to higher conversion efficiency, maximum energy and quasi-monoenergetic energy distribution [26].

1.2.4 Proton heating

A number of experiments have used laser driven ions to heat solid density samples in the investigation of warm dense matter [27, 28], where solid density matter was successfully heated to temperatures of $\sim$15 eV using a TNSA ion beam.

The sample target to be heated is placed within the expanding proton beam of the heating source and with a well characterised spectrum, as well as consid-

eration of the proton time of flight, different temperatures and heating profiles can be achieved within the sample before the main interaction. In this way warm dense matter states can be achieved of interest to electron transport studies. In particular, isochoric heating of solid density targets has been used to investigate resistivity effects on electron transport in solid density targets [29, 30].

In addition, there are numerous other potential applications of laser-accelerated protons and ions including radioisotope production [31–35].

1.3 Thesis Outline

The thesis begins with an introduction to the theoretical principles of laser-matter interactions relevant to work presented, in chapter 2. A more detailed discussion of laser-driven ion acceleration mechanisms, as well as a review of previous work and ongoing research in the field, is presented in chapter 3. This is followed by a discussion of the methods used in experimental laser-plasma physics as well as the numerical tools used to understand the underlying physics of laser-plasma interactions, in chapter A.

Chapter 4 presents experimental work on laser-driven ion acceleration from ultra-thin foils, carried out using the Vulcan petwatt laser system, as well as simulation studies in support of the experimental data. Chapter 5 presents a simulation study of the mechanisms of energy transfer between the laser pulse and the ion population in the relativistic transparency regime. Finally, in chapter 6, the new results are summarised and potential future work is discussed.

Chapter 2

Fundamentals of Laser-Plasma Interactions

This chapter provides a brief overview of the physical principles underlying the interaction of an intense laser pulse with matter. An ultra-intense laser pulse incident onto a solid target rapidly ionises the front surface of the target and the plasma electrons in the intense laser field are accelerated to relativistic velocities, in the electromagnetic field of the laser. The ultimate goal in the context of this work is to maximise the coupling efficiency of laser energy into the accelerated ion population. The mechanisms by which this can be achieved are discussed. Whilst there are many and varied aspects to laser-plasma interactions, only the fundamentals as well as those which are most important in the context and understanding of laser-driven ion acceleration are discussed in this chapter.

2.1 Introduction to plasmas

When a material in either the solid, liquid or gas state is either fully or partially ionised, and there are sufficient free charged particles such that it's dynamics are dominated by electromagnetic forces, it is in the plasma state [36]. This short section will give an introduction to plasmas and the parameters needed to define them, as well as their behaviour and interaction with electromagnetic radiation relevant to high power laser-plasma interactions.

2.1.1 Plasma parameters

There are a number of key parameters used to describe a plasma, characterised by their temperature and density. The first concerns the electrostatic nature of the plasma and it's charge neutrality. The Debye shielding distance of a plasma is defined as the distance over which a point charge in a plasma can influence and outside of which charges are shielded from it's influence. The Debye length is defined as:

$$\lambda_D = \sqrt{\frac{\epsilon_0 k_B T_e}{n_e e^2}} \tag{2.1}$$

where k_B is Boltzmann constant, T_e is the electron temperature, n_e the electron density, e the electron charge and ϵ_0 is the permittivity of free space for vacuum. From the centre of the point charge, outside a volume of radius equal to the Debye length, the charge will remain neutral and shielded from electric fields in the plasma. One of the key criteria used to define a plasma is that the Debye length must be much smaller than the size of the system [36, 37].

The plasma parameter, g, is a measure of the number of electrons present within a Debye sphere and provides a measure of the collective nature of the plasma. The greater the number of particles within the Debye sphere, the less probable collisional effects will be. The condition to be satisfied for this to be the case is:

$$g = \frac{1}{n_e \lambda_D^3} \ll 1 \tag{2.2}$$

This is second criteria used in the definition of a plasma, that a large number of particles is within a Debye sphere [36, 37].

Imbalances in the charge neutrality of the plasma cause oscillation of the mobile charge carriers, typically electrons, within the Debye sphere. The natural frequency at which the electrons oscillate is known as the plasma frequency and is expressed as:

$$\omega_{pe} = \frac{(k_B T_e / m_e)^{\frac{1}{2}}}{\lambda_D} = \Big(\frac{n_e e^2}{m_e \epsilon_0}\Big)^{\frac{1}{2}} \tag{2.3}$$

The ions in the plasma also have a characteristic oscillation period. However due to the increased mass the ion response period is much longer and is given by:

$$\omega_{pi} = \left(\frac{n_i(Ze)^2}{m_i\epsilon_0}\right)^{\frac{1}{2}} \tag{2.4}$$

where n_i is the ion density, m_i the ion mass and Z the charge state.

The rate of collisions within the system must be small compared to the natural frequency of oscillation of the plasma, as given in equation 2.3, and this is the third criteria used in the description of a plasma, signifying a regime where electromagnetic forces dominate within a system [36, 37].

For electromagnetic radiation with a frequency less than that of the electron plasma frequency it can seen that the influence of the external field will be shielded by the electron plasma oscillation. The plasma will be opaque to radiation of frequencies less than the plasma frequency and the fields will not be able to propagate into the plasma. The importance of this effect will be described in more detail later in section 2.2.

2.2 Laser produced plasmas

An intense laser pulse with a peak intensity of $I_0 = 1 \times 10^{20}$ Wcm^{-2}, will have a peak electric field strength of the order of ~ 27 TVm^{-1}. Fields of this strength will very easily strip atoms of their constituent electrons and form a plasma. The electrons, now free of the ion, will feel the influence of the oscillating field of the laser pulse. In such intense fields, electrons quickly gain energy greater than the electron rest mass energy and become relativistic in their motion.

2.2.1 Laser induced ionisation

There are a number of distinct regimes by which ionisation of matter in the presence of an intense laser pulse can occur and these will be considered in the following subsection.

If we first consider the simplest case of the ionisation of a hydrogen atom

whereby a single electron is liberated. To calculate the threshold intensity for single photon ionisation of a hydrogen atom, first the Bohr radius must be considered such that the binding energy of the atom can be found. The Bohr radius is given as:

$$a_B = \frac{4\pi\epsilon_0\hbar^2}{m_e e^2} \tag{2.5}$$

where $\hbar$ is the reduced Planck constant and m_e is the electron mass. From the Bohr radius, the binding strength of the electron to the atom can be found as in equation 2.5 and this value is used to calculate the equivalent intensity needed to overcome the binding energy and release the electron with a single photon. The electric field strength at a distance equivalent to th Bohr radius due is given as:

$$E_a = \frac{e}{4\pi\epsilon_0 a_B^2} \tag{2.6}$$

Substituting for a_B gives an approximate value of 5.1×10^9 Vm^{-1}, which is much lower than that of the electric field of the laser pulse, which is of the order 10^{12} Vm^{-1}. This corresponds to a incident threshold peak laser intensity given by:

$$I_a = \frac{c\epsilon_0}{2} E^2 \tag{2.7}$$

where E_A is the electric field strength at the Bohr radius. From this expression, an intensity of $I_a \approx 3.5 \times 10^{16}$ Wcm^{-2}, is required to ionise hydrogen. An intensity of I_L greater than this value will ensure ionisation by a single photon process [38]. A much lower threshold intensity can be achieved however due to ionisation by absorption of multiple photons, in a process known as multi-photon ionisation (MPI). The absorption of multiple photons simultaneously acts to liberate an electron into a free state by satisfying the condition:

$$E_{ion} = n\hbar\omega_L \tag{2.8}$$

where $\hbar\omega_L$ is the single photon energy, E_{ion} is the electron binding energy and

n the number of photons absorbed. Under these conditions, ionisation can occur at much lower intensities, of the order of $\approx 10^{13}$ Wcm^{-2} for ionisation of hydrogen [39, 40]. This is the minimum photon number required for the electron to gain sufficient energy to escape the potential of the atom. However, absorption of a number of photons greater than this threshold will result in the electron gaining net energy and is known as above-threshold ionisation and the electron will leave with energy equal to $n\hbar\omega_L - E_{ion}$ where n is the number of photons absorbed and E_{ion} is the electron binding energy of the given state.

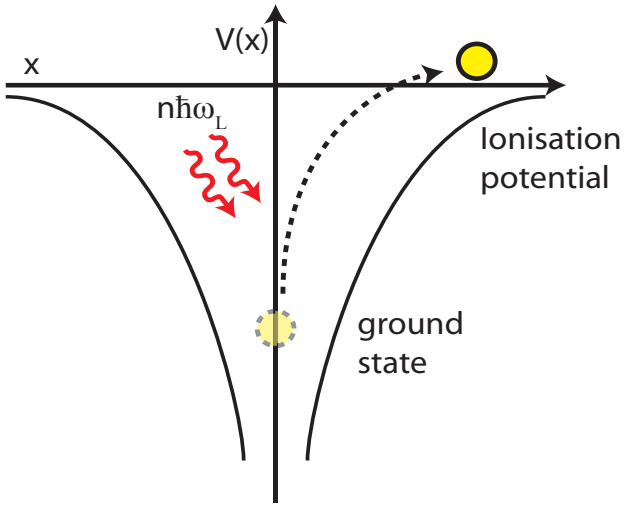

Figure 2.1: Schematic representation of multi-photon ionisation. The electron absorbs a discreet number of photons of frequency ω_L, gaining energy above the ionisation potential enabling it to escape.

The electron having gained energy greater than that required to escape the potential of the binding nucleus can subsequently induce further ionisation via collisions.

As has been discussed previously, the electric field amplitudes achieved at the focus of an intense pulse are of the order of, or greater than, the atomic Coulomb potential. The external field applied to the atom due to the laser can act to modify the potential barrier of the atom, suppressing it as illustrated in figure 2.2.

When the Coulomb potential barrier is deformed in the presence of the external laser field, electrons can escape by either tunnelling through the lowered

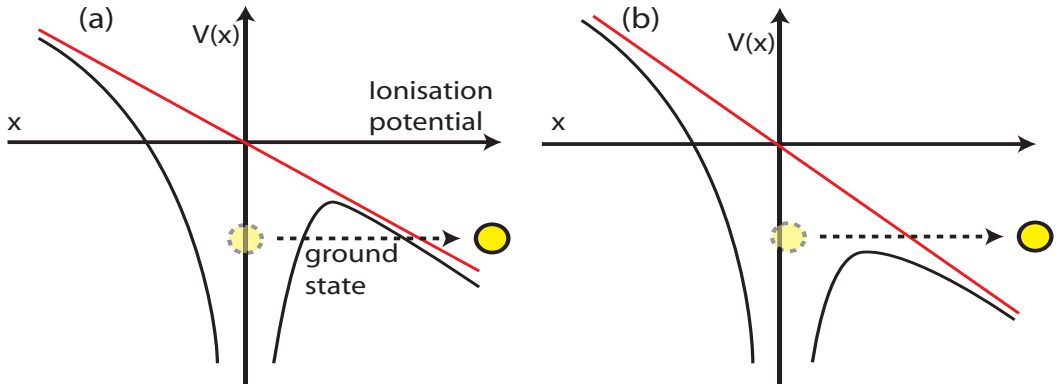

Figure 2.2: Schematic representation of barrier suppression. The electron escapes the potential well of the atom by either (a) tunnelling through the suppressed potential barrier or, (b) over the barrier ionisation if the barrier is suppressed sufficiently and below the ground state electron energy.

barrier or if it is sufficiently suppressed, escape over it. Both processes are shown in figure 2.2. Tunnelling ionisation arises from distortion of the potential barrier and the quantum probability of the electron being able to tunnel through the reduced barrier.

The rate of ionisation by barrier suppression, including both tunnelling and over the barrier ionisation, is summarised by the ADK model [41] given by:

$$w_{ADK} = \sqrt{\frac{3n^{*3}E}{\pi Z^3}}\frac{ED^2}{8\pi Z}exp\left(\frac{2Z^3}{3n^{*3}E}\right) \tag{2.9}$$

where $n^* = \dfrac{Z}{\sqrt{2E_a}}$ is the effective principle quantum number, Z is the ionic charge, E is the amplitude of the external laser field strength, and $D \equiv \left(\dfrac{4eZ^3}{En^{*4}}\right)^{n^*}$.

Differentiation between regimes where multi-photon and barrier suppression ionisation processes are dominant can be determined from work by Keldysh *et al* [42], known as the adiabaticity parameter, γ_k, and is defined as:

$$\gamma_K = \frac{\omega\sqrt{2E_a}}{E} \tag{2.10}$$

For values of $\gamma_K > 1$, the multi-photon ionisation process will dominate, and for $\gamma_K < 1$ the barrier suppression regime will contribute the greatest.

The EPOCH PIC code, used in chapter 5, includes a field ionisation package

which can also be implemented. The code's ionisation model consists of three regimes, multiphoton, tunneling and barrier suppression ionisation. The processes described above are what are known as collisionless ionisation processes, where the fields associated with the interaction are considered only. The intensity of the incident laser pulse results in significant electron energies resulting in a large corresponding mean free path. However for electrons at relatively low kinetic energies, the collisional frequency, $\upsilon_{ei} \propto k_B T_e^{\frac{-3}{2}}$, is much larger and collisions with other atoms in the target are more likely.

2.2.2 Relativistic electron motion in a laser field

In this section, the motion of an electron in a plane electromagnetic wave is considered.

The laser is considered to be relativistically intense when the energy of the electron oscillating in the laser field is equal to or greater than the rest mass energy. To quantify this value in terms of intensity the dimensionless laser amplitude, a_0 is introduced as:

$$a_0 = \frac{eE_L}{m_e c \omega_L} = \sqrt{\frac{I\lambda^2}{1.37 \times 10^{18} W cm^{-2}}} \tag{2.11}$$

where E_L is the peak electric field and ω_L is the frequency of the laser. The value of a_0 can be related to the electron Lorentz factor γ_L for the case of linear polarisation:

$$\gamma = 1 + \frac{a_0^2}{2} \tag{2.12}$$

The motion of the electron in the presence of an EM wave is described using the Lorentz equation:

$$\frac{d\mathbf{p}}{dt} = -e(\mathbf{E} + \mathbf{v} \times \mathbf{B}) \tag{2.13}$$

where $\mathbf{p} = \gamma m_e \mathbf{v}$ is the relativistically corrected electron momentum, $\mathbf{E}$ and $\mathbf{B}$ are the electric and magnetic field amplitudes, respectively, and γ is the rel-

ativistic Lorentz factor and $\gamma = \sqrt{1 + (\frac{p^2}{m_e^2 c})^2}$. Due to the much larger mass of the plasma ions, at laser intensities considered herein their response to the laser fields is negligible compared to that of the electrons, and so they are treated as stationary and only the electron dynamics considered. From equation 2.13, as the electron velocity **v** becomes comparable to **c** the influence of the magnetic field on the electron motion becomes increasingly important.

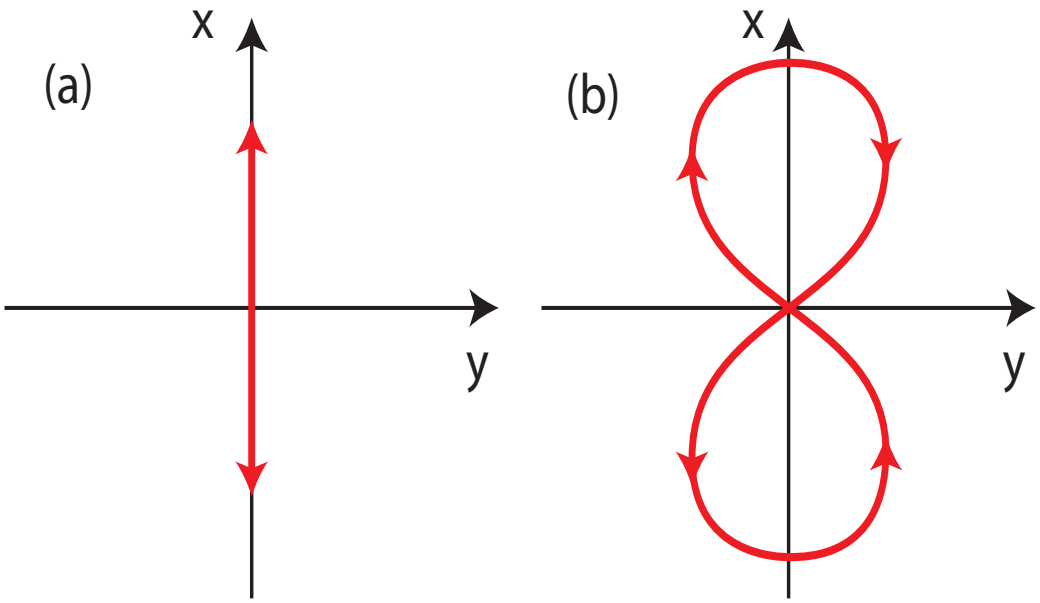

Figure 2.3: Motion of an electron oscillating in a electromagnetic field in the rest frame for (a) non relativistic intensities where $a_0 \ll 1$ and (b) for intensities where the quiver velocity is relativistic and $a_0 \geq 1$.

In the non-relativistic limit, the electron oscillates primarily due to the electric field and will have a oscillation frequency equal to that of the laser frequency in the polarisation direction of the laser. In the case where the electron velocity is below the relativistic limit, $v \ll c$, the force experienced by the electrons in the oscillating electric field is perpendicular to the poynting vector of the laser and is described as:

$$F_\perp = e\mathbf{E}cos(\omega_L t) \tag{2.14}$$

However, as $\gamma \geq 1$ and $v \sim c$, the $q\mathbf{v} \times \mathbf{B}$ component of the Lorentz force equation is no longer negligible and must be taken into consideration. The force

due to the magnetic field component is by:

$$F_{\parallel} = ev_{\perp}\mathbf{B} = e\frac{v_{\perp}}{c}\frac{\mathbf{E}}{2}sin(\omega_L t) \tag{2.15}$$

where the transverse velocity is given by:

$$v_{\perp} = \frac{eE_0}{m_e\omega_L} \tag{2.16}$$

The magnetic field will result in a force on the electron that is along the laser propagation direction. The motion incurred due to the $v \times B$ component will cause the electron to follow a 'figure-8' trajectory in the rest frame as the longitudinal component of the momentum becomes comparable with the transverse motion.

The case considered above is for that of a plane wave, and under these conditions the electron gains no net energy from the passage of the EM field and once it has left the electron will return to it's rest position.

2.2.3 Pondermotive force

In the previous section we considered the motion of an electron in a plane wave. In reality however, realistic laser pulses have both a finite spatial and temporal extent. Intense short pulse lasers are focussed down to a Gaussian spot of the order of a few microns diameter, close to the diffraction limit. With a pulse focussed to such a spot, the spatial-intensity gradient is substantial.

In a finite spatial intensity distribution, the electrons centred on the laser axis and under the influence of the Lorentz force will experience a transverse oscillation over one half of the electric field cycle as well as a forward drift due to the $v \times B$ component. In a plane wave with no spatial profile the electron would return to its initial state after the second half of the laser cycle.

The finite spatial profile of the laser though means that after the first half cycle of the field, the electron having been pulled from the laser axis will now be in a region of lower intensity and therefore the restoring force pulling the electron back toward the laser axis will be lower, resulting in a net gain of electron energy. Averaged over time this will result in a drift of the electron from the laser axis to

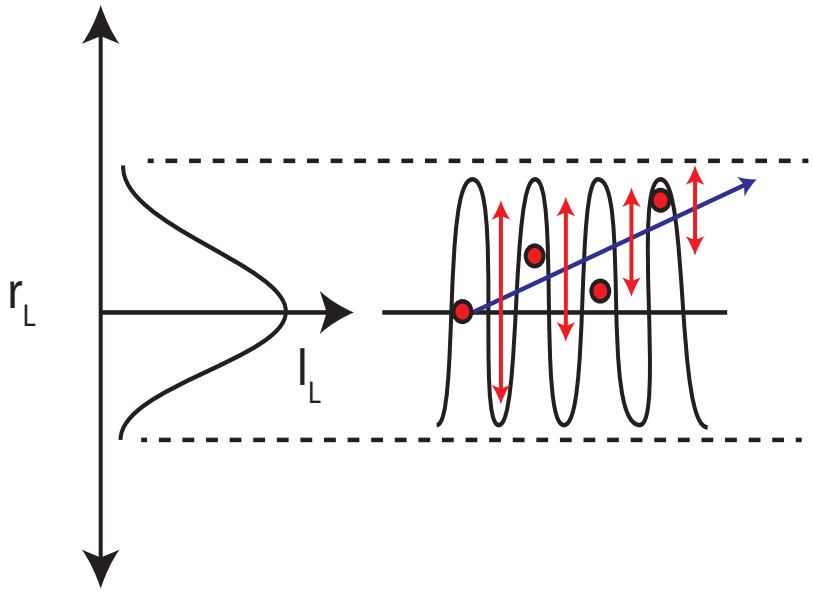

Figure 2.4: Radial intensity profile of the laser pulse and electron drift experienced due to the resulting pondermotive force.

regions of lower intensity in the laser propagation direction and is known as the pondermotive force.

In the non relativistic limit, the pondermotive force is given the equation 2.17, where only the transverse oscillation of the electrons due to the electric field is considered.

$$F_{pond} = -\frac{e^2}{4m_e\omega_L^2}\nabla\mathbf{E} \tag{2.17}$$

As the transverse velocity approaches c, with increasing laser intensity, not only the spatial intensity distribution effect, as discussed above, but the relativistic motion in the laser field will contribute.

The time averaged pondermotive force in this relativistic regime is given by equation 2.18 and the derivation of which can be found in [38, 43].

$$F_{pond} = -mc^2\nabla\sqrt{1+\frac{a_0^2}{2}} \tag{2.18}$$

There are a number of interesting effects that arise in the relativistic regime and due to the pondermotive potential of the laser therein. These include: (1)

plasma channel formation due to pondermotive expulsion of electrons centred on the laser axis [44]; (2) hole boring of the critical density layer due to the radiation pressure exerted from the laser pulse by the $j \times B$ [45] and (3) steepening of the density profile as a result [46].

These effects will be discussed in further detail in later sections as well as the role they play in the context of laser driven ion acceleration.

2.3 Laser interaction with matter

In the interaction of an intense laser pulse with a solid density target, the target is rapidly ionised by the strong electric field of the focussed pulse as discussed in section 2.2.1. This results in a hot dense plasma that begins to expand into the vacuum. The subsequent electron dynamics are governed by the Lorentz force.

As the laser pulse propagates through the expanding plasma, it's path is governed by the refractive index dependence on the electron density along the density gradient of the expansion. The propagation of an intense laser pulse into an expanding plasma can result in relativistic self-focussing and channel formation leading to increased absorption of the laser pulse [47]. There is a well defined point however when the plasma becomes opaque to the propagating laser pulse and it can no longer propagate. This corresponds to a density known as the critical density and is given by:

$$n_c = \frac{\epsilon_0 m_e \omega_L^2}{e^2} \tag{2.19}$$

This corresponds to the density at which the plasma frequency is equal to the laser frequency. As discussed in section 2.1.1, due to the Debye screening effect, electromagnetic fields with frequency less than the characteristic plasma frequency will be screened out due to the dominance of the natural oscillation of the plasma electrons over the Debye sphere.

For the case $\omega_{pe} > \omega_L$, the solutions to the plasma dispersion relation 2.20, for the wave vector of the propagating laser pulse, k, tend to zero. At the point

of $\omega_L = \omega_{pe}$, $k = 0$, and the pulse is reflected from the critical surface.

$$\omega_L^2 = \omega_{pe}^2 + k^2 c^2 \tag{2.20}$$

This is the defining parameter between under-dense and over-dense interaction regimes, though relativistic effects make this distinction less clear cut and will be discussed in more detail in section 2.3.5.

Beyond the critical surface where plasma density is greater than the critical density, and the plasma frequency is greater than laser frequency, the k vector solution is complex and represents an evanescent decay of the laser field.

The range beyond the critical density for which the electric field of the laser decreases exponentially is known as the collisionless skin depth and is given by:

$$l_s = \frac{c}{\omega_{pe}} \tag{2.21}$$

2.3.1 Plasma expansion

Under realistic laser pulse conditions achievable experimentally, the main interaction pulse which has a duration of between 30 fs and 1 ps will also have an intensity pedestal that can precede it by a duration of nanoseconds. This 'Amplified Spontaneous Emission (ASE)' is inherent in the process of generating and amplification of the laser pulse in the laser chain and is discussed in more depth in chapter A.

Without the use of pulse cleaning techniques such as plasma mirrors, the intensity of the ASE can be a factor of $10^{-6} - 10^{-8}$ of that of the main pulse, which for a main pulse of peak intensity of the order 10^{20} Wcm^{-2} is still well above the ionisation threshold.

This ASE pedestal begins to ablate the target front surface, causing a coronal plasma blow-off and target pre-expansion. The presence of this low density expanding plasma means that the laser pulse must propagate through this before reaching the critical surface and that the interaction will no longer be with a sharp solid-vacuum density boundary.

For this reason it is important to reduce the level of ASE and pre-pulses prior to the main pulse below the threshold for ionisation. The technique by which these conditions may be met are discussed in further detail in chapter A and the sensitivity to, and consequences of, significant target pre-expansion are discussed in chapter 4.

The target pre-expansion and the corresponding density gradient can be characterised by a parameter known as the density scale length [48], L_{ne} which is approximately as:

$$L_{ne} \simeq C_s \tau_L \tag{2.22}$$

where τ_L is the laser pulse duration, $C_s = \sqrt{\frac{k_B(ZT_e + T_i)}{m_i}}$ is the ion sound speed, Z is the ionisation state, m_i the ion mass, k_B Boltzmann constant and, T_e and T_i the electron and ion temperatures respectively.

The density profile of the plasma expanding in the x direction will usually have an exponential form such as:

$$n_e(x) = n_0 e^{\frac{-x}{L_{ne}}} \tag{2.23}$$

where n_0 is the electron density of the initially unperturbed solid target and $n_e(x)$ is the spatially varying electron density along the longitudinal axis (x) normal to the target surface.

The presence of a pre-plasma impacts on the dynamics of the interaction of the main laser pulse and the absorption mechanisms as well as the propagation through the underdense plasma region. Characterisation of the pulse conditions is significance in the understanding of the absorption physics as the role and dominance of mechanisms of coupling of laser energy into the plasma strongly depend on the scale length at the front surface.

Previous experimental and theoretical work, [47, 49, 50], have investigated the effect of plasma scale length on the absorption of an intense pulse by using a separate nanosecond laser pulse to vary the pre-plasma expansion before the arrival of the main short pulse. The propagation of the short pulse through a

sufficiently long the under-dense plasma is susceptible to effects such as relativistic self focussing [38], channelling [51] and filamentation instabilities [52, 53].

2.3.2 Relativistic self-focussing

In reality, an intense laser pulse is focussed onto the target by a parabolic or spherical mirror. At focus, the spot has a Gaussian or $Sech^2$ spatial intensity distribution. At relativistic intensities, as discussed above, the quiver velocity of the electrons in the oscillating electric field of the laser pulse tends to the speed of light, and relativistic effects must be considered.

For gamma values greater than 1, effects such as the relativistic increase in the mass of the electrons must be taken into consideration.

The natural oscillation frequency of the plasma electrons, as discussed in section 2.1.1, scales with the electron density as well as the inverse of electron mass. An increase in the mass of the plasma electrons will result in a decrease of the electron plasma frequency.

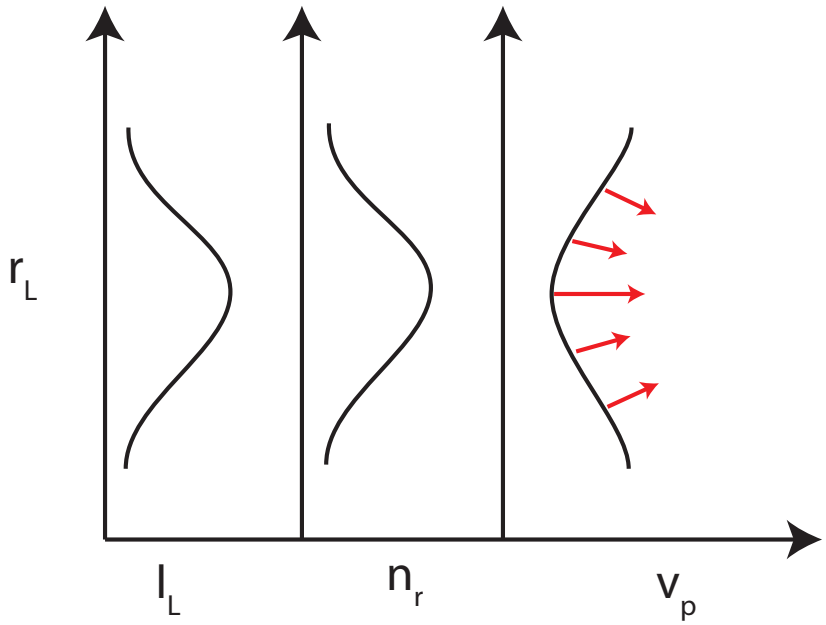

Figure 2.5: Schematic showing the radial intensity distribution, plasma refractive index and phase velocity profiles

The refractive index of the plasma is given below in equation 2.24 and is dependent on the plasma frequency. As has been discussed previously in section

2.2, the laser can only propagate in a plasma up until the point where the density is such that the plasma frequency is equal to the laser frequency (the critical density). The refractive index of a plasma is thus always less than 1 for the condition where a laser pulse can propagate in the plasma.

$$n_r = \sqrt{1 - \left(\frac{\omega_p^2}{\gamma\omega_L^2}\right)} = \sqrt{1 - \left(\frac{n_e}{\gamma n_{crit}}\right)} \tag{2.24}$$

where ω_p is the plasma frequency, ω_L is the laser frequency and γ is the electron Lorentz (gamma) factor.

With increasing electron gamma factor, the plasma frequency is reduced, resulting in an increase in the refractive index of the plasma. The laser pulse, focussed onto the target typically has a 2D Gaussian intensity profile. Since the electron Lorentz factor is intensity dependent, this will correspond to a 2D refractive index profile across the laser pulse profile. The phase velocity of the pulse in the plasma is given by:

$$v_p = \frac{\omega}{k} \tag{2.25}$$

where k is the wave vector. The radial relativistic mass increase due to the 2D pulse intensity profile results in a lower phase velocity on axis creating a curvature of the phase front and focussing of the pulse as shown schematically in figure 2.5. The pondermotive expulsion radially of the electrons also results in a radial density gradient, with a higher electron density in the low intensity spatial region. Due to the radial variation in refractive index the phase velocity of the laser pulse will also have a radial profile, with the phase front velocity slower on axis. This is illustrated in figure 2.5 which shows a representation of the 2D intensity profile and corresponding behaviour of the refractive index and phase front velocity.

The curvature in the phase front will act to bend the light rays resulting in a focussing effect on the beam profile. The laser pulse will relativistically self focus when the total power, in gigawatts, exceeds a critical value [38, 44], given

in equation 2.26.

$$P_{crit} \simeq 17(\frac{\omega}{\omega_{pe}})^2 GW \tag{2.26}$$

At this critical power, the self focussing of the laser is balanced by the diffraction of the beam and this is the threshold for relativistic self-focussing.

The competition between the diffraction of the beam and the self focussing means that the angle of self-focussing must be greater than that of the diffraction divergence angle, and is satisfied for equation 2.26. In this regime, the laser pulse is optically guided through the under-dense plasma.

2.3.3 Hole-boring

As has been discussed in the previous section, for intensities in which the electron motion is relativistic, the pondermotive force acts to drive electrons in the laser propagation direction due to the $v \times B$ component of the Lorentz force. When the laser is sufficiently intense, the pressure exerted on the critical surface by the laser can be high enough that it is possible to overcome the thermal pressure of the electrons [54]. The pressure exerted by the laser is given by:

$$P_L = (1 + R)\frac{I_L}{c} \tag{2.27}$$

where R is the reflectivity from the front surface and I_L is the intensity of the incident pulse.

The pressure imbalance results in a hole being bored into the plasma by the laser, pushing the surface forward most where the intensity is highest, at the centre of the focal spot.

This results in a dense electron population being driven into the target with a constant velocity for a constant intensity laser driver, forming an electrostatic shock. The charge separation field resulting from the depletion of electrons from the hole accelerates the ions from the region forward. Ions that are ahead of the shock front will be reflected due to the electrostatic shock to twice the shock velocity [38]. The consequences of this for ion acceleration will be considered in

more detail in the next chapter.

The velocity of the hole boring front driven by the laser radiation pressure can be estimated by considering the balance between the ion pressure and the radiation pressure in the laboratory frame [38], and is given by:

$$v_{HB} = \sqrt{(1+R)\frac{I_L}{m_i n_i c}} \tag{2.28}$$

where n_i is the ion number density and m_i the ion mass.

Experimentally, the velocity of the hole boring front can be determined by the measured spectrum of the back-reflected light. As the hole boring front is being driven forward, the spectrum of the reflected light will be frequency shifted toward the red end of the spectrum. The hole boring velocity can therefore be determined by the Doppler red-shift from the Doppler formula:

$$\omega_r = \omega_L \frac{1-\beta}{1+\beta} \tag{2.29}$$

where $\beta = v_{HB}/c$ is the hole boring velocity of the critical surface. Consequently, a blue shift observed in the back reflected spectra indicates expansion as opposed to recession of the critical surface and highlights the importance of measuring experimentally the reflected portion of the laser pulse as a diagnostic of plasma dynamics.

2.3.4 Relativistic channelling

The radial pondermotive force, as discussed previously, acts to expel electrons from regions of high intensity and the relativistic electron velocity causes a mass increase locally decreasing the refractive index on axis and ultimately resulting in self focussing of the beam.

Sustained propagation of the pulse into the plasma results in the formation of a plasma channel where electrons on axis are expelled radially outwards leaving a reduced density within.

For underdense plasms, $n_e \ll n_{crit}$, and laser pulse powers greater than the critical power given in equation 2.26, the pondermotive force is sufficiently large

that pondermotive force expels all electrons from the regions of highest laser intensity on-axis. This results in a channel free of electrons along the central axis of the propagating pulse and enables the laser to be guided within the channel.

In plasmas of higher density, that are closer to the critical density $n_e \sim n_{crit}$, a laser pulse undergoing relativistic self-focussing is susceptible to transverse instabilities resulting in beam filamentation, which effectively competes with channel formation [55]. In near critical density plasma not all electrons are expelled from the central region of the channel and a current of electrons within the channel acts to magnetise the surrounding plasma. The quasi-static self generated magnetic fields can reach strength close to that of the laser itself [56]. If the magnetic field is sufficiently strong, pinching of electron filaments, that follow the filamented laser profile, can result in collapse into a single channel that contains a large fraction of the laser energy [56].

2.3.5 Relativistic induced transparency

Other interesting effects occur due to the relativistic motion of electrons in an intense laser field, one such phenomenon is relativistic induced transparency.

As discussed previously, the laser can only propagate in the plasma until a characteristic density known as the critical density. The pulse is then either absorbed (processes of which will be discussed in further detail later), or reflected. However it has also been shown that the electron motion in a sufficiently intense laser field can reach relativistic velocities.

The laser pulse is incident on an ultra-thin foil of tens of nanometers in thickness, where the electrons density is initially at solid density. As the pulse accelerates the electrons at the critical surface, they reach relativistic velocities and experience an increase in mass by a factor of γ. As the laser pulse witnesses the critical surface, the electron density has been reduced by a factor of γ and hence the critical density is increased by the same factor [57]. As the plasma refractive index corrected for relativistic effects depends on the ratio $n_e/\gamma n_{crit}$ as shown previously in equation 2.24, the effective refractive index is reduced, enabling the laser to propagate further into the target.

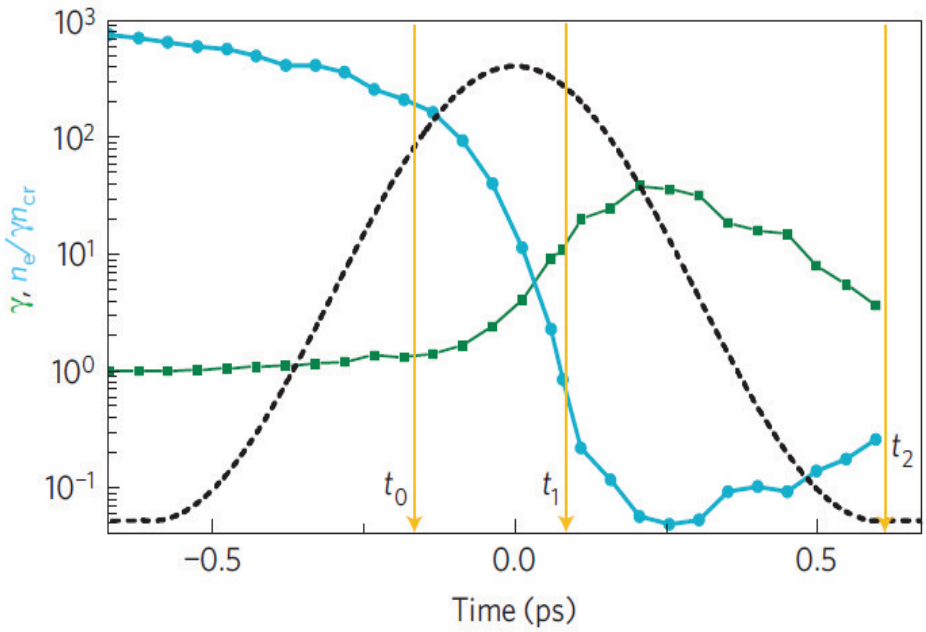

Figure 2.6: Temporal evolution of the electron density normalised to the relativistically corrected critical density (blue), electron lorentz gamma factor (green) and the temporal profile of the laser (black), from a 2D PIC simulation. Adapted from [58]

In this way, the plasma frequency is reduced by a factor of γ such that the effective frequency is $\omega_{pe}^{'} = \omega_{pe}/\gamma$. This reduction means that the skin depth, $l_s = c/\omega_{pe}^{'}$, by which the laser field beyond the critical surface decays evanescently, is increased. Once this reaches a value comparable with or greater than the target thickness transmission of the laser field occurs.

To achieve pure relativistic induced transparency however, much higher laser intensities than currently available from state of the art laser technology would be required. For solid density, fully ionised aluminium, a Lorentz factor of $\gamma = 780$ would be required, such that the critical density would be equal to solid, meaning an $a_0 \sim 1100$ or $I_L \simeq 10^{24}$ Wcm^{-2}.

At peak laser intensities achievable at present, some degree of target expansion is required, together with the relativistic increase in the critical density such that the criterion ($\frac{n_e}{\gamma n_{crit}} < 1$) for relativistic transparency is met.

This is represented in figure 2.6 which depicts results from 2D PIC simulations by Palaniyappan *et al* [58], where the blue line represents $n_e/\gamma n_{crit}$, the green line the electron gamma factor, and black the super-imposed temporal envelope of the laser pulse. The times marked t_0, t_1, t_2 correspond to the times when, (1) the

target is overdense, (2) relativistically underdense transmission of the laser pulse can occur and (3) the target is classically underdense.

2.4 Absorption

The previous sections have discussed the collective electron dynamics in an intense laser field. This section is concerned with interaction of an intense pulse with a plasma and the mechanisms by which energy is exchanged between the incident laser pulse and the plasma. The incident laser light cannot propagate beyond the critical density surface. In the region of n_{crit} significant coupling of energy between the laser into the target occurs. The energy is coupled either by collisional or collisionless absorption processes. In the case of intensities where the electron motion is in the relativistic regime and the mean free path λ_e of the electrons is large, collisionless absorption, i.e. field-driven absorption processes, tend to dominate.

2.4.1 Resonance absorption

Resonance absorption is prevalent when the front surface of the target has a significant density gradient, $L > \lambda_L$, an oblique laser incidence angle and linear polarisation with the plane of polarisation normal to the target surface (p-polarised). The case of a sharp density interface will be discussed in further detail in the next section. The laser pulse propagates through the expanding plasma, being constantly refracted by the increasing electron density.

At this point, due to refraction and then reflection at $n_{crit}\cos^2(\theta)$, the laser electric field oscillates normal to the critical surface. This condition results from the oblique incidence with consideration to the dispersion relation and the laser k-vector to include the incidence angle. The k-vector perpendicular to the density gradient is then expressed as $k_y = (\omega_L/c)\sin^2(\theta)$. Consequently the plasma dispersion relation becomes:

$$\omega_L^2 = \omega_{pe}^2 + k_x^2 c^2 + \omega_L^2 \sin^2(\theta) \tag{2.30}$$

For the condition where the pulse is reflected this corresponds to a density $n_{crit}\cos^2(\theta)$. The electric field component normal to the target surface can tunnel through to resonantly drive a plasma wave at the laser frequency at the critical density surface. Beyond $n_{crit}\cos^2(\theta)$ the laser electric field decays evanescently and the restoring force on the electrons is weaker.

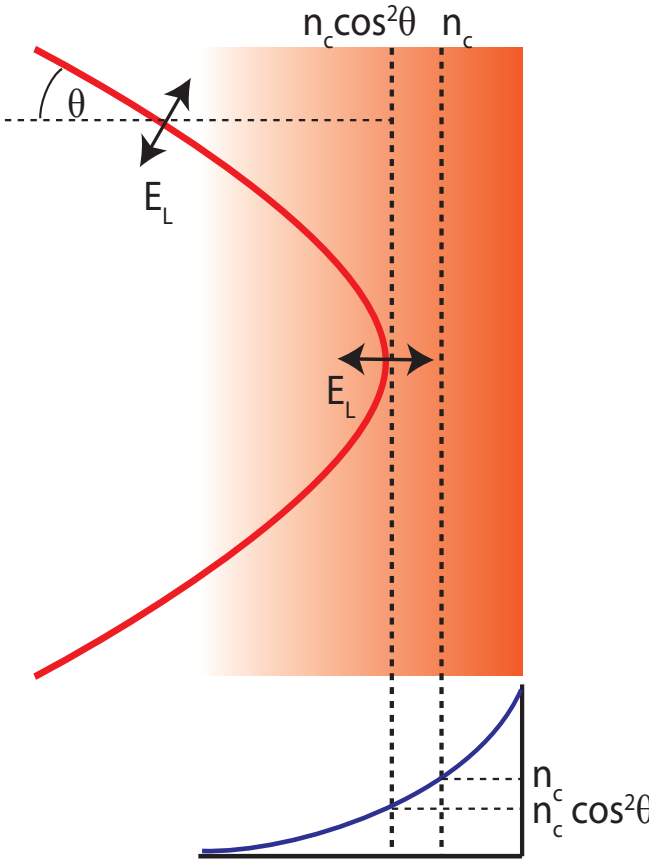

Figure 2.7: Schematic showing laser propagation through a density gradient and the corresponding electric field direction with respect to the target surface

The resonantly driven plasma wave can transfer energy into the plasma by damping of the wave or wave breaking [59]. This results in a population of fast electrons that are injected into the target at the laser frequency.

2.4.2 Vacuum (Brunel) heating

Consider the same conditions as described above, i.e. an obliquely incident linearly polarised pulse, but this time incident on a sharp density gradient. In this scenario, the electrons oscillate in the E-field of the laser as before but plasma

waves cannot be excited due to the sharp vacuum-plasma boundary. The electrons are instead stripped from the plasma, out into the vacuum in one half cycle of the laser field. Upon the E-field direction change, they are then driven back into the target beyond the vacuum-plasma interface.

Once re-injected into the target they extend beyond the critical surface. Since the target is over-dense, the laser electric field is only able to penetrate to approximately a skin depth beyond the critical density layer. The restoring force of the laser on the electrons at this point is weaker resulting in a net gain of energy by the electrons, creating a population of fast electrons that are injected into the target and travel through it. Vacuum heating dominates in the case when the amplitude of the electron oscillation is greater than the density scale length.

2.4.3 Pondermotive (j × B) heating

The $j \times B$ mechanism is similar to the Brunel heating scheme, in that electrons are accelerated by the laser fields in the presence of a sharp density gradient most effectively by this mechanism. At relativistic intensities, the electrons are accelerated to velocities close to c and the $v \times B$ term of the Lorentz force equation becomes comparable with that of the electric field term.

As discussed previously, the electric field component gives rise to electron oscillations perpendicular to the laser k-vector at a frequency equal to that of the laser. The component of the electron motion due to the $v \times B$ term is directed in the propagation direction of the laser and injects electrons at twice the laser frequency. For a linearly polarised pulse the longitudinal component of the pondermotive force is expressed [38] as:

$$f_x = -\frac{m_e}{4}\frac{\delta v_{osc}^2(x)}{\delta x}(1 - \cos(2\omega_L t)) \tag{2.31}$$

where v_{osc} is the electron quiver velocity and ω_L is the laser frequency. The first term corresponds to the non-oscillatory pondermotive push of the electrons in the forward direction, and the second term that of the $j \times B$ components which oscillates at twice the laser frequency.

This mechanism only occurs for a linearly polarised laser pulse due to the oscillating term and is most efficient at normal incidence onto the target due to reduced competition of mechanisms such as vacuum heating.

Under this scheme, at the vacuum-plasma interface, the electrons experience the pondermotive force of the laser which drives them beyond the critical density during one half laser cycle. The electrons driven beyond the critical are thus injected into the target at twice the laser frequency.

Under this mechanism, the energy gained by the electron population is correlated to the pondermotive potential of the laser pulse during the interaction [48]. It has been shown that the electron energy spectrum has a Maxwellian form with a finite cut-off energy and that the effective electron temperature scales as [48]:

$$k_B T_{hot} = m_e c^2 \left(\sqrt{1 + \frac{a_0^2}{2}} - 1 \right) \tag{2.32}$$

2.5 Plasma instabilities

The interaction of an intense laser pulse with a dense plasma can be subject to a variety of plasma instabilities. Some, such as streaming instabilities between electron-ion and ion-ion can result in the resonant exchange of energy between particle species [36, 37, 60] and can potentially be advantageous, particularly in the context of ion acceleration and absorption physics [61]. Others instabilities such as the Rayleigh-Taylor [62], and other transverse instabilities including Weibel [63], can be detrimental especially in the field of implosion driven ICF where it leads to inefficient compression of the fusion fuel [64], and ion acceleration where it has been shown to cause poor beam quality of radiation pressure accelerated ions [65]. The following section summarises the different instability mechanisms relevant to laser-ion acceleration and the roles they play.

2.5.1 Rayleigh-Taylor instability

The Rayleigh-Taylor instability classically is a two-fluid instability and can be thought of as a light and heavy fluid separated by a boundary. When the light

fluid pushes into the dense fluid, any interface perturbations will result in the growth of localised regions of the lighter fluid that propagates in the heavier. Some examples of such instabilities include supernova explosions where the material ejected is accelerated into the less dense gas surrounding it, the most famous example of which is that of the Crab Nebula.

Small perturbations in the interface between the two fluids means that locally there are differences in pressure applied, leading to the growth of regions of high and low density, similar to that illustrated in figure 2.8.

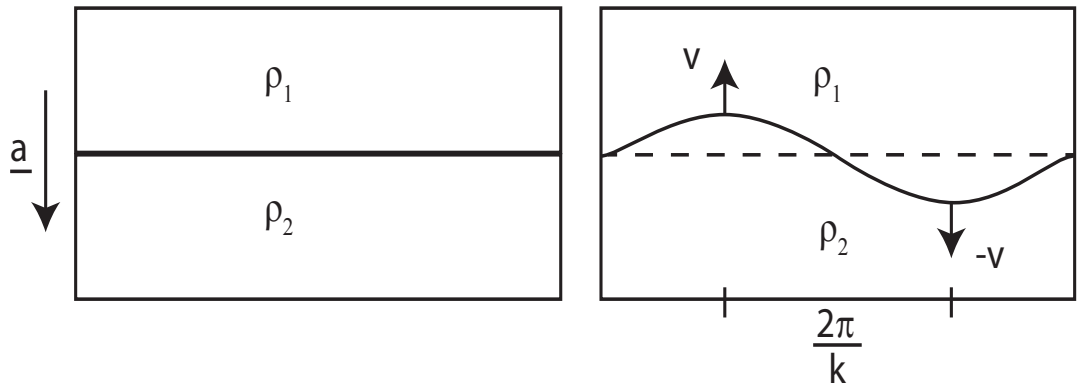

Figure 2.8: Schematic showing (a) the initial conditions of two fluids with different densities ($\rho_1 > \rho_2$) separated by a boundary and (b) a perturbed interface with peak and trough moving in opposite directions with the same velocity.

Acceleration of the low density fluid into the high density fluid results in the boundary between both becoming unstable and the instability growth is exponentially increasing. For a sinusoidal spatial perturbation, the amplitude of the initial perturbation will grow exponentially as [36] :

$$\xi = \xi_0 e^{\gamma_0 t} = \xi_0 e^{\sqrt{Aka}t} \tag{2.33}$$

where γ_0 is the instability temporal growth rate, $A = \frac{\rho_1 - \rho_2}{\rho_1 + \rho_2}$, ρ_1 and ρ_2 are the densities of the heavy and light fluids respectively, a the acceleration and k the spatial wavenumber.

Rayleigh-Taylor instabilities in intense laser interactions with ultra-thin foils in the radiation pressure acceleration regime have been inferred from spatial measurements of proton beams profiles, where bubble structures were observed [65].

The laser photons are considered as the light fluid and the target electrons the dense fluid. Any surface perturbations on the front surface of the target, from either surface structure or rippling of the critical density surface, act to seed the instability and enable the growth of localised regions of higher intensity, resulting in regions of higher photon pressure. In the regions of high intensity, electrons are pondermotively expelled radially resulting in a lower density.

The ion population will have the electron density profile imprinted onto it from the electrostatic field of the accelerated electrons resulting in a beam with bubble structures, which has been observed experimentally [65, 66].

2.5.2 Streaming instabilities

The two-stream instability is a form of beam-plasma instability where a population of energetic particles are injected into and stream through a plasma. The streaming together of the fast population with the background means that the relative drift velocities enables the excitation of wave modes in the plasma.

The beam of particles streaming into the plasma overtakes the background ions, resulting in an unbalanced space-charge leading to an electric field growth which acts to decelerate the fast particles, electrons or ions, and accelerate the background ions [67].

A small disturbance in the beam-plasma system will result in the propagation of a plasma wave accordingly. The plasma wave will have a characteristic electric field that acts to accelerate some of the particles in the beam, and decelerate others toward the initial perturbation point. This process results in a fluctuation in particle density due to the plasma wave electric field, which when the correct phase matching relationship is met, enhances the initial perturbation. The process will reinforce itself, resulting in growth of density fluctuations and of a longitudinal plasma wave enabling transfer of energy between particles [68]. This instability will have an exponential growth in the linear regime, continuing until the growth saturates and enters the non-linear regime.

A type of two-stream instability is the Buneman instability, which has been predicted to occur in the resonant energy transfer between electrons and acceler-

ated ion species in the relativistic transparency regime [61].

The dispersion relation for the simple case of a beam of electrons flowing into a background ion population, in the rest frame of the electrons is [36]:

$$\frac{\omega_{pe}^2}{\omega^2} + \frac{\omega_{pi}^2}{(\omega - kv_d)^2} = 1 \tag{2.34}$$

where ω_{pe} is the electron plasma frequency, ω_{pi} is the ion plasma frequency, and v_d is the relative ion drift velocity.

For the Buneman instability, the maximum growth rate possible is [36]:

$$\Gamma_{max} = \frac{\sqrt{3}}{2\sqrt{2}} \left(\frac{Zm_e}{m_i} \right)^{\frac{1}{3}} \omega_{pe} \tag{2.35}$$

The dispersion equation and maximum growth rate given above in equations 2.34 and 2.35 are for that of a fast electron population streaming with a cold ion background The corresponding dispersion and growth for the case of ion-ion streaming can be obtained by substituting the electron plasma frequency and drift velocity for that of the streaming ion population considered.

2.6 Summary

It has been shown that laser plasma interactions encompass a broad range of physics including but not limited to electromagnetic and plasma phyiscs which determine the coupling of laser energy into the plasma, quantum physics in the ionisation of matter by the laser pulse and relativistic effects in the motion of electrons who have gained energy in the intense laser field, to name but a few. These combined processes plus many more make laser-driven plasma interactions extremely complex in nature. To understand the complex processes that take place in such interactions often requires both numerical and theoretical modelling in the interpretation of experimental observations.

Chapter 3

Ion acceleration mechanisms in intense laser plasma interactions

The previous chapter presents an overview of the theoretical concepts in the interaction of an intense laser pulse with matter, in particular, in the overdense plasma regime. This chapter addresses mechanisms of ion acceleration, as well as the resulting ion beam properties. A brief overview of the history of laser-driven ion acceleration is provided, as well as the current status of the field and future outlook.

Since the development of CPA laser systems, and the resulting high intensities achievable, the acceleration of high flux ion beams to multi-MeV energies from overdense targets has led to intense interest in the field of laser driven ion acceleration.

Although ion acceleration from laser plasma interactions has been observed for numerous target types, solid density foil targets have been the subject of most studies and will be the primary focus of this thesis.

The ion response to slowly varying electric fields resulting from large charge separations is on a time scale :

$$\omega_{pi}^{-1} = (\frac{m_i}{m_e})^{\frac{1}{2}} \omega_{pe}^{-1} \tag{3.1}$$

Where ω_{pe} is the electron plasma frequency and m_e and m_i are the electron

and ion mass respectively. This shows that the ions response is on a much longer time scale than that of the electrons.

3.1 Introduction

Laser driven ion accelerators are particularly appealing for applications as they are compact, due to the much larger accelerating gradient (100's GVm^{-1} compared to 10's MVm^{-1} for conventional radio frequency based accelerators [69]) and high brightness. At the source, the duration of the accelerated ions is approximately that of the laser pulse duration although the typically broad spectrum and time of flight results in temporal stretching. This has led to intensive research into laser plasma based ion acceleration, particularly toward compact, optically tunable sources.

In the previous chapter, the motion of the plasma electrons and their collective response to an intense laser field has been discussed extensively while the motion of the plasma ions has been neglected. This is due to the fact that the plasma ions have a much larger mass, and their response to the laser field is much less than that of the electrons. The ion quiver velocity in the laser field is given by:

$$v_i = \frac{ZeE_0}{m_i \omega_L} \tag{3.2}$$

where Z is the ionisation state, e the electron charge, E_0 the peak electric field amplitude, m_i the ion mass and ω_L the laser frequency.

Due to this difference in mass, it is the electron motion and the subsequent charge separation fields resulting from that, which mediates the ion motion and acts accelerate them [38].

For the ions themselves to be significantly influenced directly by the laser field and reach near relativistic velocities, the laser intensity would need to be in excess of 10^{24} Wcm^{-2} which is out-with the peak intensities (10^{22} Wcm^{-2}) currently achievable at existing laser facilities. Planned multi-petawatt laser facilities such as ELI may make it possible to reach these relativistic ion acceleration conditions.

In the early days of ion acceleration from solid density targets driven by

intense short pulse lasers, there was somewhat of a controversy surrounding the source of the ions, with some arguing that they originated at the front surface and propagated through the target in the forward direction [70]. This conclusion was drawn from the annular nature of the proton beams observed and it was argued that this was due to deflection of ions by mega-gauss magnetic field within the target [70, 71]. It was shown that by cleaning of the contaminant layer on the rear of the target, forward ion emission was reduced, and that the source of the accelerated ions was thus concluded to be from the rear surface [72]. It was demonstrated that while there is both front and rear surface emission, the dominant sources of ions accelerated in the forward direction originated from the rear surface of relatively thick (>10 μm) targets and peak intensities $< 10^{20}$ Wcm^{-2} [73, 74].

3.2 Target Normal Sheath Acceleration

In the previous chapter, energy coupling from the laser pulse into the plasma via various absorption mechanisms creating a population of fast 'hot' electrons was discussed. The transport of this multi-mega Ampere fast electron through the target is subject to resistively generated field, filamentaion instabilities and Ohmic losses. These physical processes are not the subject of this thesis. A comprehensive review can be found in references [75–78].

The electron population produced at the front of the target travels through it, and as they reach the rear a fraction of the fastest escape the target [79]. This sets up a charge separation field, of the order of TVm^{-1}, strong enough to field ionise the rear surface atoms and accelerate the resulting ions. Expansion from the front surface can also occur due to ionisation of the front surface, with electrons blown off producing a similar sheath field, although with lower maximum ion energies.

Recirculation or 'refluxing' of the electrons within the target can occur because electrons are reflected in the sheath fields formed on both surfaces [5]. The electrons within the target effectively reflux between the two surface fields, with a fraction escaping at each boundary. The refluxing process acts to extend the

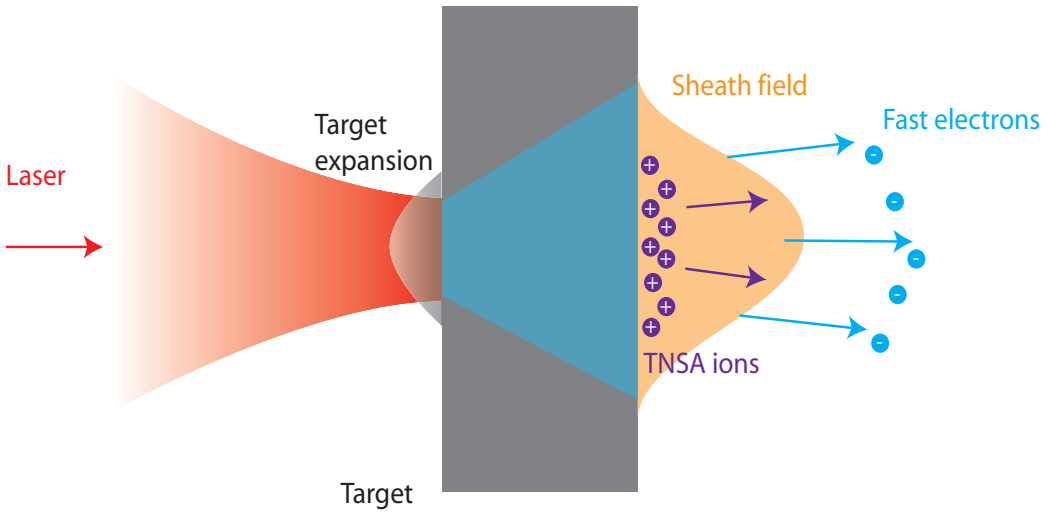

Figure 3.1: Schematic showing laser pulse interaction with solid target, transport of electrons through the target and sheath formation resulting in acceleration of contaminant ions from the rear surface in the TNSA regime.

lifetime of the fields and thus enhance the ion acceleration time leading to higher maximum ion energy [80].

The front and rear surfaces of the target have a thin layer of contaminant hydrocarbon layers, consisting of both hydrocarbon compounds and water vapour, leading to acceleration of energetic hydrogen and carbon ions from the sheath field [81] in addition to constituent ions.

Of particular interest are protons, which due to their high charge to mass ratio (q/m), these are typically the most efficiently accelerated ion species. In the case of multiple ion species, layering of the ion expansion with highest charge to mass ratio at the leading edge of the ion front occurs.

The extent of the charge separation sheath field is governed by the Debye length, given by equation 2.1. The resulting expansion is normal to the target rear surface and this is why the process is known as target normal sheath acceleration [5, 82].

By first considering the simplest model of the sheath field where the sheath remains static throughout the ion acceleration and a sharp step like ion density profile, the potential drop, $\nabla\Phi$, in the sheath for a hot electron population of

temperature, T_e, can be written as:

$$\nabla \Phi_s \approx \frac{T_e}{e} \tag{3.3}$$

The energy gained by an ion with charge Z in the potential will be:

$$\varepsilon_i \approx Ze\nabla \Phi_s \tag{3.4}$$

A more precise treatment of the charge separation potential and sheath field can be acquired by solving Poissons equation found in [43]. The magnitude of the sheath field at the rear of the target can be approximated [43, 82]:

$$E_0 = \sqrt{\frac{n_0 k_B T_e}{\epsilon_0}} \simeq \frac{k_B T_e}{e\lambda_D} \tag{3.5}$$

where k_B is Boltzmanns constant, T_e the hot electron temperature, n_0 is the electron density and λ_D the hot electron Debye length.

In reality the rear surface electrons are expanding out into the vacuum and the sheath field dynamics are temporally evolving. There are parallels that can be drawn between models of an electron-ion plasma expansion into vacuum and sheath acceleration, one such model is presented by Mora [83] is widely used. It is a 1-dimensional isothermal free expansion model of a plasma into vacuum and assumes that the plasma is locally neutral, that the ions are initially cold and static, a sharp boundary between the ion-vacuum boundary and an initial Boltzmann electron density distribution. For a simple plasma expansion, the ion density as a function of space and time can be expressed as [43]:

$$n_i(x,t) = n_0 \exp\left(\frac{-x}{(c_s t)} - 1\right) \tag{3.6}$$

which results in an exponential decrease spatially which is dependent on the expansion velocity, given by the ion acoustic velocity c_s.

The energy spectrum in the TNSA acceleration regime has an exponential

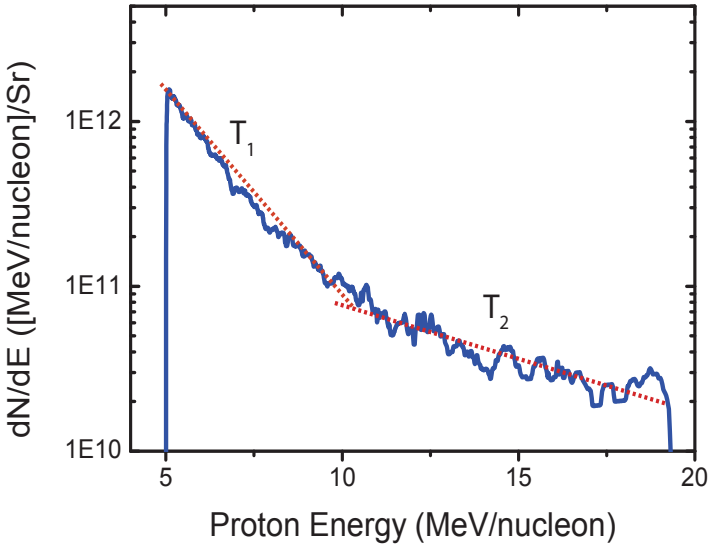

Figure 3.2: Example proton spectra in the TNSA regime.

from analytical solutions of the expansion model and is of the form given as:

$$\frac{dN}{d\varepsilon} = \left(\frac{n_{i0}c_s t_{acc}}{\sqrt{2\varepsilon\varepsilon_0}}\right)\exp\left(-\sqrt{\frac{2\varepsilon}{\varepsilon_0}}\right) \tag{3.7}$$

where $c_s = \sqrt{ZT_e/m_i}$ is the ion sound speed, t_{acc} is the acceleration time and $\varepsilon_0 = Zk_BT_e$.

An example proton spectrum in the TNSA regime is shown in figure 3.2. The spectra shows a two temperature distribution as has been shown to correspond to the fast electron population and cold return currents generated within the target [84, 85]. The ion spectrum has a finite high energy cut-off which is given by equation 3.8.

$$\varepsilon_{max} \simeq 2E_0[\ln(2\tau)]^2 \tag{3.8}$$

where $\tau = \omega_{pi}t/\sqrt{2e}$, is the normalised acceleration time. The acceleration time, $t_{acc} \simeq 1.3t_L$ has been inferred from PIC simulations, and has been shown to be in agreement with experimental results [86], where t_L is the pulse length of the laser.

As explained previously, the sheath field formed at the rear of the target results from fast electrons sourced at the front side, and so the spatial distribution of the

field will be dictated by that of the electrons as they emerge at the target rear.

The highest energy electrons are produced at the highest intensity region, the centre of the focal spot, with the energy decreasing radially with a Gaussian profile. This results in a sheath field on the rear of the target with a Gaussian 'intensity' profile.

The sheath area is determined by the divergence half angle of the hot electron population [73], θ, the radius of the focal spot, r_L, and the thickness of the target, l, and is given by:

$$S_{sheath} = \pi(r_L + l\tan\theta)^2 \tag{3.9}$$

The electron density dependence on the divergence of the electrons means that the sheath field will be strongest closest to the laser axis, where the electron density is highest. This results in an energy-dependent beam divergence of the accelerated ions, with highest energies having a smaller half angle than those of lower energy. Figure 3.3 (a) shows a schematic representation of this.

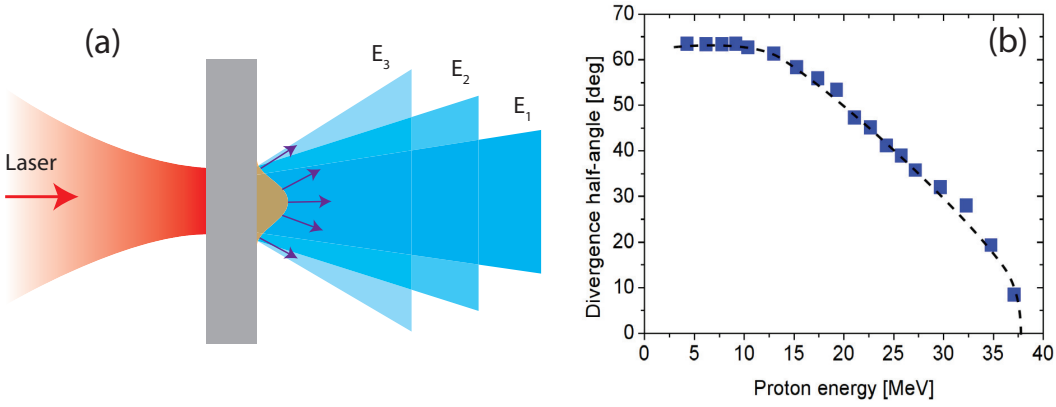

Figure 3.3: (a) Schematic showing the energy dependence TNSA ion beam divergence where $E_1 > E_2 > E_3$. (b) Experimental proton beam divergence measurements, adapted from [87].

One of the key challenges in the development of laser driven ion acceleration schemes is that of control of the beam properties. Control of ion energy is of particular importance. There have been numerous studies focussing on how the maximum ion energy achievable scales with the peak laser intensity.

Fuchs *et al* (2006) [86] and Robson *et al* (2007) [88], for example have shown

that for picosecond pulses, the maximum proton energy scales with the ponder-motive potential of the laser pulse, i.e. $(I_L\lambda^2)^{\frac{1}{2}}$ from equation 2.32.

Measurement of the TNSA source and expanding sheath field on the rear of the target were made by using grooved targets [89, 90] and transverse probing by a second TNSA ion beam to measure the electric field [15]. As shown above, it was found that the rear surface sheath had a radial Gaussian intensity profile resulting in a Gaussian ion spatial intensity distribution and were found to be approximately cylindrically symmetric around a central axis [90]. Measurements of the ion source size have also been made by using a metallic mesh placed a known distance between the target and the detector and using the magnification of the mesh projected onto the detector to calculated the sheath size with a source size diameter of ~ 100 μm measured [91].

Other techniques have also been employed to extend the lifetime of the acceleration including using dual laser pulsing [92, 93] and tailored targets consisting of a foil with quarter sphere to capture and re-focus the reflected laser light back onto the interaction region [94]

By using a dual laser pulse configuration, enhancement in coupling of energy from the laser into the TNSA ions resulting in a conversion efficiency of 15% for a pulse separation of 1 ps incident onto thin gold foils. As the pulse separation is increased further, the enhancement begins to diminish due to the decrease in proton density gradient from earlier expansion [93]. A similar approach was taken in earlier work by Scott *et al* [94] which utilised the fraction of the laser pulse reflected from the front surface which was refocussed resulting in an effective dual pulse resulting in enhancement in conversion efficiency to the TNSA protons. This method differentiates from the previous as the second pulse is of lower intensity, with the energy contained within it determined by the fraction reflected in the first interaction which was measured to be $\approx 40\%$. This approach enables energy that would typically be lost in reflection to be delivered back into the interaction and results in an experimentally observed enhancement in low proton energy region of the spectrum, with the degree of enhancement dependent on the duration between the pulses.

As the TNSA ions are accelerated normal to the rear surface, by employing convex curved target design, the ion beam can effectively be focussed and were considered with particular interest for application in the ion fast ignition ICF scheme [21, 25].

3.3 Radiation Pressure Acceleration (RPA)

Radiation pressure acceleration (RPA) is an alternative scheme of ion acceleration that has been proposed and has drawn considerable attention. In this scheme, the extreme light pressure exerted by the focussed laser pulse directly accelerates electrons in the focal spot volume, setting up an electrostatic field due to charge separation which accelerates the ions, and theoretically lead to a mono-energetic ion energy distribution.

There are two distinct modes of RPA that are considered in the following sections. Hole boring (HB) in which the laser incident on the front surface of an overdense target pondermotively drives the electrons at the critical surface into the target causing profile steepening. The electrons displaced create an electrostatic field that in turn accelerate the ions. Light sail (LS), where if the target is sufficiently thin, the electrons in whole target volume irradiated in the focal spot can be accelerated, with the resulting charge separation field accelerating the ions.

The pressure exerted by an intense laser pulse can be approximated by conservation of momentum [95]:

$$P_{rad} = (2R + A)\frac{I_L}{c} \tag{3.10}$$

where R is the reflectivity of the laser pulse from the target, A is the fraction of the laser pulse absorbed, and I_L is the laser intensity.

The scaling of maximum ion energy from radiation pressure is predicted to be much more favourable than that of TNSA. Simulations and theoretical work have predicted that for a linearly polarised laser pulse, a peak intensity of $\simeq 10^{23}$ Wcm^{-2} is required such that RPA will be the dominant mechanism for the

acceleration of ions [96].

Other simulation work has shown that for more modest intensities available with present laser systems, by using circular polarisation the pondermotive heating of electrons and subsequent expansion is suppressed, and the target electrons compressed and driven forward under the radiation pressure [54, 97] thus making RPA effective at presently achievable intensities.

RPA can be discussed in terms of the radiation pressure on a perfectly reflecting surface ($A = 0$ and $P_{rad} = 2I/c$) moving at a velocity $v = \beta c$. Circular polarisation is assumed in order to suppress electron heating and absorption can be neglected. In this case the surface is considered as a moving mirror with the reflectivity from the surface a function of frequency, $R(\omega')$, in the rest frame. The radiation pressure in both the laboratory and rest frame is the same and can thus be expressed:

$$P_{rad} = P'_{rad} = \frac{2I}{c} R(\omega') \frac{1-\beta}{1+\beta} \tag{3.11}$$

where the relationship between the incident and reflected frequencies due to the Doppler shift in the rest frame is given by:

$$\omega' = \omega \sqrt{\frac{1-\beta}{1+\beta}} \tag{3.12}$$

3.3.1 Hole Boring

In the hole boring mode of RPA, in the case of a thick target and sufficiently high intensity, the laser at the critical surface pushes the critical density layer into the target, due to the radiation pressure being greater than the plasma thermal pressure $P_{rad} > P_{th}$.

The electrons are driven forward into a compressed layer from their initial position and leave a depleted region behind, with ions only and causing a charge separation field to be set up. It is this field that acts to accelerate the ions as they will not be directly influenced by the laser pulse, and so the electrons being much lighter act to mediate the ion motion.

In the case where the electrons are driven to relativistic velocities, the effect on the electron mass must be considered. A model for the relativistically corrected hole boring velocity has been developed [98, 99] to account for these effects:

$$\frac{v_{hb}}{c} = \frac{\sqrt{\Xi}}{1+\sqrt{\Xi}} \tag{3.13}$$

where $\Xi = \frac{I_L}{n_i m_i c^3}$

From this it can be seen that the hole boring velocity depends only on the incident laser intensity, the target density and the ion mass.

In this model, the maximum ion energy obtained after acceleration is:

$$E_i = m_i c^2 \left(\frac{2\Xi}{1+2\sqrt{\Xi}} \right) \tag{3.14}$$

The hole boring phase lasts up until the point where either hole boring front reaches the back of the target or until the laser pulse has ended [100].

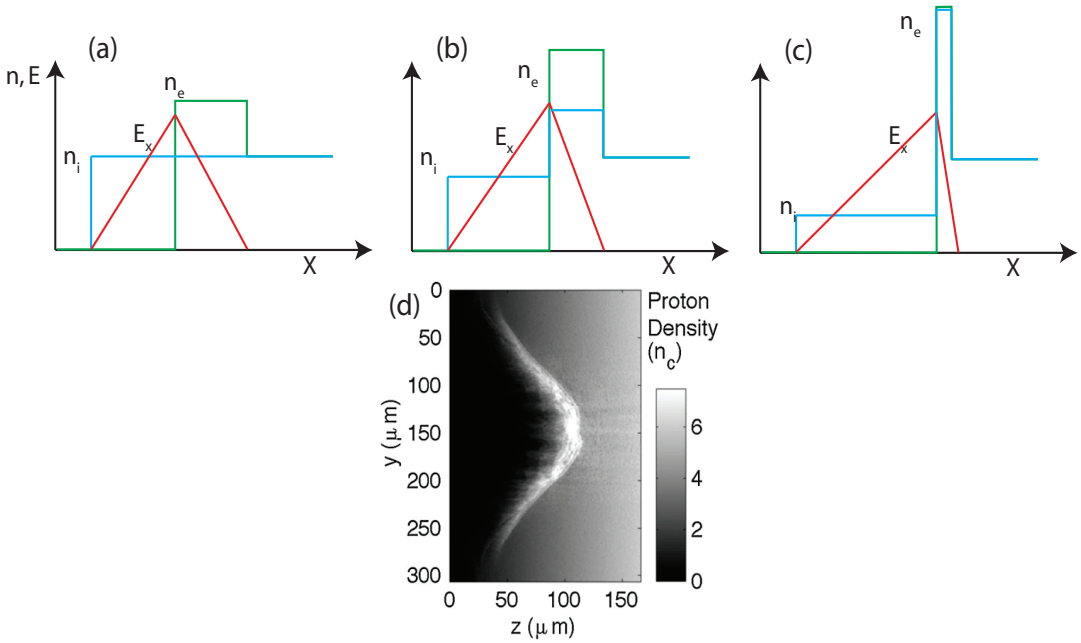

Figure 3.4: Hole boring schematic (adapted from [43]) showing (a)-(c) the temporal evolution of the hole boring front, with increasing time from (a)-(c), including the compression in electron density, the depleted region behind and the corresponding longitudinal electric field and (d) 2D PIC simulation result of target electron density in the HB RPA mode at a fixed time from [101].

Ions accelerated in the hole boring RPA regime are predicted to have a quasi-

monoenergetic spectra, with the ion energy scaling proportional to the incident laser intensity, $E_i \propto I_L$ (providing a more favourable scaling than the TNSA mechanism which scales as $E_i \propto I_L^{\frac{1}{2}}$).

The compressed electron layer driven by the laser forms an electrostatic shock which propagates through the target, with ions behind being accelerated by the associated field, as shown in figure 3.4. However the shock launched is also able to reflect bulk ions preceding it, and accelerate them in the process. This is known as colisionless shock wave acceleration and will be discussed in further detail in section 3.5.

As discussed above, the HB phase lasts up until the ions leave the back of the target or the laser pulse has left the system. For ultra thin targets this can occur very quickly and the acceleration phase switches to the light-sail RPA mode.

3.3.2 Light Sail

For ultra-thin targets of the order of tens of nanometres, the whole target volume may be accelerated by the laser radiation pressure. In the light sail mode of RPA, all of the target electrons within the focal spot volume are accelerated forward by the photon pressure, accelerating the ions and thus the whole target propagates forward with the laser pulse.

As before with hole boring, for currently available laser systems and intensities, the use of circular polarisation and suppression of target expansion and sheath acceleration means that RPA signatures can be observed from ultra-thin targets.

Work by Kar *et al* [102] has shown experimental evidence of narrow energy spread spectral features in ion spectra from pico-second interaction with ultra-thin foils. Spectra measured at varying angles with TP spectrometers and RCF indicate that the beam has a narrow divergence angle of $\simeq 13°$, in agreement with predictions of a less divergent beam compared with sheath acceleration [102].

It was also found that for pico-second duration pulses, the difference between circular and linear polarisation was negligible in contrast to that predicted by theoretical and simulation work [96, 102].

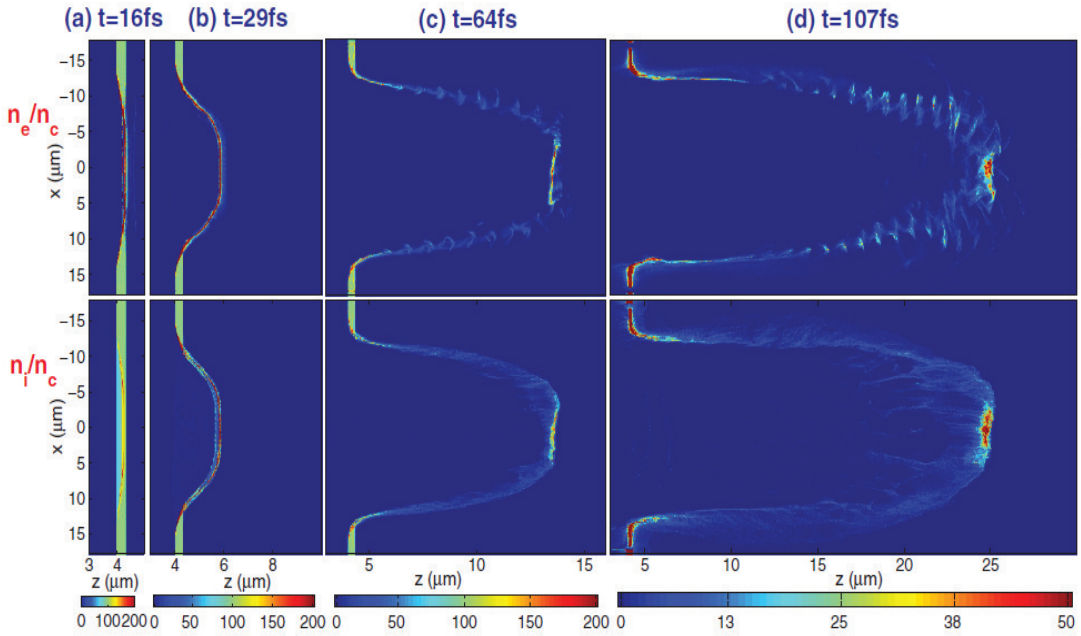

Figure 3.5: 2D PIC simulation of Light Sail RPA, from [103], showing the temporal evolution of (top) target electron density and (bottom) ion density. The laser is incident from the left.

The electrons driven forward by the radiation pressure result in a depletion of electrons from the focal region and a strong charge separation field between the electrons and ions. The charge separation field set up acts to accelerated the ions that then co-move with the electrons, as shown in figure 3.5.

The velocity imparted to the target which is accelerated under radiation pressure can be calculated by the conservation of momentum between the laser and the target, and is given as:

$$v_{ls} = \frac{(2R + A)\tau_{acc}}{n_{i0} m_i d} \frac{I_L}{c} \tag{3.15}$$

where d is the target thickness. From equation 3.15 it can be seen that the scaling of ion energy will be $E_i \propto I_L^2$ in the non-relativistic ion energy regime. The acceleration time of the foil $\tau_{acc} \approx \tau_L$ is approximately that of the pulse duration of the laser pulse.

Previous theoretical work has shown that in the light sail mode of RPA, the maximum energy of the ions and the conversion efficiency, $\varepsilon_{i,max}$ and η, are given

as follows in equations, 3.16 and 3.17, respectively [96, 104]:

$$\varepsilon_{i,max} = \frac{2E_L}{2E_L + N_i m_i c^2} \frac{E_L}{N_i} = 2m_{ic^2} \frac{(\mu s N)^2}{1 + 2\mu s N} \tag{3.16}$$

where $N_i = n_i dA$ is the areal density of the target encircled within the focal spot, $N = c\tau_L/\lambda_L$ the number of field cycles contained within the duration of the laser pulse, $\mu = m_e Z_i/m_i$ and $s = a_0^2/\sigma$ with $\sigma = \dfrac{n_e l}{n_{crit}\lambda_L}$ is the normalised areal density to critical density.

$$\eta = \frac{N_i \varepsilon_{i,max}}{E_L} \tag{3.17}$$

As the velocity of the light sail approaches c, the reflected light is Doppler red shifted and energy is transferred to the accelerated plasma slab as discussed with consideration to the moving mirror model in the previous section.

The frequency of the reflected light is quantitatively given by $\omega_r = \frac{\omega_L}{4\gamma^2}$, where ω_L is the initial laser frequency and γ the electron Lorentz factor.

As the foil approaches c ($\gamma \gg 1$), the energy reflected is significantly reduced due to the Doppler red shift and a large fraction of the energy transferred to the foil in the form of kinetic energy [105, 106].

3.3.3 Plasma surface dynamics

With such a large pressure exerted on the target surface localised variations in density or surface structure can act to seed transverse Rayleigh-Taylor like instabilities, such as those discussed in the previous chapter, which can cause break up of the beam [106, 107]. The growth of such instabilities is detrimental to the efficient acceleration by radiation pressure in the light sail mode.

For both the relativistic and non-relativistic case, the growth time of the instability is given as [105, 107, 108]:

$$\tau_{rel} = \frac{a_0}{3c} \sqrt{\frac{Z_i m_e n_{crit}}{2k^3 l m_i n_e}} \tag{3.18}$$

$$\tau_{non-rel} = \frac{1}{a_0 c}\sqrt{\frac{l m_i n_e}{2k Z_i m_e n_{crit}}} \tag{3.19}$$

The growth of RT instabilities in electron density is mapped into the ion population and results in a bubble-like profile to the beam, an example of which is shown in figure 3.6.

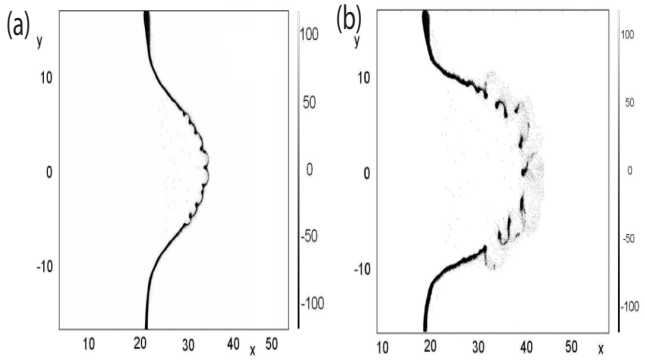

Figure 3.6: Temporal evolution of electron density for Rayleigh-Taylor unstable acceleration in the LS mode in 2D PIC simulations from [106]. (b) is taken from a later time step than (a).

Observations of beams exhibiting these properties have been made by Palmer *et al* [65] and are a signature that radiation pressure acceleration is playing a significant role in the interaction. Further discussion of there effects, in the context of the results presented in this thesis, is given in chapter 4.

3.4 Break-out Afterburner (BOA)

In the mechanisms of ion acceleration that have been discussed above, the target remains opaque to the laser pulse throughout the interaction. In the case of ultra-thin targets however, this is more difficult to achieve in practice, requiring ultra-high contrast laser pulses and circular polarisation to minimise heating and target pre-expansion.

If sufficient target expansion occurs driven by the rising edge of the laser pulse, the target may become relativistically transparent during the main interaction, due to the decrease in peak density and the relativistic increase in the critical density, as discussed in chapter 2.

Although in the RPA regime transparency of the target reduces the efficiency of ion acceleration and overall ion energies, other mechanisms of energy exchange are predicted to occur [7]. The radiation pressure from equation 3.11 can be rewritten since $R + T + A = 1$, where T is the fraction of the laser pulse transmitted, as:

$$P_{rad} = (1 + R - T)\frac{I_L}{c} \tag{3.20}$$

From this it can be seen that transmission of the laser pulse diminishes the radiation pressure resulting in less efficient acceleration. However, the fraction of the laser pulse transmitted can volumetrically heat target electrons, enhancing sheath accelerated ions. One such mechanism is known as the laser breakout afterburner (BOA). The dynamics of the BOA mechanism have been studied numerically in multi-dimensional PIC simulations, [109–112], and theoretical studies [61, 113], and shown promising enhancements in both the laser to ion conversion efficiency and maximum ion energy. Experimental results have shown that in this regime, considerable enhancement in the maximum energy of bulk carbon ions from nanometre thick diamond-like carbon targets occurs [114–116], while there is also evidence of enhancement of protons [114].

The physical picture of the BOA mechanism. as shown schematically in figure 3.7 can be summarised as follows. The laser pulse interacts with the front side of the target, heating electrons via the various absorption mechanisms discussed in section 2. At this point the laser pulse can only influence up to the skin depth or region of hole boring into the target, though if the target is thin enough then this could be a considerable fraction of the overall thickness. The electrons heated by the laser pulse initialises expansion of the bulk target, decreasing the electron density in the region of the focal spot.

As described in the previous chapter, the relativistic motion of the electrons in the laser field results in relativistic effects at the interaction region, with the critical density increasing by a factor of γ and the skin depth increasing by $\sqrt{\gamma}$.

The target expansion coupled with the relativistic critical density increase and skin depth effect means that a point will be reached when the target will

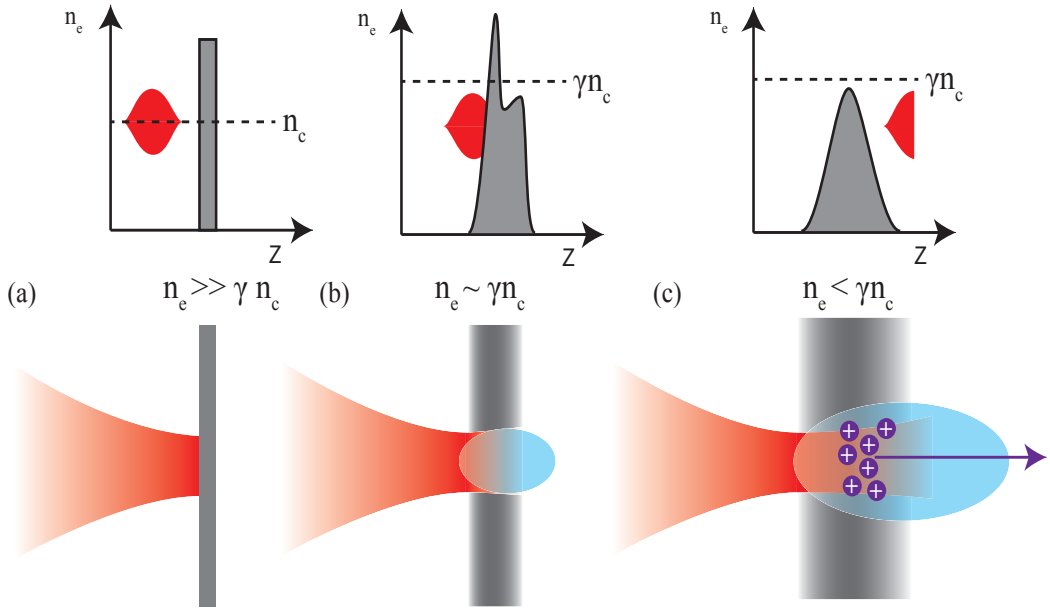

Figure 3.7: Schematic representation of the temporal evolution of (a) the electron density and (b) the BOA mechanism. Adapted from [1]

become relativistically transparent to the incident laser pulse and the remaining laser pulse fraction will be transmitted through the target. Another way by which the relativistic induced transparency conditions can be achieved is due to the compression and profile steepening at the front surface of the target. A combination of the increased critical density and skin depth due to the relativistic mass increase of the electrons, coupled with the reduction in effective target thickness to the order the plasma skin depth, results in transmission of the laser pulse through the target [1]. Relativistic induced transparency is one of the key features of the BOA mechanism.

As the target becomes transparent to the laser pulse, the propagating laser volumetrically heats the bulk electrons. The onset of transparency changes the dynamics from a surface dominated interaction to one where the collective electron response to the laser pulse throughout the whole volume of the target dominates [117].

The electrons accelerated by the presence of the laser field are co-directional with the ions, which move much slower due to the mass difference. The relative drift velocities between the two species results in the unstable growth of a plasma

wave excitation via the relativistic Buneman instability [61]. The phase velocity of the plasma wave excitation when it matches the drift velocity of the expanding ions transfers energy resonantly resulting in acceleration of the ions [61, 115].

Later in time, as the target has been strongly expanded, the electron density will have dropped such that the conditions for Buneman instability growth are less favourable and efficient energy transfer can no longer occur.

The maximum ion energy in the BOA regime has been shown analytically to scale with the electron temperature and a parameter α, which describes the coupling efficiency between the ions and electrons has been inferred from PIC simulations to be 3, according to [7, 118, 119]:

$$\varepsilon_{i,max} \simeq (1 + 2\alpha) Z T_e \tag{3.21}$$

For the most efficient acceleration via the BOA mechanism to occur it is necessary that the point at which relativistic transparency occurs is close to or at the peak of the laser pulse [115].

Previous work has investigated the BOA mechanism in the context of the enhancement to the bulk heavy ions of the target while the protons with higher charge to mass are 'self-cleaned' from the target interaction due to sheath expansion [110]. By using pure hydrogen targets or targets with large quantities of hydrogen in the bulk target, BOA is predicted to result in efficient proton acceleration. Reduction of the target pre-expansion prior to the main pulse arrival, by improvements in laser contrast, would also enable proton enhancement in the BOA regime.

3.5 Shock wave acceleration

Up until this point, ion acceleration from initially solid targets has been discussed. However, in near critical density laser plasma interactions, a scheme of ion acceleration known as colisionless shock-wave acceleration has been proposed as an alternative mechanism for the acceleration of ions [120–126].

In this scheme electrons at the critical surface are snow-ploughed due to hole

boring, causing a dense electron bunch and propagating electrostatic field into the target. Upstream of the shock front, ions may be reflected from the propagating shock front and those that are will achieve a velocity $v_i = 2v_{shock}$, where v_{shock} is the shock velocity.

For the shock to be considered collisionless it must satisfy the condition that the shock velocity is greater than the ion sound speed (a Mach number $M > 1$), as:

$$M = \frac{v_{shock}}{c_s} > 1 \tag{3.22}$$

Driven by radiation pressure, the initial shock velocity can be found as shown previously in section 3.3, and from this the energy of the ions reflected from the shock front will be:

$$E_i = 2m_i v_{shock}^2 \tag{3.23}$$

This applies for a constant shock velocity, and the spectrum of ions in this case would be close to mono-energetic [43].

Experiments investigating shock acceleration from near critical density gas jet targets irradiated by CO_2 lasers of ~ 10 μm wavelength [101], have demonstrated quasi-monoenergetic ion energy spectra attributed to hole boring from the front surface driving a shock and subsequent ion acceleration due to reflection, showing promising scaling of ion energy for applications [101, 123].

Similar experiments with CO_2 lasers by [123] present a different interpretation based on the launch of a collisionless shock wave and subsequent reflection of ions. The combination of overdense gas jet targets and gas laser means that a high repetition rate can be achieve, and coupled with the mono-energetic spectra obtained experimentally make this a promising scheme of laser ion acceleration for applications [43, 123].

3.6 Summary

To date, the TNSA mechanism has attracted considerable attention since such ion beams were observed since the advent of short pulse CPA laser systems. However research into new mechanisms of laser driven ion acceleration from ultra-thin targets show considerable promise with more favourable scaling of the maximum ion energy, increased efficiency in conversion of energy to ions, and the possibility of optical control of the ion properties toward applications. The work presented in later chapters of this thesis presents experimental and numerical investigations of these properties toward optimisation of the acceleration of protons from ultra-thin foils in the relativistic transparency regime.

Chapter 4

Enhanced laser energy coupling to protons via a self-generated plasma channel during RIT

Since the advent of CPA, the acceleration of fast ions from solid density targets has been the subject of intense study. Target normal sheath acceleration (TNSA) is capable of accelerating ions to multi-MeV, short pulses, of ions energies over short distances. In the TNSA regime, the ion beam has a thermal energy spectrum and unfavourable maximum energy scaling with intensity, as described in chapter 3.

The potential application of such ion beams, including hadron therapy, radiography and fast ignition fusion all necessitate the enhancement in flux, laser-ion conversion efficiency and most crucially optical control of the ion beam properties. Hadron therapy also requires a significant increase in the maximum ion energy. The requirements of a 'useful' ion beam for these types of applications are, high flux and narrow energy spread, as well as the ability to control the maximum energy depending on the application. These requirements have driven intense study in recent years into new mechanisms of ion acceleration such as Radiation Pressure Acceleration (RPA) and the Break-out Afterburner (BOA), as introduced in chapter 3.

In nanometer-thick foil interactions there are several distinctly different ion

acceleration mechanisms that can occur over the duration of the laser pulse. Target normal sheath acceleration (TNSA), as a result of fast electrons transported through the target forming an electrostatic field at the rear side accelerating ions into a relatively divergent beam with a thermal spectral distribution [82]. Radiation pressure acceleration (RPA), when the target surface is driven forward by the intense pressure of the focussed laser [96], is predicted to result in a higher energy and less divergent beam with a narrow energy spread [102, 147]. In the case where the target expands and undergoes relativistic-induced transparency (RIT) [148], volumetric heating of the electrons by the transmitted portion of the laser pulse has been demonstrated to enhance the maximum energy of the TNSA ion population in what is known as the break-out afterburner (BOA) scheme [109, 114]. The electrons heated by the transmitted laser pulse are thought to transfer energy to the co-directional ions via the relativistic Buneman instability [61]. The energy transfer mechanism is investigated numerically in chapter 5. In reality, multiple acceleration processes can take place during the temporal evolution of the interaction depending on the laser and target parameters. Diagnostic techniques employed in the measurement of the ion properties are time-integrating making deconvolution to investigate one particular aspect of the acceleration problematic.

In this chapter, by spatially separating the components of the ion beam, the examination of the individual acceleration mechanisms is enabled. As well as the presence of TNSA, RPA, and BOA enhanced acceleration processes, enhancement in energy coupling to ions by a plasma jet in near critical density expanded plasma during RIT. Energy coupling from the laser to the background ions over an extended length is demonstrated. Multi-dimensional PIC simulations aid in the understanding of the temporal evolution of the interaction and assist in the interpretation of the experimental measurements.

4.1 Experimental method

The petawatt arm of the Vulcan laser system, as described in chapter A, was configured to deliver either a single or dual pulse to investigate the acceleration of fast ions from ultra-thin foils.

The Vulcan petawatt laser delivered $E_L = 200 \pm 15J$, in a pulse of duration $t = (1.0 \pm 0.2)$ ps FWHM onto target. The laser was focussed by an $f/3$ off-axis parabola to a focal spot of diameter $d_L = 7\mu$m FWHM, giving a peak intensity of 2×10^{20} Wcm^{-2}. The laser pulse was linearly polarised, p-polarised for the case of oblique incidence.

As described in chapter A, the Vulcan petawatt laser can also be configured to deliver a dual pulse by splitting the main pulse after the picosecond OPCPA pre-amplification stage. In dual pulse mode, the energy between the two pulses was fixed but the energy ratio between the two pulses was varied. The pulses had a temporal separation of (1.5 ± 0.1) ps and the intensity ratio of the pre-pulse was varied to modify the rising edge of the main pulse.

The changes to the rising edge intensity profile of the main pulse are quantified by the introduction of the parameter I_{RE}. This is defined as the ratio of the intensity on the rising edge to the peak intensity, I_L, at a time 1.5 ps prior to the main pulse. This time is selected arbitrarily to provide a parameter to quantify the intensity rising edge profile on the picosecond time scale. For ultra-thin foil interactions, a high contrast laser pulse is required and so a single plasma mirror was used in the main focussing beam to enhance the contrast. The value of $I_{RE} = 0.04I_L$ corresponds to the nominal single pulse condition after plasma mirror contrast enhancement and the value of I_{RE} was varied from $0.04 - 0.2I_L$. Studies of plasma mirror reflectivity and it's response in dual pulsing modes have shown that up to a temporal separation of $\sim$5 ps, the quality of the near and far field of the focal spot are maintained [149].

Figure 4.1 shows an example contrast measurement of the TAP laser pulse. The measurement is made of the combined ps and ns OPCPA pre-amplifiers, stretcher and compressor. After the ns-OPCPA stage the pulse is sent to the

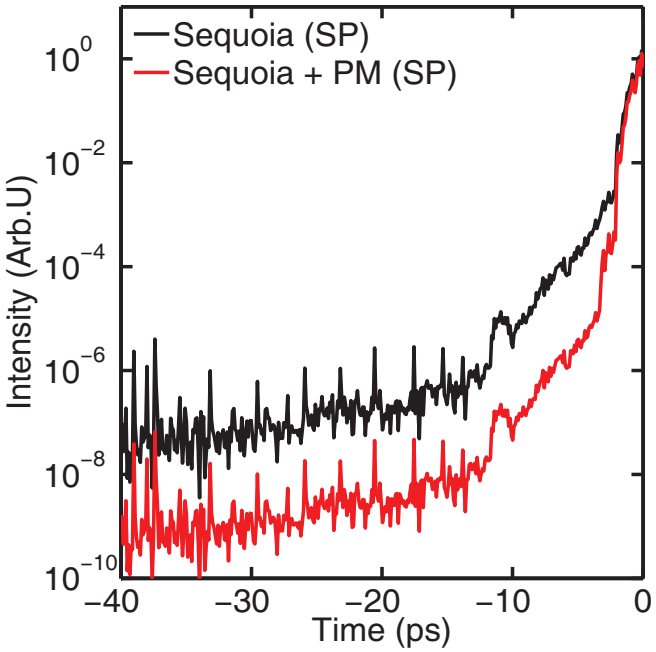

Figure 4.1: Contrast measurement of the combined ps and ns OPCPA pre-amplification stages using a third order scanning cross-correlator [2] - black; Modelled contrast enhancement due to the plasma mirror - red.

compressor chamber, by-passing the main amplification chain. This enables a high repetition rate to be achieved (no waiting is necessary for cool down of the amplifiers) and thus enables a Sequoia, third order scanning cross-correlator to be used.

Figure 4.1 shows the contrast measurement from -40 ps prior to the main pulse, and the calculated contrast enhancement due to the plasma mirror (PM), modelled from experimental reflectivity measurements [3].

The reflectivity measurements were made by measuring the specular reflectivity from the PM as a function of intensity. The intensity incident on the PM was varied by (a) moving the PM in the focussing plane of the laser, changing the incident spot size, and (b) by decreasing the energy in the pulse. Reflectivity as a funtion of intensity on the plasma mirror are shown in figure 4.2.

The plasma mirror setup employed consisted of a single anti-reflection coated plasma mirror inserted into the focussing beam of the main pulse at 4.5 cm from the focal spot and operated at an intensity of 3.6×10^{15} Wcm^{-2}, corresponding to a maximum in reflectivity for a 500 fs pulse as shown in reference [3, 131] and illustrated in figure 4.2.

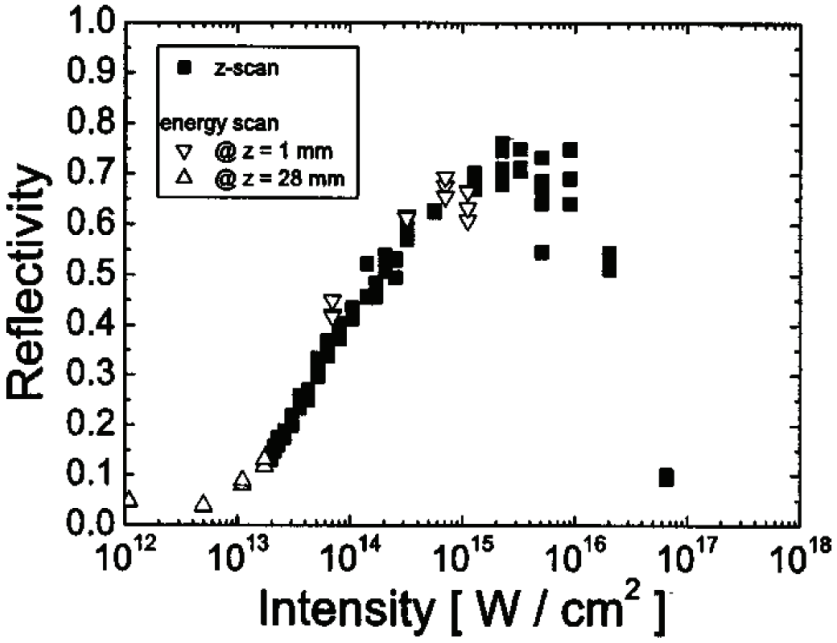

Figure 4.2: Specular reflectivity measurements for a pulse duration of 0.5ps. The intensity was varied by moving the target out of focus (squares) and by decreasing the laser energy (triangles). Adapted from [3].

The reflectivity data in the range of $1.0 - 3.6 \times 10^{15}$ Wcm^{-2} from figure 4.2 was used in the modelling of the plasma mirror enhancement of the TAP contrast as shown in figure 4.1. The intensity axis is normalised to the value for which reflectivity is optimum and is taken as the operating intensity of the plasma mirror. The reflectivity in this range is plotted on a linear scale with the normalised intensity. A logarithmic fit is made to the experimental data and is also shown plotted in figure 4.3.

To calculate the predicted enhancement to the laser pulse contrast due to the PM, the peak of the pulse trace in figure 4.1 at $t = 0$ is set to be 3.6×10^{15} Wcm^{-2}, the intensity of maximum reflectivity and the contrast measurement is normalised to this reference intensity.

The function fitted to the reflectivity measurements is applied iteratively as a function of the intensity contrast measurement represented by the black curve in figure 4.1. Each point on this gives a reflectivity value based on the contrast intensity measurement. The reflectivity calculated as a function of intensity is applied to the initial contrast measurement to give the expected contrast enhancement from the PM, shown as the red curve in figure 4.1

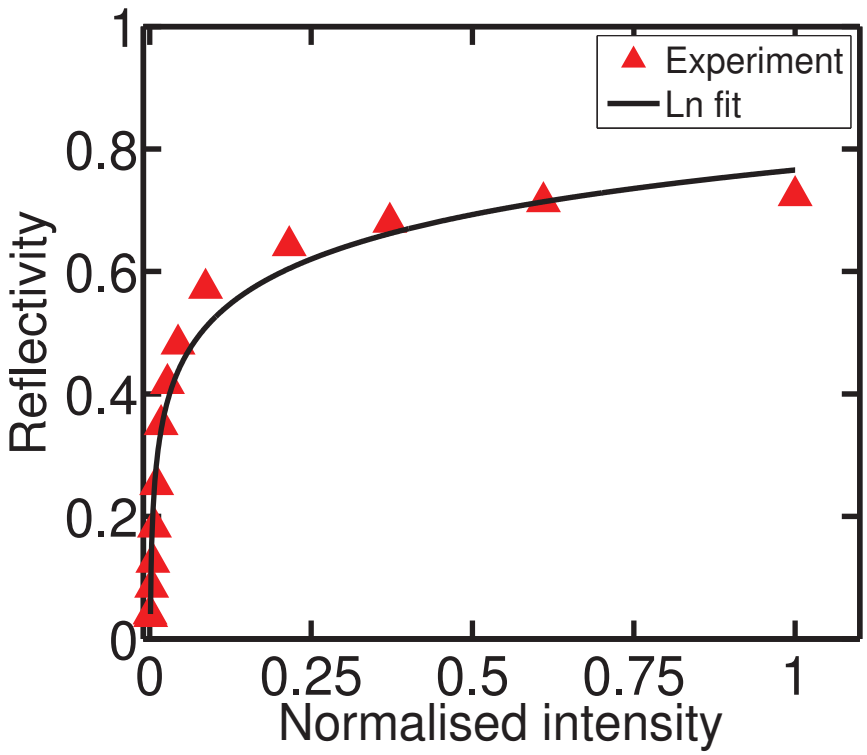

Figure 4.3: Reflectivity as a function of intensity (normalised to the peak intensity). A logarithmic fit is also plotted

It is worth noting that this process has only been applied to the rising edge of the pulse and not the falling edge for a number of reasons. Firstly, it is primarily the rising edge that is of interest in the context of the work presented, and post pulse effects have not been considered. Secondly is that once the plasma has been initialised, or 'switched on', by the main pulse the intensity on the falling edge of the pulse will be fully reflected.

Quantification of the contrast, the leading edge intensity profile of the main pulse and it's significance in the context of thin foil interactions will be explored in further detail as part of the discussion in section 4.4

After reflection from the plasma mirror, the focussing laser pulse irradiates aluminium targets of 10 nm and 40 nm thickness at both normal and oblique (30°) incidence.

A range of diagnostic techniques were used to measure various properties of the interaction. The 2D spatial intensity distribution of the proton beam was measured at discreet energy steps using stacked RCF dosimetry film. The stack

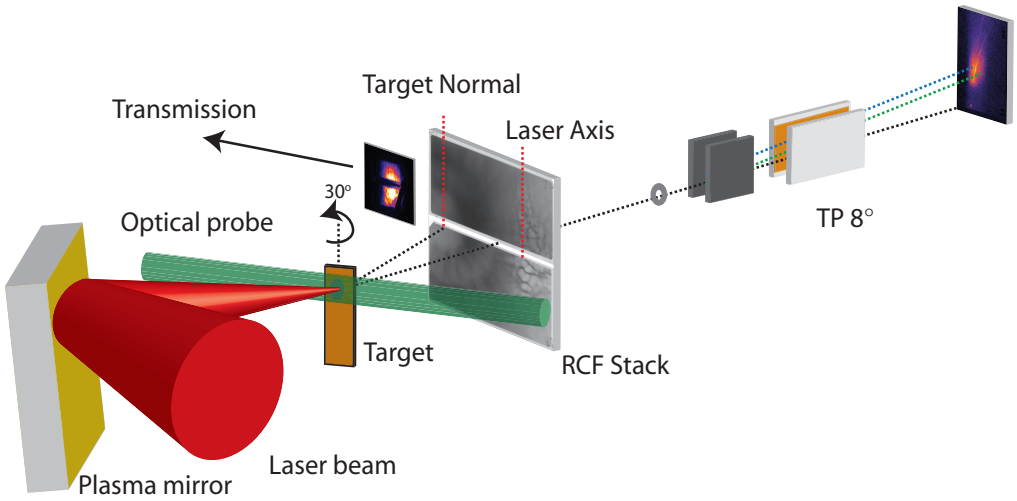

Figure 4.4: Schematic illustration of the experimental arrangement and the key diagnostics.

was at a distance of 75 mm from the target and enabled an angular range of -10 to 35° to be measured in the horizontal plane with respect to the laser axis. This angular range allows for both the laser axis and target normal components of the proton beam to be measured when shooting at oblique incidence, as shown in figure 4.4

The RCF stack was built of two halves. A slot in the middle enables a line of sight for a suite of high resolution TP spectrometers [136] covering an angular range of 36°. There were 5 spectrometers, positioned at discreet angles of -6, 0, 3, 8 and 30° with respect to the laser propagation axis. The dispersed ions from the TP spectrometer were recorded on imaging plate calibrated for extraction of the total ion flux. In this way the spectrum was measured for both protons and heavy ions, with a low energy detection threshold of 5 MeV for protons.

The percentage of transmitted light through the target, in both the fundamental and second harmonic, was measured by imaging of a thin PTFE scatter screen placed at the front of the RCF stack. While the second harmonic is typically produced at the front surface, measurement of the second harmonic has also been used in the diagnosis of channel formation in near critical density plasmas [51]. A fibre connected to a spectrometer, collecting light from the scatter screen also enabled the transmitted light to be spectrally resolving using an optical spectrometer. A transverse optical probe was also used to probe the target expansion

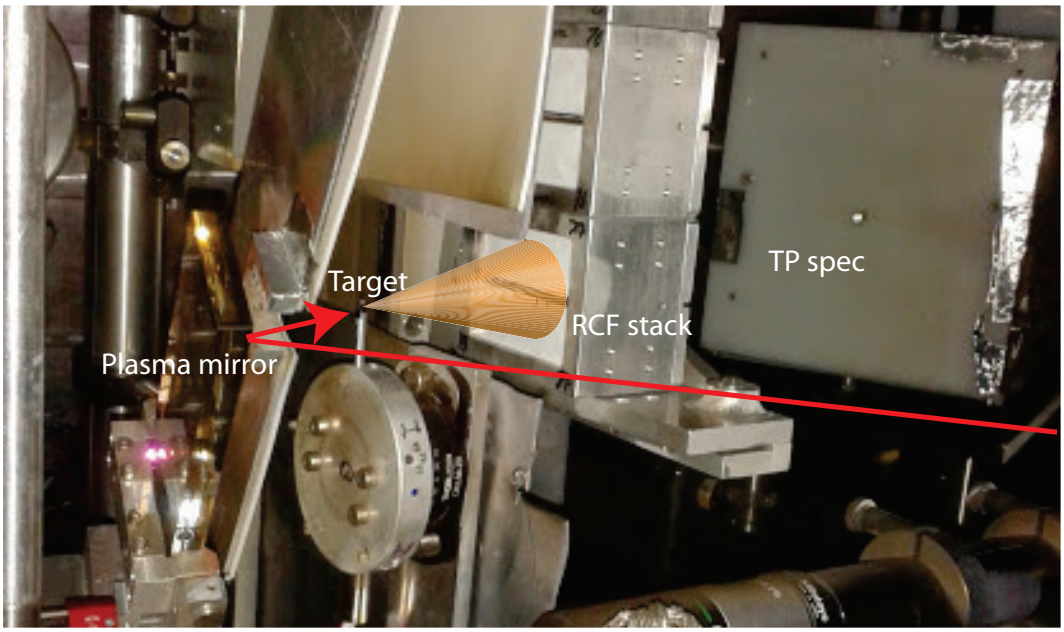

Figure 4.5: Picture taken within the TAP interaction chamber showing the experimental arrangement of the slotted RCF stack and the target normal (30°) TP spectrometer, as well as the plasma mirror and target. The laser axis is also marked. The expanding proton beam is marked by a cone.

dynamics at different temporal steps ranging from t = -20 to 150 ps with respect to the main pulse interaction time.

A schematic layout of the diagnostic set-up is shown in figure 4.4 as well as a picture of the setup in the chamber itself in figure 4.5. The picture shows a close up of the PM, target, RCF stack 'ladder' (which enables four shots to be taken before recycling the vacuum chamber) and the TP spectrometer at 30°. The other spectrometers are outside the image as they are situated further from the interaction. Detailed discussion of the individual diagnostic methods is provided in chapter A.

4.2 Experimental results

In the interaction of an ultra-intense laser pulse with an ultra-thin foil undergoing RIT, multiple acceleration mechanisms can to take place. By angling the target with respect to the optical axis of the laser, the individual components which typically all overlap for normal incidence, can be spatially separated and the

characteristics of the individual components investigated. The case of a single laser pulse normally incident upon an aluminium foil target of thickness $L = 10$ nm is considered first.

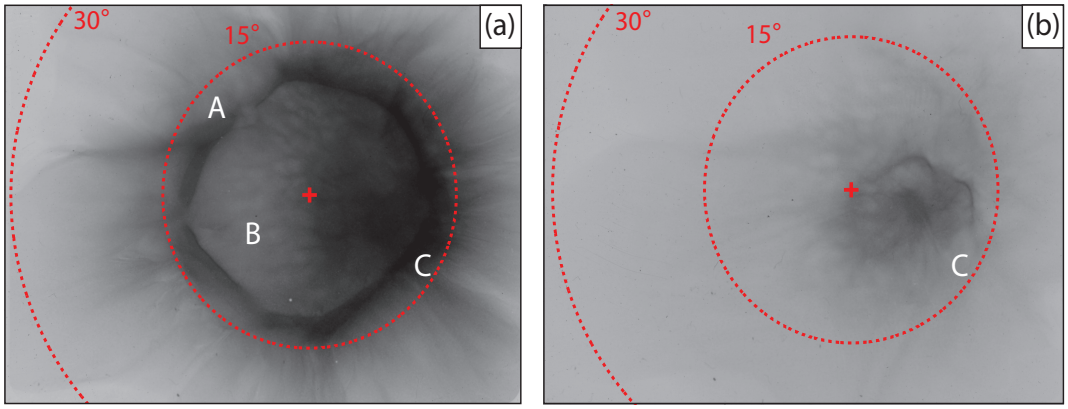

Figure 4.6: RCF images from a relativistically transparent 10 nm Al target. Spatial intensity profile images for proton energies (a) 5.3 MeV and (b) 11.6 MeV. The red cross marks the direction of the laser axis and the dashed rings mark the angular ranges of 15° and 30° respectively.

Figure 4.6 shows a typical proton spatial intensity profile, at two sampled energies, for a target undergoing RIT. At lower energies, as seen in (a), the proton beam is dominated by feature **A**, a ring having a half angle divergence of ∼12°. Similarly, this feature is observed for all targets where RIT is present and has been reported in previous experiments in the RIT regime [114, 150]. In the same RCF layer, there is evidence of bubble-like features (feature **B**), although not particularly pronounced, consistent with the Rayleigh-Taylor instability of radiation pressure accelerated thin foil targets and subsequent proton beams as reported in reference [65]. Within the ring there is also a localised enhancement in the proton flux, though due to the integrated nature of the diagnostic it is not certain if this is a feature of the ring itself.

At higher sampled proton energies however, the profile no longer displays the annular structure witnessed at lower proton energies, but a region of enhanced proton density, feature **C**, within the vicinity of the ring, as can be seen in figure 4.6(b). When this angular region is compared between the two energy layers, it is clear that this corresponds to the feature within the ring mentioned in the discussion of figure 4.6(a) above. From this we can see that there are processes

leading to multiple populations of protons with different spatial characteristics overlapping. In order that we can examine individually the different populations it is necessary that we are able to distinguish each from the others.

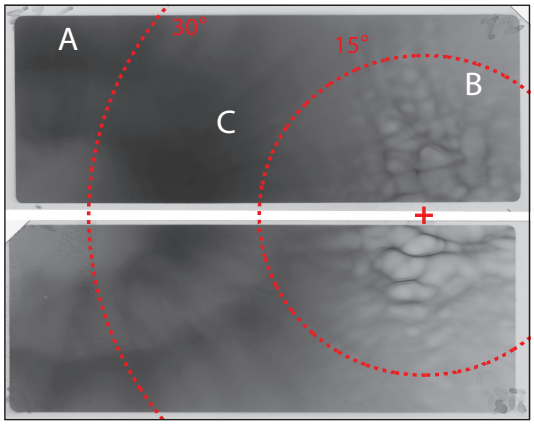

Figure 4.7: Proton beam spatial profile from RCF from an $L = 10$ nm Al target, irradiated by a dual pulse with $I_{RE} = 0.2$. The beam onto the RCF shows separation of three distinct components labelled A, ring feature, B, laser directed bubble structured beam, and C, an off-axis enhanced beam. The red cross marks the direction of the laser axis and the dashed rings mark the angular ranges of 15° and 30° respectively.

By angling the target, as can be seen in figure 4.7, multiple beam components are separated spatially in the projection downstream on the RCF stack. The red cross indicates the laser propagation axis, around which a bubble-like beam, labelled **B**, is centred. The dashed red circles mark radii corresponding to 15° and 30° respectively. The 30° radial line, taken along the middle of the stack, corresponds to the target normal direction in the horizontal plane, around which the annular feature labelled **A** is centred.

Interestingly however, a third feature labelled **C**, in the angular region 15-25° is measured and shows a region of localised enhancement in the proton beam and also the highest proton energies of the three components present. The following sections will take a more detailed look at each of these features.

4.2.1 Laser-directed beam (B)

The first beam to consider is the bubble structured component centred around the laser direction. Previous experiments using the Vulcan petawatt laser [65] have demonstrated a Rayleigh-Taylor like instability arising from the radiation

pressure acceleration of ultra-thin targets. In that work, the target was diamond-like carbon (DLC) of nanometer thickness, where the bulk target composition consisted of carbon and hydrogen. It was found that as the target thickness was reduced, the instability started to dominate, with 5 nm targets showing the highest degree of instability growth.

As we have seen in figure 4.6 (a), a small degree of bubble-like structure is measured in 10 nm Al targets under single pulse irradiance, at low proton energies, indicating the presence of an RPA component of the proton beam.

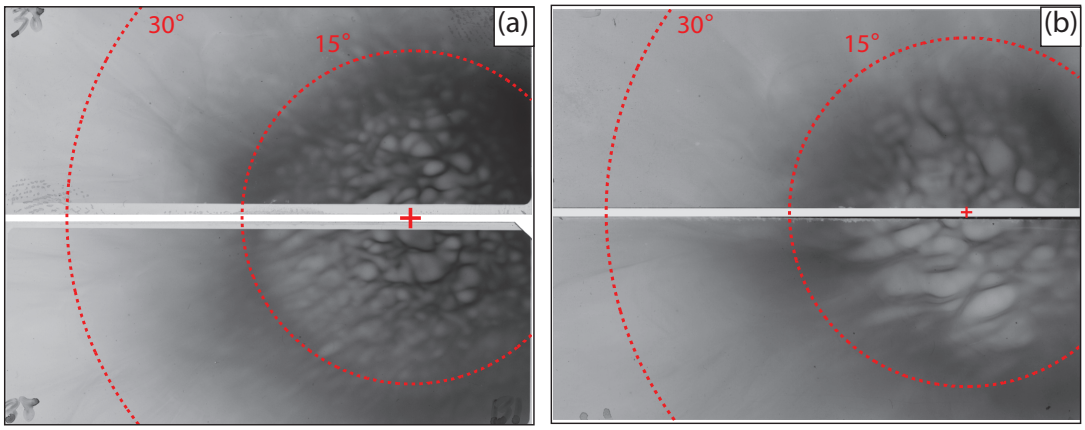

Figure 4.8: Measured spatial-intensity profile of the proton beam from a 10 nm Al target, in the energy range of 7 MeV for (a) $I_{RE} = 0.05\ I_L$ and (b) $I_{RE} = 0.1\ I_L$ at normal laser incidence. The red cross marks the direction of the laser axis and the dashed rings mark the angular ranges of 15° and 30° respectively.

Under the same nominal conditions, by adding a small pre-pulse, changing the intensity gradient of the rising edge of the main pulse, the measured bubble features become much more pronounced and the maximum energy of the component as measured on the RCF increases. Figure 4.8 shows a sample proton profile at an energy of 7 MeV, where an annular feature is observed. Superimposed on this are much more pronounced bubble-like features.

In the transition from single pulse to dual pulse, the rising edge of the main pulse is modified such that I_{RE} increases. This enables pre-expansion of the target prior to the main pulse interaction, setting up a density gradient. By modifying the rising edge sufficiently, near critical density plasmas can be achieved and to some extent controlled prior to the peak of the laser pulse arrival.

By introducing a density gradient, and reducing the target density there are a

number of potential explanations for the measured growth of spatial instabilities attributed to the RPA mode. Reduction of the target density could signify a transition to a regime of efficient hole-boring acceleration, which would agree with the experimental observation of the increasing maximum energy.

The RT instability growth rate is sensitive to the density of the two "fluids", in this case the laser photons and the target electrons. It is clear that by increasing I_{RE} the size of the bubbles measured increases in size and become much stronger. The energy of this laser-directed component is also shown to increase with the same parameter.

It is also seen that as the bubbles become more pronounced, they become less round and develop a strong ellipticity. The degree of ellipticity is largest closest to the laser axis and reduces moving radially outwards. Interestingly, the major axis of the ellipse is aligned with the axis of polarisation of the laser pulse as can be seen clearly in figure 4.8 (b) and 4.7. Both of these observations suggest that there is pondermotive expulsion of the electrons during the transparency phase and has been investigated numerically in reference [151].

The bubbles are only observed in the interaction with the 10 nm Al targets, although weak bubble-like structures have also been seen in the interaction with 40 nm Al target foils with large values of I_{RE}. Though typically very weakly seen in the RCF, they are observed from the burn patterns on the protective layer of the RCF stack indicating that their energy is below the lowest proton energies sampled by the stack.

The increased areal density of the 40 nm target means that the efficiency of the RPA phase for the same range of I_{RE} and pulse parameters, is much less than for the 10 nm, and instability growth is reduced.

The highly structured profile of the laser-directed component of the beam and the small solid angle sampled by the TP spectrometer ($\sim$nSr) mean that beam flux modulations vary shot to shot, making comparison of ion spectra between shots problematic.

4.2.2 Ring profile (A)

The rings observed in the proton profiles show in figures 4.6 and 4.7, labelled **A**, are present for all targets in which RIT occurs. The directionality of the rings, centred around the target normal axis, indicates that it is a transparency-induced effect on the initial TNSA expansion.

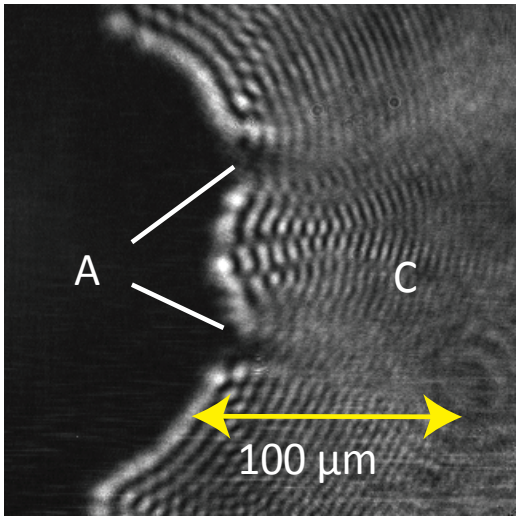

Figure 4.9: Transverse optical probe measurement of the rear surface expanding plasma at $t = 120$ps after the arrival of the main pulse for a 40nm AL target and $I_{RE} = 0.04\ I_L$.

Transverse optical probing of the interaction after the interaction shows plasma expansion that also takes the form of an annular structure. Figure 4.9 shows characteristics of the expanding plasma, 120 ps after the arrival of the main pulse consistent with features observed in the proton profiles measured down-stream. At this timing of the optical probe, the expanding light ion populations have left the interaction region and the image shows the expansion of the bulk target ions after the main interaction. Feature **A** corresponds to the ring-like expansion, and **C** shows evidence of a possible channel consistent with experimental observation from the proton profile measurements.

Previous work, [114, 150], has attributed the ring-like formation of the proton beam to buffering of the rear of the TNSA proton expansion by the heavier, lower charge-to-mass, transparency-enhanced ions. Ring formation of the proton beam occurs most prominently at lower proton energies sampled in the stack. The spatial separation of the expanding protons means that the slower protons are

closer to the heavy ions and will be modulated foremost by the boosted heavy ions. This is supported by the observation of the rings in the lower energy sampled profiles of the beam.

As the ring features are a perturbation of the target normal expanding ions, it is expected that they will be angularly centred around this axis. By spatial separation we have shown this to be the case. Enhancement of the heavy ion population in the transparency phase is mediated by the volumetric heating of the target electrons by the laser field and subsequent energy transfer by the mechanisms discussed in chapter 5.

Although in the RIT regime, electrons at the rear of the target are ponder-motively expelled into a ring, it is observed to be centred around the laser axis. This indicates that the ring profile seen in the proton beam is not a product of the expelled electrons. The annular profile in the proton beam is seen for both the 10 and the 40 nm Al target interactions indicating RIT plays a significant role in both.

4.2.3 Off-axis channel enhanced component (C)

When the beam components are spatially separated, a region of enhanced proton density and maximum energy is observed near the edge of the ring structure, closest to laser axis, at an angle of 15-25° from the laser axis. This feature is most prominently observed with 40 nm aluminium foils, although enhancements to a lesser degree are observed in 10 nm targets also. An example proton beam spatial-intensity profile is shown in figure 4.10, and exhibits both the ring component around target normal axis labelled **A** as well as an off-axis enhancement **C**.

The position of the enhancement, **C**, is observed to vary shot-to-shot within an angular range of ∼10°. On shots for which it overlaps with a localised region of the ring, it gives an arc shaped population of enhanced proton density. When the enhanced region is not spatially overlapped with the expanding ring, the beam takes an approximately circular form as shown in figure 4.10. In shots with 40 nm Al, the off-axis enhanced region is consistently the highest energy component of the overall proton beam, as observed throughout the entirety of the RCF stack.

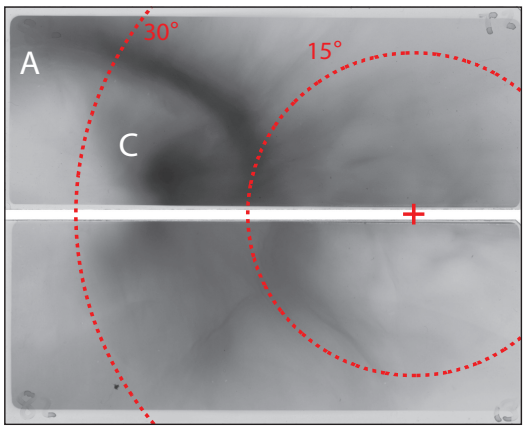

Figure 4.10: Proton spatial-intensity profiles of 40 nm Al targets in the energy range of 5 MeV for $I_{RE} = 0.1 I_L$ for normal laser incidence. Label **A** shows the ring profile and **C** is a localised enhancement off axis

The shot-to-shot variability in the direction of the component C is attributed to the asymmetry in the local density around the laser propagation axis. The asymmetry in the expanding plasma leads to a susceptibility for the propagating laser pulse to refract in the plasma. This is illustrated in more detail in the discussion of the PIC simulations later in this chapter.

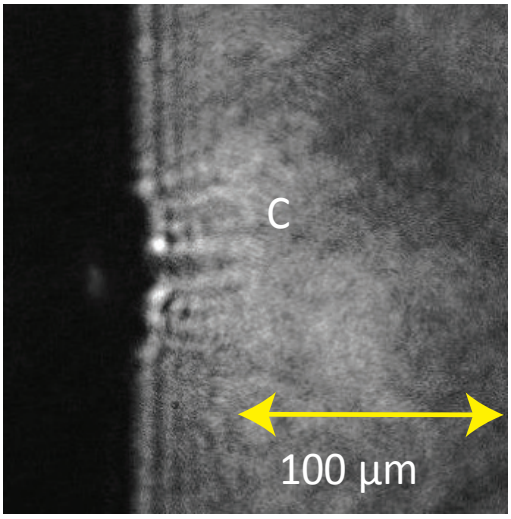

Figure 4.11: Transverse optical probe measurement of the rear surface expanding plasma at $t = 10$ps after the arrival of the main pulse for a 40nm AL target and $I_{RE} = 0.1\ I_L$.

The variation in the position of feature C makes it difficult to reproducibly sample the ion spectrum with a fixed TP spectrometer at various angular intervals. Instead representative proton spectra taken from RCF stacks are compared

with TP spectra obtained at the closest angular position of 8°, corresponding to the edge of feature **C**. The RCF gives a more accurate measure of the proton maximum energy compared to the TP, though in comparison any spectral measurements are coarse.

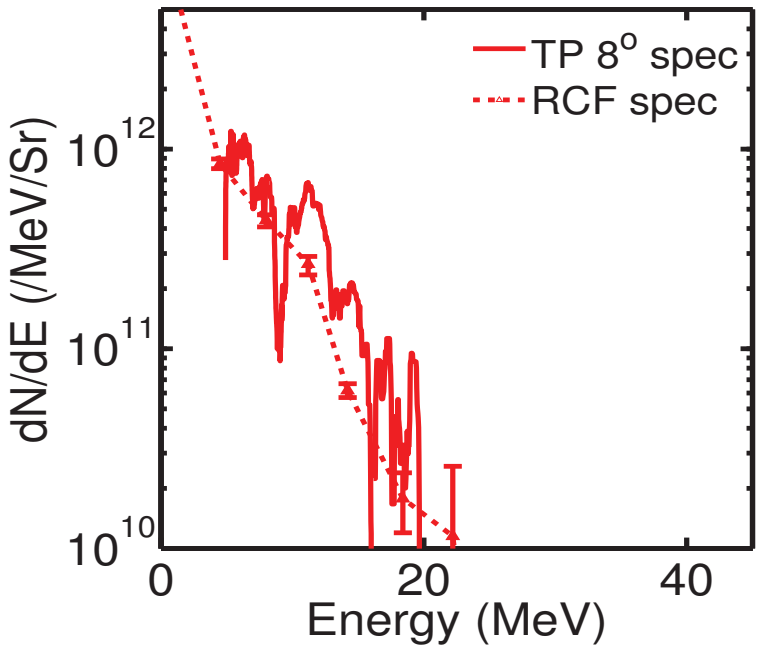

Figure 4.12: Comparison between proton spectra obtained from TP spectrometer (Red - solid) and RCF (dashed red) in the angular region of the channel enhanced proton beam component, for $I_{RE} = 0.04 I_L$

Optical probing of the expanding plasma at $t = 10$ ps after the main pulse shows evidence of a dense plasma channel formed, labelled **C**, at the rear of the target and expanding out into vacuum. A comparison with the later optical probe measurement in figure 4.9 shows that this process is independent of the ring-like expansion and occurs on a much faster time scale. Channel formation and propagation of the laser pulse through tenuous plasmas have been studied in references [47, 51], which have shown enhanced coupling of laser energy into the plasma over an extended length in this regime.

After the target has become relativistically transparent, the laser pulse self focusses and electrons are pondermotively expelled from the regions of high intensity forming a plasma channel. Electrons that are expelled along the propagation axis of the laser set-up a strong current generating an azimuthal magnetic field that can maintain the channel over an extended distance. Within the channel,

the laser pulse can be absorbed in the plasma over an extended length resulting in an enhancement to the electron and proton energies, effectively generating a plasma jet.

Variation of the rising edge, by adjusting I_{RE}, enables the rear surface plasma expansion to be controlled such that optimal channel formation and absorption of the propagating laser pulse post-transparency can be achieved.

For the case of $I_{RE} = 0.04\ I_L$ and $L = 40$ nm, the spatial profile shows an arc-like enhancement on the edge of the ring that extends to a maximum energy of 25 MeV. The energy spectrum of the protons, as obtained from the TP spectrometer and from RCF stack detector, show a relatively thermal distribution with some peaked modulation toward higher energies.

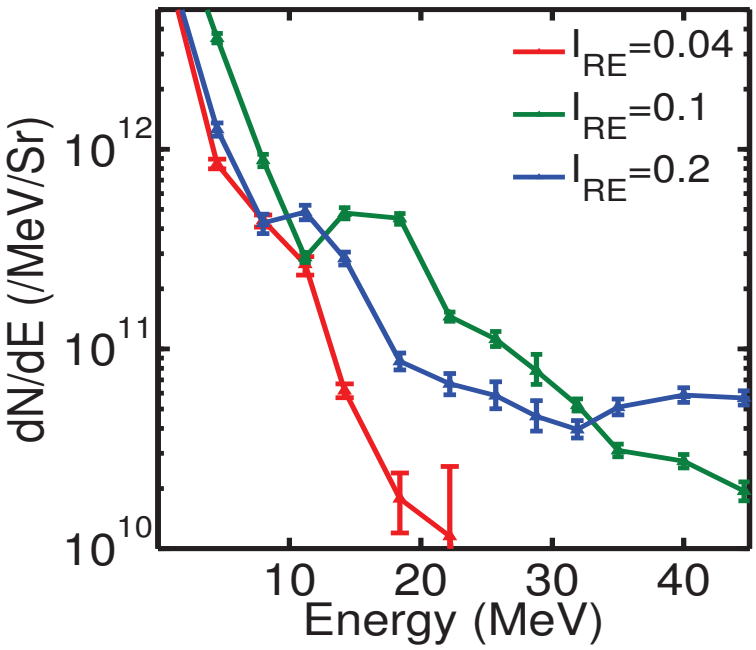

Figure 4.13: Proton spectra extracted from the RCF in the region of feature C beam component for values of $I_{RE} = 0.04 - 0.2 I_L$.

It is worth noting that the RCF shows a higher cut-off energy and this is due to the fact the TP at 8° is not sampling the beam precisely in the region of feature C.

Figure 4.13 shows the proton spectra measured in the region of the enhancement for three different rising edge profiles including the reference $I_{RE} = 0.04 I_L$ case from before. This shows an extension of the spectrum to higher proton

energies as I_{RE} is increased. An overall enhancement in the ion energies in the angular region situated between target normal and the laser axis and corresponding to feature **C**, is observed, with the maximum energy doubling over the range $I_{RE} = 0.04 \rightarrow 0.2 I_L$.

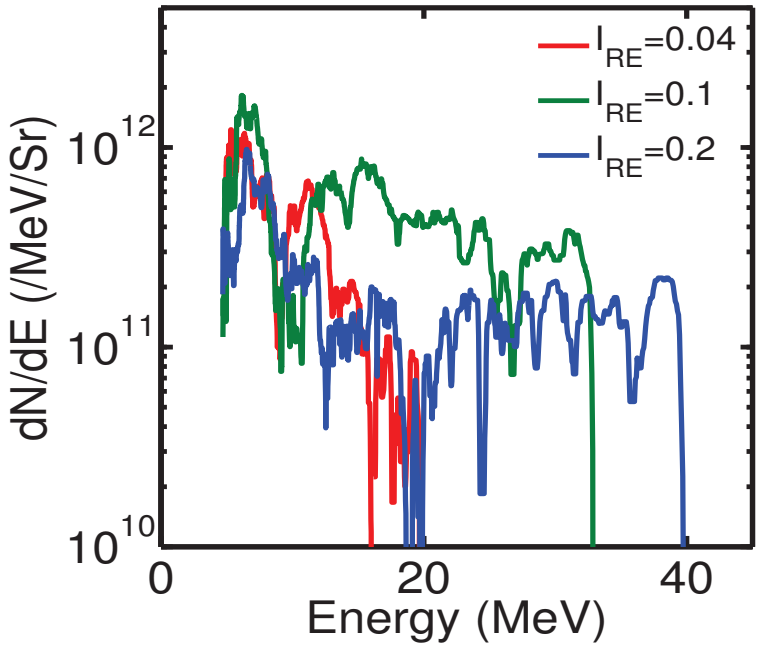

Figure 4.14: Proton spectra extracted from the off-axis (8°) TP spectrometer for values of $I_{RE} = 0.04 - 0.2 I_L$.

An energy spectrum can be extracted from the TP positioned at 8° which gives greater energy resolution. The measurements using the TP spectrometer confirm the maximum proton energy enhancement with increasing I_{RE}. It also shows that as I_{RE} is increased, the proton spectrum departs from that of a thermal-like distribution expected of TNSA, to one with multiple peaked features as well as a plateau in the high energy region.

This trend is observed in TP measurements of C^{6+} ions also, with maximum energies of 15 MeV/u achieved. The corresponding C^{6+} spectra from the same TP spectrometers are shown below in figure 4.15.

There are no corresponding beam spatial profile measurements for the C^{6+} ions as this is not possible with the RCF stack (not possible to separate the proton and carbon dose contributions). The carbon beam profile characteristics are therefore unknown.

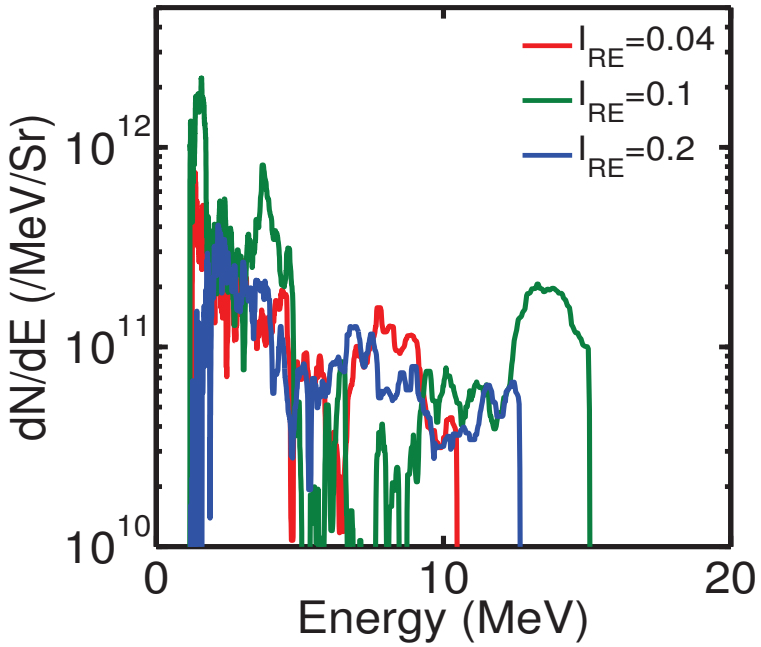

Figure 4.15: Carbon spectra (C^{6+}) from the 8 degree off-axis TP spectrometer for values of $I_{RE} = 0.04 - 0.2I_L$

4.3 PIC simulations

To investigate the underlying physics, 2D and 3D PIC simulations were performed using EPOCH, a fully relativistic PIC code [146].

For the 2D simulations, a simulation box of 175 μm$\times$ 65 μm, consisting of 26000 $\times$ 3840 mesh cells was used. Targets of L=40 nm thickness at an angle of 30°, with respect to the laser propagation axis, were used in the simulations. The target consisted of a 40 nm layer of Al^{11+} with an ion density equal to $60n_{crit}$, where n_{crit} is the critical density as described in chapter 2. On each surface of the target, an 8 nm thick contamination layer consisting of fully ionised carbon and hydrogen. The layers had an ion density of 60 n_c and 20 n_c for C^{6+} and H^+ respectively. The neutralising electron population was initialised with a temperature of 10 keV.

The laser pulse simulated had a Gaussian temporal envelope with a FWHM of 0.5 ps and a focussed Gaussian intensity spatial profile with a FWHM of 6 μm. The peak intensity of the pulse set to I_L=2×10^{20} Wcm^{-2} to match the experimental conditions.

The rising edge of the main pulse was varied by the addition of a second

laser pulse of the same duration but variable peak intensity, 1 ps prior to the main pulse. The intensity of the pre-pulse, I_{RE}, was varied up to $0.5I_L$, with the intensity of the main pulse being reduced correspondingly such that the total energy is conserved, as in the experiment.

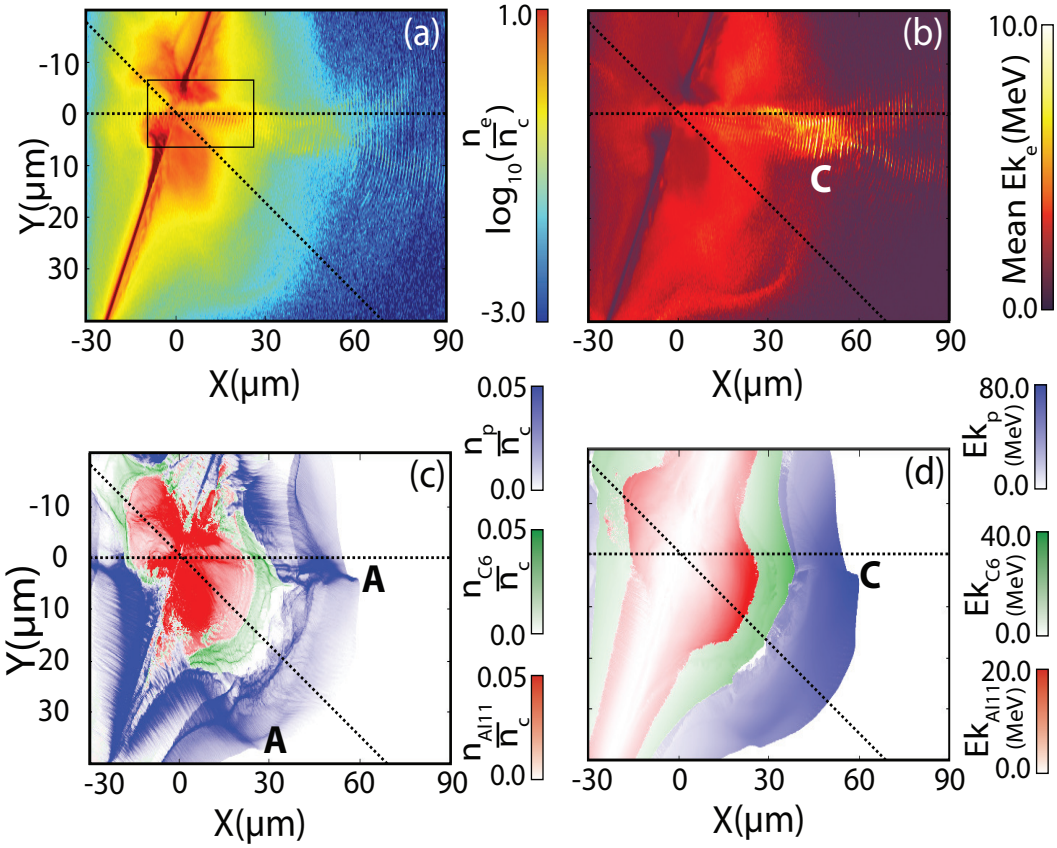

Figure 4.16: Top row: 2D PIC results showing (a) electron density and magnetic field (inset), (b) mean electron energy, (c) ion density (protons - blue; C6+ - green; Al11+ - red) and (d) mean ion energy, all for $I_{RE} = 0$ at an example time of 1 ps. The laser pulse is incident from the left along the Y=0 axis. The dotted lines mark the laser and target normal axes.

In the example result shown in figure 4.16, a single Gaussian pulse is simulated. It is found that at early times in the interaction, front surface electron heating drives sheath expansion. The difference in charge to mass of the different species accelerated due to the sheath field results in a layered expansion with the protons expanding ahead due to their higher velocity. Later in time, close to the peak of the pulse, RIT occurs and drives additional electron heating over the target volume that the remainder of the pulse travels through, as shown in figure 4.16**(c)**. The transparency enhanced heavy ions, carbon and aluminium, having gained

energy from the volumetrically heated electron, rapidly expand at a greater rate than the initial TNSA phase, and push on the rear of the expanding proton layer. This results in a modulation to the spatial profile of the lower energy protons, as shown in 4.16(c) and labelled **A**.

The 2D simulations show the formation of a ring-like structure in the expanding proton distribution that arises from the rapid expansion of the heavy ions deforming the rear of the proton layer. This is labelled as feature **A** in figures 4.16 and 4.18. The simulations do not show a clear indication of a dominant RPA component present in the simulations of L=40 nm, in particular the presence of transverse surface instabilities used to identify it experimentally, were not clearly observed.

The simulations also show a feature, labelled **C**, close to the laser axis. This feature contains the highest proton energies and comparison with figure 4.16(b), shows that in this region there is an enhancement in electron energy. Comparison with the 2D electron density map in figure 4.16(a) shows that a channel is formed in the expanding plasma, through which the laser pulse propagates. In a localised region the electron energies are enhanced due to the laser pulse, resulting in a fast electron jet and a boost to all ion energies propagating close to, although not directly along, the laser axis. This is labelled as feature **C**. Figure 4.17 shows the corresponding magnetic field in the B_Z direction that acts to sustain the channel and the additional electron heating drives the accelerating electric field into the expanding ion layers boosting their energies over the length of the plasma.

In this way, during the RIT phase, the laser pondermotively expels electrons on axis and relativistically channels through the expanded near critical density plasma. In the channel, the laser directly accelerates any remaining electrons. The strong current of electrons sets up a self-generated azimuthal field that maintains the channel over an extended distance beyond the rear of the target. The channel extends out into the expanding ion layers with the electrons heated in the presence of the propagating pulse transferring energy to the ion population. The longitudinal extent of the resulting plasma jet is governed by the ability to draw a return current from the background plasma to neutralise the fast electron

beam. Thus the jet extends to the region of the expanded plasma and thereafter expands in radius and is broken up.

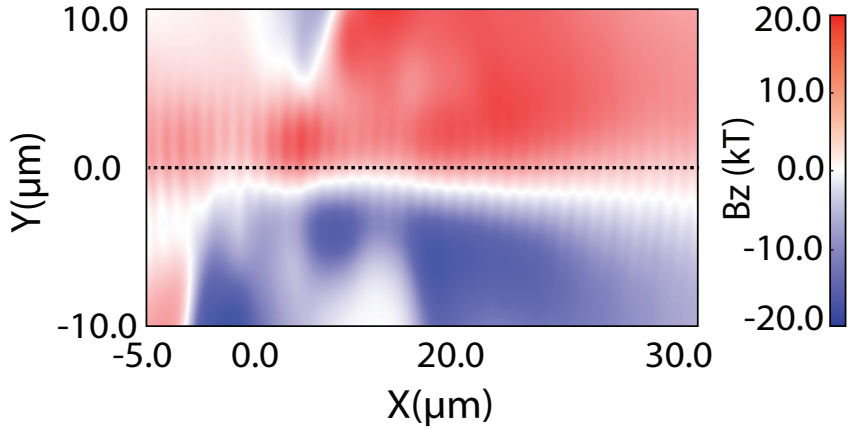

Figure 4.17: 2D PIC simulation result showing the azimuthal (B_Z) magnetic field that maintains the channel at the rear of the target.

The proton distribution observed in figure 4.16 is in good qualitative agreement with experimental results that exhibit a ring like profile centred around the target normal, labelled **A**. Although the electrons around the laser direction take an annular form also, due to the radial pondermotive expulsion from the laser field, this does not appear to be responsible for the highest energy, feature **C**, and the rings observed in the proton beam appear to be produced by the RIT boosted acceleration of the heavier ions into the proton layer.

The magnetic field and channelling is similar to that observed in relativistic laser pulse propagation in other types of near-critical density plasmas [47, 51, 56]. The initial channel propagation is along the laser-direction as one would expect, but tens of microns from the rear surface, the channel steers off to one side by ∼10-15°. At this point the jet cannot draw a return current longitudinally and steers to the side due to the asymmetry in the plasma density from the angle of the target.

Within the channel, the propagating laser directly accelerates the electrons resulting in higher electron energies than in the background plasma as shown in the 2D electron energy map in figure 4.16(b). In the vicinity of this enhanced electron energy, at the edge of the expanding ring, additional energy is coupled to the protons and heavy ions and results in the highest energy protons being

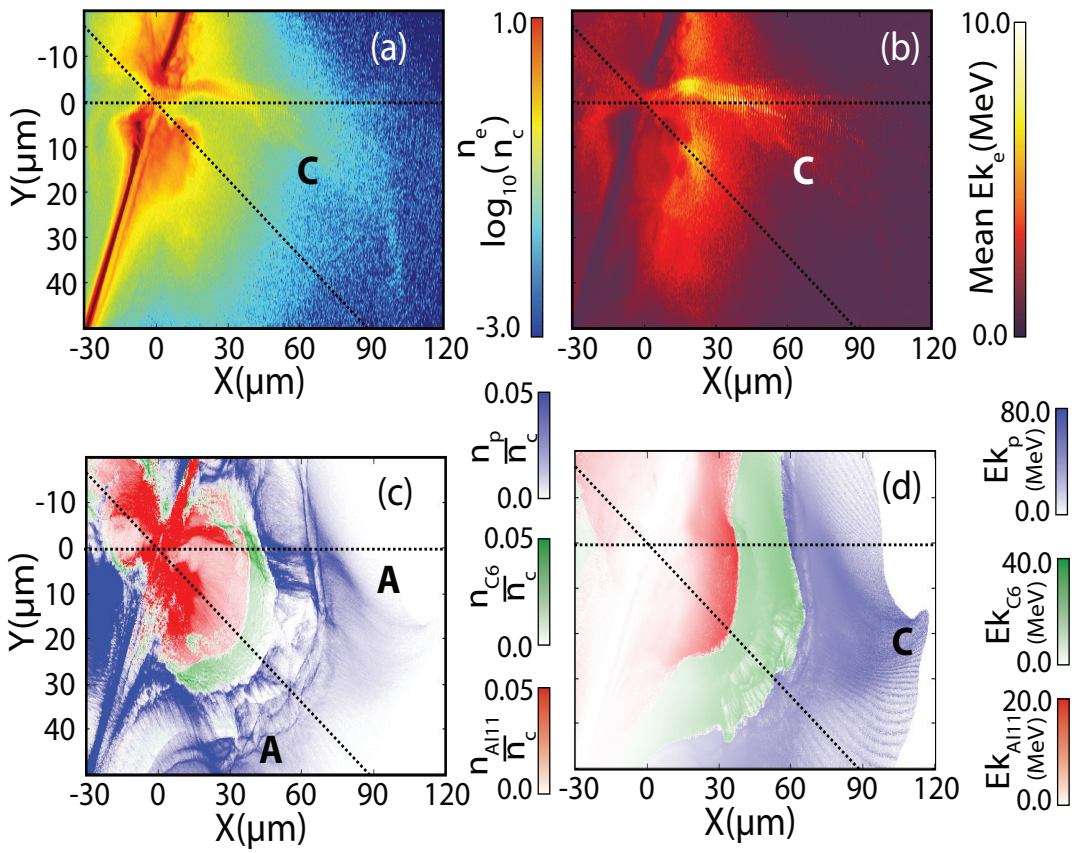

Figure 4.18: Top row: 2D PIC results showing (a) electron density and magnetic field (inset), (b) mean electron energy, (c) ion density (protons - blue; C^{6+} - green; Al^{11+} - red) and (d) mean ion energy, all for $I_{RE} = 0.2$ at an example time of 1 ps. The laser pulse is incident from the left along the Y=0 axis. The dotted lines mark the laser and target normal axes.

produced in this angular region. Expansion and divergence of the channel and electron beam at larger distances from the rear of the target enable the electrons to provide to a lesser degree a boost in ion energies over a wider angular range.

A double pulse interaction is simulated under the same conditions except with a pre-pulse with intensity of $I_{RE} = 0.2I_L$, and the results are shown in figure 4.18. The modification of the rising edge intensity profile of the laser pulse by the addition of a pre-pulse results in pre-expansion of the target to near-critical density, prior to the main pulse arrival. The pre-expansion of the target enables the channel formation to occur over a much greater length, reaching to the front of the proton layer, as shown in figure 4.18(b)-(d). Controlled pre-expansion of the target by variation of the rising edge intensity profile enables channel formation to occur over an extended distance and subsequent additional energy transfer

from the laser pulse to electrons, ultimately resulting in enhancement in proton energies.

To verify that the channel and jet are not simply a product of the 2D simulation geometry, 3D simulations were performed using EPOCH. The 3D simulations are much more computationally demanding, which constrained the size of the simulation box and resolution that could be simulated with available computation resources. The simulation box used was 60 μm $\times$ 20 μm $\times$ 20μm with a mesh cell density of 3000 $\times$ 360 $\times$ 360. To compensate for the reduction in box size and resolution compared to the 2D simulations, the target consisted of the equivalent of 20 nm Al^{11+} at a peak density of $60n_c$, expanded to a Gaussian profile with a peak density of $5n_c$. The contaminant layers were treated in the same way and expanded to give a peak density of $5n_c$ and $1.67n_c$ for the H^+ and C^{6+} respectively. In the expanded target, the areal density is conserved to equal that of initial solid density. The neutralising electrons were given an initial electron temperature of 10 keV. The target once again is initialised at an angle of 30° with respect to the laser axis. The main laser pulse simulated had a duration of 0.2 ps FWHM and a peak intensity of 2×10^{20} W cm^{-2}, and in the case where a pre-pulse is simulated to modify the main pulse rising edge, the two pulses were separated by 0.5 ps and the total energy between the two pulses conserved. The reduction in temporal duration of the pulses is due to the computational demands of running the 3D simulations.

The 3D simulations shows the formation of a plasma channel and direct acceleration of the electrons by the laser field within it. This can be seen in figure 4.19 which shows the electron kinetic energy at 0.4 ps. It shows a clear coupling of the laser into electrons with the electrons gaining a maximum energy within the region of the channel. In the region close to the rear of the target the electrons are also heated over a wider radius of tens of microns and observed to form an annular density distribution in the plane perpendicular to the laser axis. This is due to the radial pondermotive force. The RIT behaviour observed clearly in the 3D simulation is consistent with theoretical predictions and experimental results as reported in references [1, 109].

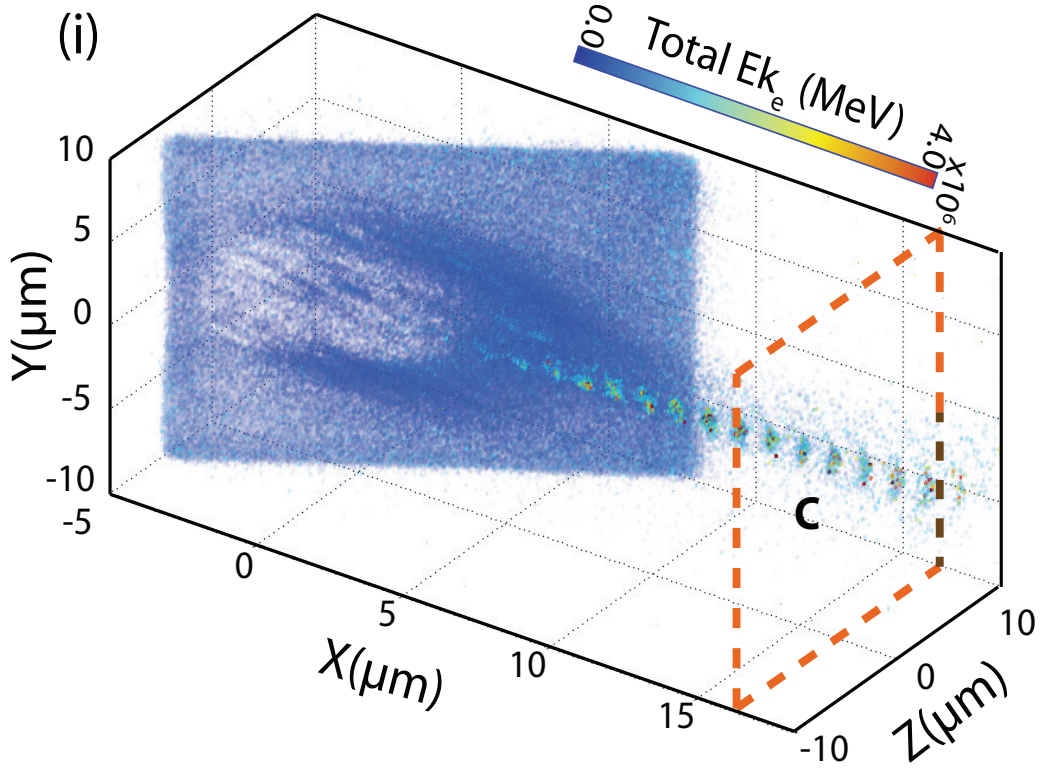

Figure 4.19: 3D PIC results showing an example 3D plot of the total electron energy at sample time of 0.4 ps. Label C corresponds to the electrons which are enhanced by the laser guided within the channel.

By taking a 2D slice in the Y-Z plane of the 3D simulation, shown in figure 4.19, and marked with the dashed red box, at a distance of 16 μm from the point of interaction, it is possible to sample the 2D distribution in the plane of the detector. Figure 4.20 shows the spatial energy distribution of the electrons and shows a clear localised energy enhancement close to the laser axis.

The 2D energy distribution of the protons is also sampled in the same pane and is shown in figure 4.21. The region highlighted as **C** corresponds to the region of enhanced electron energy. It can be seen that this acts to enhance the side of the expanding proton ring that is closest to the laser axis, and that the annular proton expansion is centred off axis.

At this relatively small distance from the target rear the channel is close to the laser axis and overlaps with one side of the proton ring. However at larger distances, as shown in the 2D simulations illustrated in figures 4.16(b) and

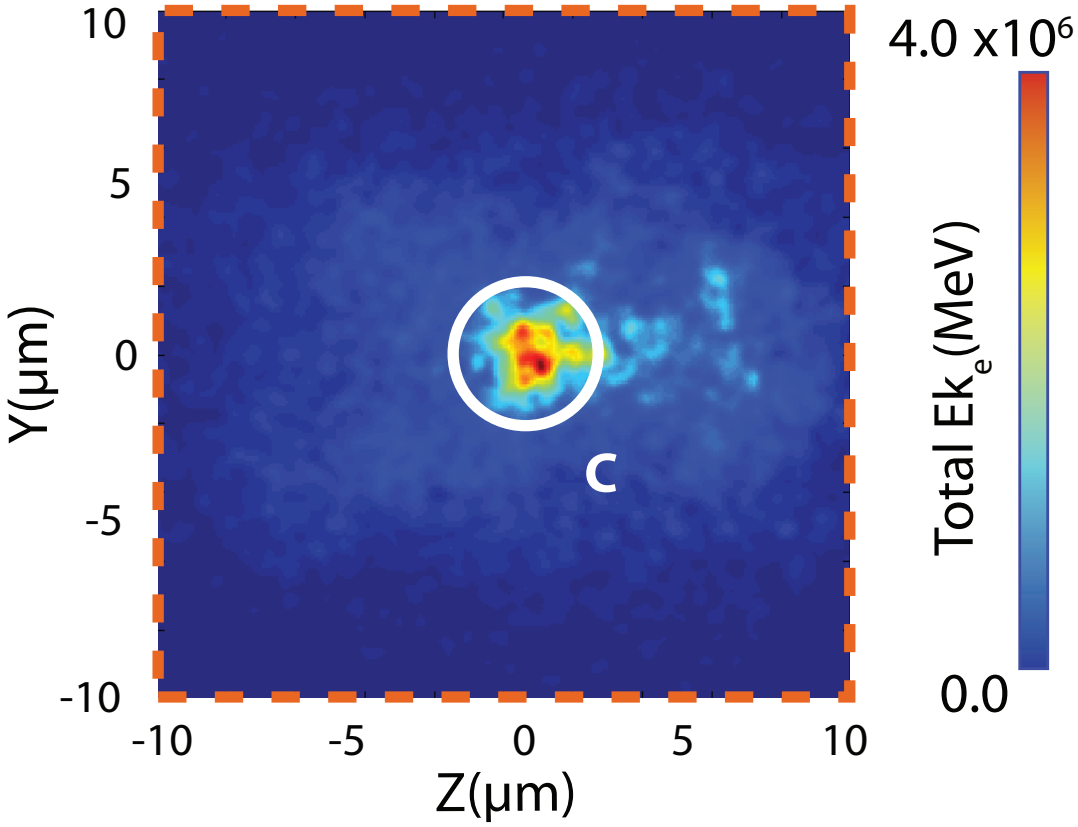

Figure 4.20: Results from 3D PIC simulation showing the total electron energy in a 2D plane taken at 16μm, and marked with the dashed red box in figure 4.19.

4.18(b), the channel steers off axis due to the asymmetry in the expansion.

4.4 Discussion

The experimental results show that there are three distinct components present in the accelerated proton beam in targets undergoing RIT, and these are also observed in 2D and 3D simulations. The highest energy component of the beam is observed at a angle between the laser and target normal axes and labelled feature **C** throughout.

Comparison of the proton spatial measurements shown in section 4.2 with the results from both 2D and 3D simulations of 40 nm targets show that there are multiple acceleration process occurring over the duration of the interaction and that they have unique spatial characteristics that enable them to be distin-

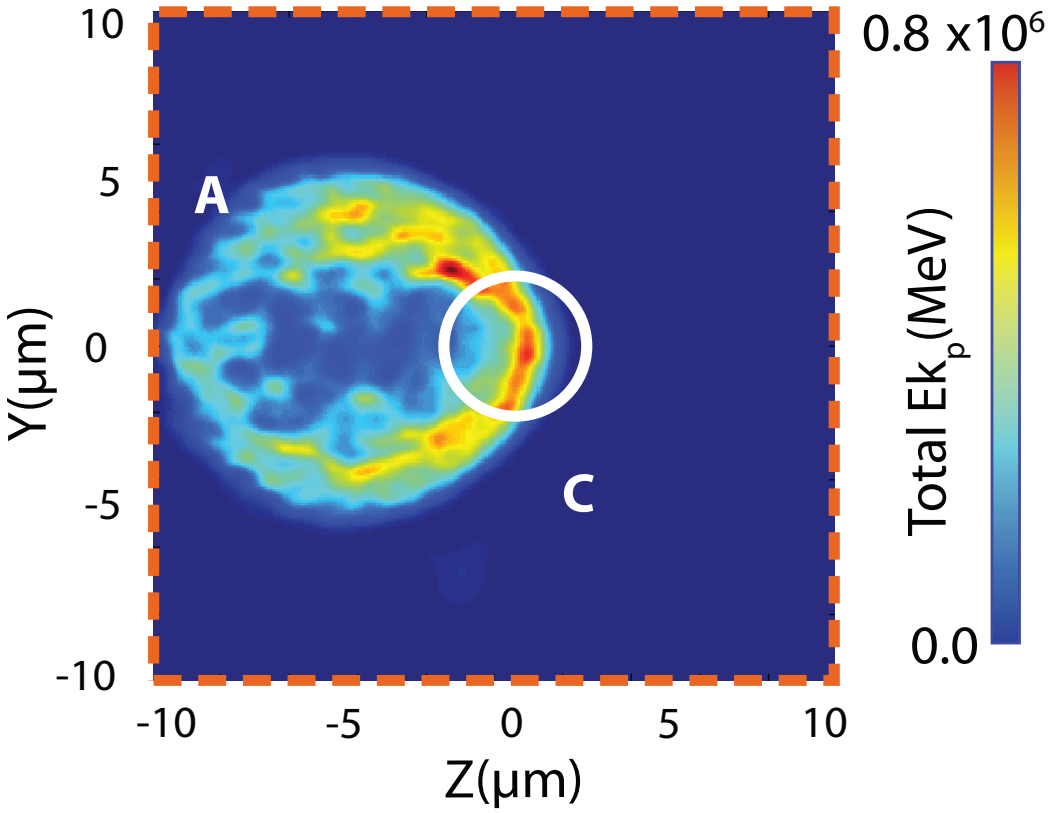

Figure 4.21: Results from 3D PIC simulation showing the total proton energy in a 2D plane at 16μm, and marked with the dashed red box in figure 4.19. The feature labelled **A** corresponds to the annular profile component of the proton beam expanding off axis from the laser propagation direction. Feature **C** is the region of the expanding beam enhanced from the energetic electrons accelerated in the plasma channel

guished. Ring profiles in the proton beam centred around target normal direction experimentally are also observed to expand along the target normal axis.

The 2D density and energy plots of the ions sampled at a time after transparency and illustrated in figure 4.18(c) and (d) show that regions of localised high density labelled **A**, in the form of a ring centred around the target normal axis (black dashed line).

It can be seen that the rear of the proton layer has been deformed and that the ions behind have gained significant energy causing the back of the proton layer to be pushed by the rapidly expanding heavy ions. This results in localised regions of high proton density measured downstream as a ring profile.

A comparison between the 2D proton profile sampled downstream from the 3D simulation with experimental measurements is provided in figure 4.22. The profile

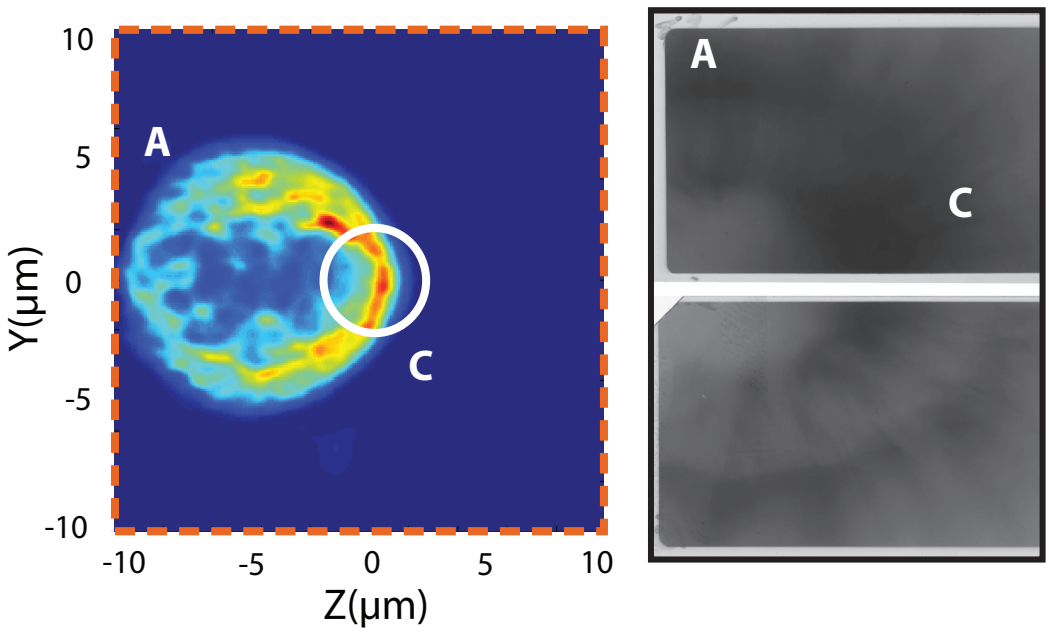

Figure 4.22: Comparison of proton profiles from (a) 3D simulations and (b) sampled experimentally from RCF. **A** corresponds to the ring profile in the beam and **C** the enhancement from plasma channel off axis

from the 3D simulation is in good agreement with that measured experimentally. The expanding ring profile is centred off axis from the laser direction, with one side of the ring enhanced due to the presence of electrons further accelerated by the laser propagation within the channel.

When looking at the ion energy plots in figures 4.18(d) , it can be seen that the highest energy protons are directed at an angle between target normal and laser axes labelled as **C**. In this region, comparison with the electron kinetic energy plots in figures 4.18 (a) show that the electrons have gained considerable energy localised within the channel in the multi-MeV range.

The measured maximum proton energy of the feature **C** increases with I_{RE} experimentally, from 25.7 MeV to 50 MeV, over the range $I_{RE} = 0.04I_L$ to $I_{RE} = 0.2I_L$.

The simulations show a similar trend in the increase in maximum energy, both in the 2D and 3D cases.

The maximum proton energies obtained experimentally from the RCF stack in the vicinity of the enhancement are plotted along with maximum energies obtained from simulation, for both protons and electrons in figure 4.23. The maxi-

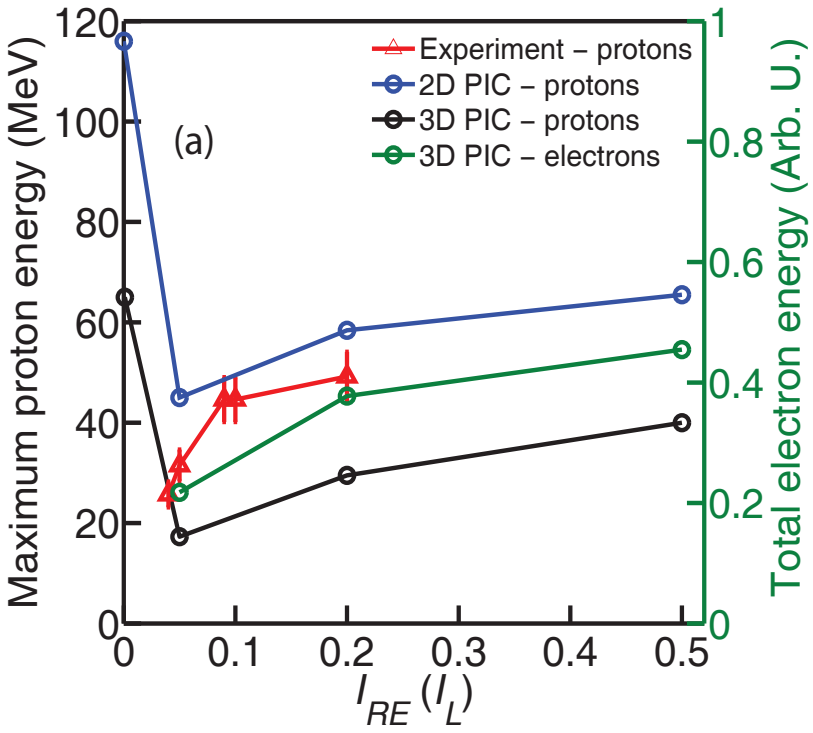

Figure 4.23: Comparison of the maximum proton energy in the experiment and in the 2D and 3D simulations, and total electron energy in the region of the channel in 3D simulations, as a function of I_{RE}.

mum proton energies in the simulations are in the off-axis region of enhancement and confirms that this is highest energy component of the expanding ion beam. This can also been seen in the 2D proton kinetic energy profiles in figures 4.16(d) and 4.18(d).

Compared to the experimental results, the maximum energies predicted are higher in the 2D and lower in the 3D simulations, but these absolute values are sensitive to the laser pulse duration and simulation time, for which both are shorter in the more computationally intensive 3D runs.

With increasing I_{RE}, the expanded near critical density plasma becomes more favourable for extended channel formation and results in higher laser energy coupling to electrons as can be seen in figure 4.23.

The case of $I_{RE} = 0$, an idealised Gaussian pulse with a sharp rising edge, is an exception however. Significantly higher proton energies are predicted under these conditions due to the limited expansion of the ions prior to the onset of RIT. This results in the plasma jet extending over the full dense proton layer, as

shown in figure 4.16(a)-(d). In this example, the proton layer has a spatial extent reaching 60 μm from the rear of the target and the plasma jet extends beyond this.

Experimentally the 'single' pulse scenario generates the least energetic protons, which seems at first to contradict the simulations.

However, this is not the case. Figure 4.1 shows an example contrast measurement made of the combined pre-amplifiers, stretcher and compressor using a third order cross-correlator (Sequoia) with the calculated enhancement due to the plasma mirror, as modelled using measurements of plasma mirror reflectivity [3]. The corresponding plot of the PM enhanced contrast in the pico-second region of the pulse rising edge is shown in figure 4.24. Example on-shot auto-correlation measurements in both single and dual pulse modes are also shown, together with a reference Gaussian pulse of 1ps FWHM.

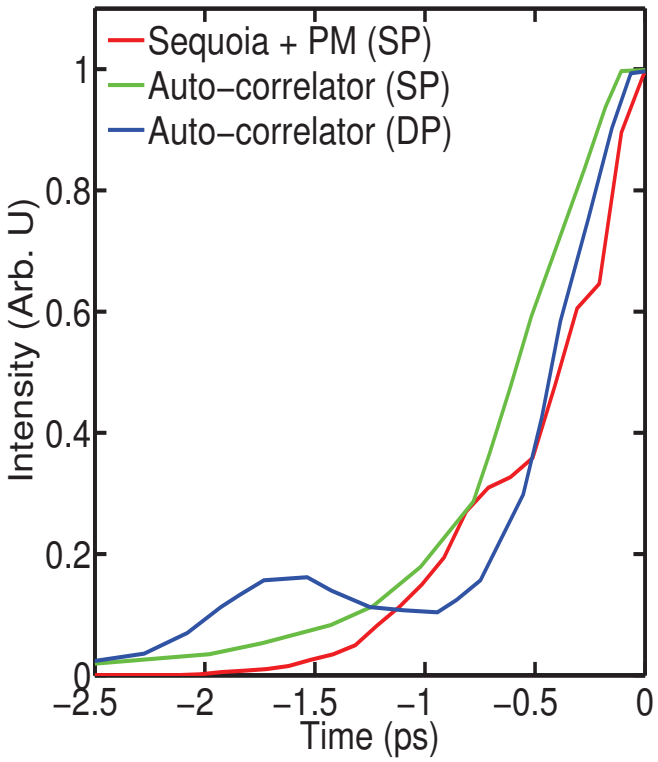

Figure 4.24: Contrast measurement on a linear intensity scale; Red - calculated enhancement to contrast measurement of combined pre-amplifiers and stretcher/compressor as shown in figure 4.1; Green - on-shot autocorrelation measurements of a single pulse; Blue - on-shot autocorrelation measurement of a double pulse ($I_{RE} = 0.2$); Black(dashed) - Gaussian single pulse with 1ps FWHM.

Even with the plasma mirror enhancing the contrast, for a single laser pulse

experimentally, $I_{RE} \sim 0.04 I_L$ as seen in figure 4.24. Thus the perfect Gaussian pulse is not experimentally achieved in this study using the Vulcan laser.

Thus experimentally $I_{RE} = 0.04 I_L$, for the nominal single pulse condition, and shows that even with a relatively small inherent I_{RE} of only a few percent of I_L, the proton layer expands significantly before the onset of RIT and the channel is formed predominantly within the lower q/m ion layers.

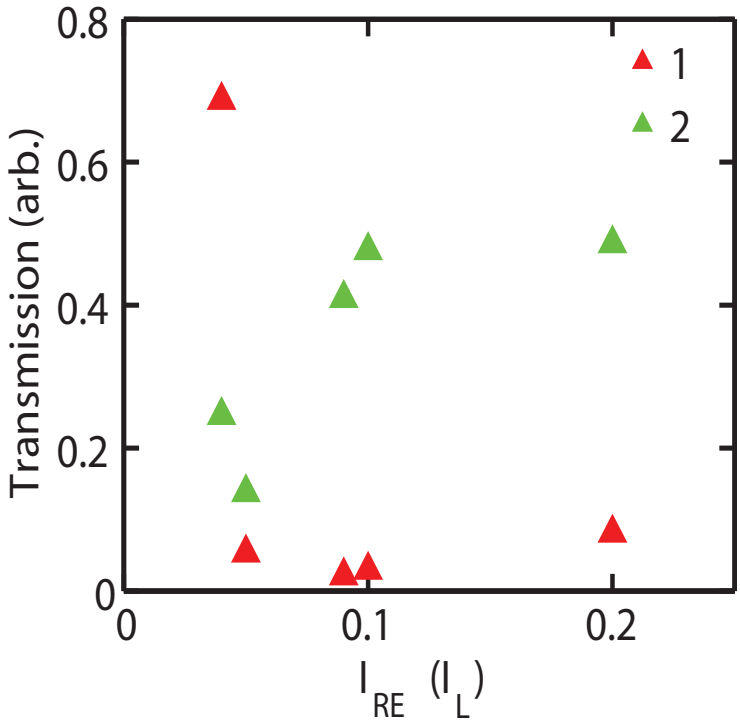

Figure 4.25: Measurement of the transmitted 1ω and 2ω light for 40nm Al targets with increasing I_{RE}.

This work shows that in the event that ideal ultra-high contrast conditions are not achieved on the picosecond rising edge, increasing the value of I_{RE} by the addition of a small pre-pulse acts to pre-expand the target further such that the conditions for the formation of a sustained plasma channel become much more favourable. The transmitted laser pulse is guided within the channel and able to exchange energy over a greater length and out into the TNSA expanded proton layer.

Absorption of the laser pulse within the channel, transferring energy to the electrons, becomes more favourable with increasing I_{RE} as shown in the simula-

tions. Measurement of the transmitted laser light at the fundamental frequency supports this observation. Over the range of I_{RE} tested experimentally, from $I_{RE} = 0.04I_L$ to $I_{RE} = 0.2I_L$, a sharp decrease in transmitted 1ω is observed indicating an increase in absorption. Figure 4.25 shows the transmitted light measured by integration of the signal count imaged on the front of the RCF stack, and normalised to the laser pulse energy.

With increasing I_{RE}, the $2w$ light is measured to increase significantly, though it is unclear if this is transmitted from the front surface or produced in the vicinity of the channel. Previous work by Borghesi *et al*, [51], has shown an increase in backscattered 2ω from laser propagation in channels from near critical density plasmas formed on the target front surface and used this as a diagnostic of the channel formation. Since the second harmonic generation is produced through non-linear processes in the direct interaction of electrons with the oscillating field of the laser it provides an indirect measure of the laser coupling to electrons during in the channel [51] during the RIT phase. The increase in the amount of 2ω could indicate increased absorption in the channel and coupling to electrons and follows a similar trend to the maximum ion energy.

It is seen that the most efficient channel formation and subsequent exchange of energy to the ions is observed in the L=40 nm Al interactions. The presence of a localised enhancement off-axis is also seen to occur for the thinner L=10 nm targets. In L=40 nm interactions, it is clearly seen that the most energetic component of the beam is the off-axis one with the laser axis component being much lower in energy. In the 10 nm targets though, there is increased competition between the off-axis beam and the laser driven component.

Figure 4.26 shows the maximum proton energies, of feature C, from the RCF stacks for a range of values of I_{RE} for both 10 nm and 40 nm targets. The maximum proton energies are observed to increase with I_{RE} for the thinner targets as well, though comparison with the 40 nm scan shows that it is to a much lesser degree. The thinner target is much more sensitive to the rising edge intensity profile. The jet does not form to the same extent due to the significantly reduced density arising from the rapid expansion.

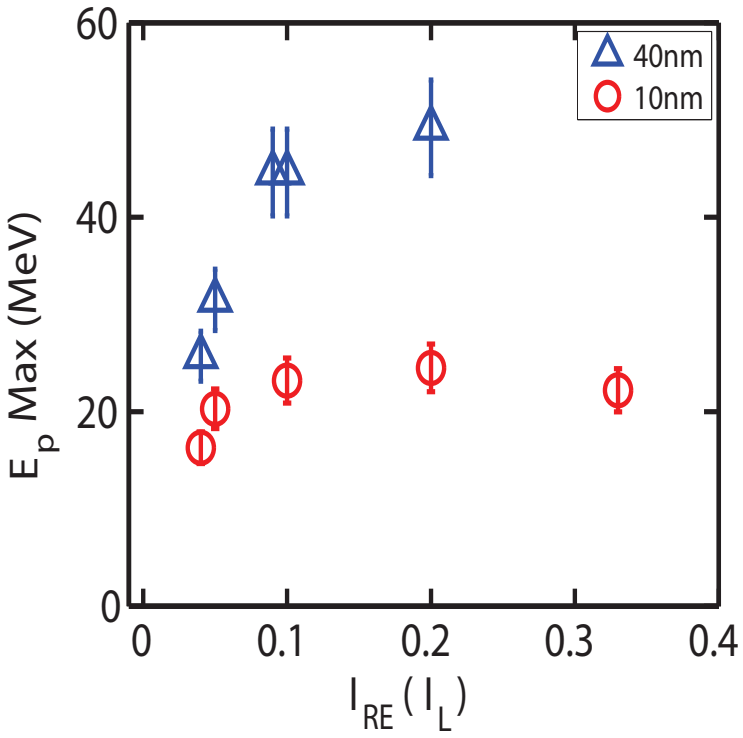

Figure 4.26: Comparison of the maximum proton energies from the RCF stacks of feature C. Proton maximum energies are shown for 10 nm Al foils (red) and 40 nm foils (blue) as a function of I_{RE}

Figure 4.27 shows the temporal evolution of the maximum proton energy as well as the total electron energy from simulations, for both transparent and non-transparent target cases. The transparent case is represented by the solid lines and considers a 40 nm Al target undergoing RIT. Two cases are considered for which RIT does not occur. The first is the 40 nm Al considered above, but at the point of transparency the laser pulse is truncated such that there is no transparency enhancement in the expanding plasma. This is shown by the dotted lines. The second case, represented by the dashed line, considers the full pulse interaction with an 800 nm Al target as a benchmark case, for which there is no transparency, only TNSA.

The 40 nm target expands until RIT occurs at 0.6 ps, at which point the total electron energy rapidly increases. It begins to decrease again as the laser pulse decays and energy is transferred to longitudinal accelerating fields and the ions, from the point of $\sim$ 1 ps. There is a corresponding increase in the proton acceleration, shown by the change in gradient of the maximum proton energy, at

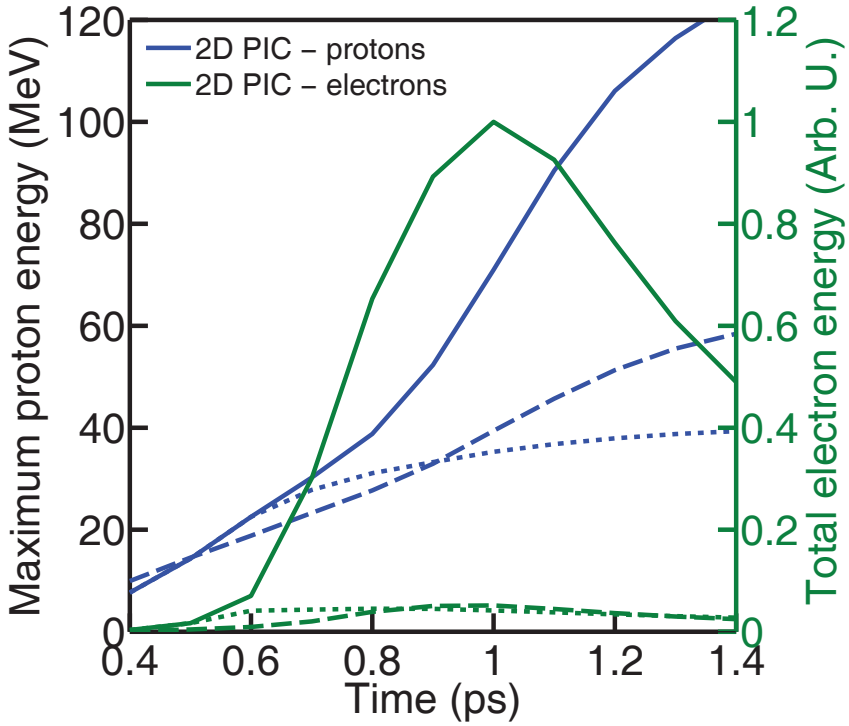

Figure 4.27: Temporal evolution of the maximum proton energy and total electron energy behind the target: Solid - L = 40 nm with RIT; dotted - L = 40 nm with the laser pulse truncated immediately prior to RIT; dashed - L = 800 nm with the full laser pulse (no RIT)

0.8 ps. The resulting enhancement in the overall maximum energy in the RIT case gives a factor of ~ 3 over the TNSA-proton expansion initialised before RIT occurs and with the truncated pulse. Compared to the L=800 nm interaction, an enhancement factor of ~ 2 is found.

4.5 Conclusions

In summary, by angularly separating protons accelerated by multiple mechanisms in the interaction of ultra-intense laser pulses with ultra-thin Al foils, ion energy enhancement driven by the onset of RIT is investigated.

In addition to a general enhancement arising from the pondermotively driven radial expansion of the volumetrically heated electron, direct laser acceleration of electrons in a self-generated plasma channel results in an additional proton energy enhancement in a localised off-axis region. It has been shown that the enhancement is extremely sensitive to the rising edge of the laser pulse and that an

idealised sharp rising edge laser profile is predicted to produce the highest proton energy enhancement. However, for typical less-than-perfect pulse parameters available experimentally, controlled pre-expansion of the target, by variation of the rising edge intensity profile, enables better conditions for channel formation and energy coupling to electrons and thus protons.

The work presented highlights the criticality of having an ultra-high contrast and well characterised pulse experimentally. If these conditions can be achieved experimentally, much higher proton energies can, according to simulations, be reached. The results provide new insight into the interaction and acceleration physics occurring in the transparency regime of laser-dense plasm interactions. They demonstrate that for the currently available laser and target technologies, with improvement in the contrast and tailoring of the gradient of the rising edge intensity profile, it is possible to achieve much higher proton energies by reducing the ion expansion prior to the onset of relativistic induced transparency. They further demonstrate that for a non-optimal pulse condition controlled target pre-expansion to near critical densities enables enhancement and to some extent tuning of the maximum proton energy.

Chapter 5

Mechanisms of energy transfer to ions during RIT

As covered in chapter 3, typical ion spectra from laser solid interactions have a thermal distribution in the TNSA regime which would not be suitable for many of the proposed applications of laser-ion sources. What is needed then is an ion distribution that can be easily tailored, by either tuning of the laser or the target parameters, to enable control of the ion energy distribution.

This chapter will address energy exchange mechanisms in ion acceleration from thin foils undergoing relativistically induced transparency. It is shown numerically that there are multiple phases of ion acceleration, which include TNSA expansion of the target, an hole boring RPA phase followed by acceleration of upstream ions by the electrostatic shock, and transparency enhancement of the ion population by the transmitted laser pulse. After RIT occurs, an overall enhancement in ion energies is shown to result from the volumetrically heated electrons. This is mediated by the relativistic Buneman-instability It is shown that resonant energy transfer between ion species via the two-stream plasma instability could result in further enhancement of proton energies. A combination of Particle-in-Cell (PIC) simulations and analytical modelling are used to explore mechanisms of energy transfer to ions in the RIT regime.

5.1 Role of streaming instabilities in ion acceleration

In chapter 4 it is shown that the onset of RIT in the interaction of an ultra-intense laser pulse with thin foil targets of tens of nanometres, results in an enhancement of the TNSA accelerated ions.

One explanation that has been suggested to result in enhancement of the ion energies is by a type of two-stream instability, the relativistic Buneman-instability (RBI) [61]. Energy is transferred from the volumetrically heated electrons produced during RIT, streaming through the slower moving expanding ion population. The streaming electrons causes excitation of an electrostatic instability that accelerates the ions through resonant transfer of energy.

The resonant transfer of energy relies on the phase velocity of the instability to be matched to the drift velocity of the expanding ions. In this way energy is transferred from the electrons to the ions. This ultimately would result in a dampening of the field for electrons of a finite energy The co-propagating laser pulse however acts to boost the energy of the electrons [112]. In this way laser energy is coupled indirectly to the ion population via volumetrically heated electrons when the target is relativistically under-dense.

5.2 Particle-in-cell simulations

The energy transfer mechanism was explored with representative 1D and 2D PIC simulations using the EPOCH PIC code. While a limited number of 2D simulations were performed to investigate the consistency of the collective ion behaviour with the lower dimension simulations, the detailed parameter scans and analysis were performed using the 1D code. 1D simulations enable the use of far higher particle number, as well as spatial and temporal resolution to be used. This high numerical resolution is required to investigate streaming instabilities.

5.2.1 1D simulations

Solid density aluminium foil targets of thickness, L, equal to 40 nm and 100 nm with contaminant surface layers of 6 nm, are considered in the simulation study. The contaminant layers were given a mixed hydrogen and carbon composition of density 6×10^{28} m^{-3} and 2×10^{28} m^{-3} respectively.

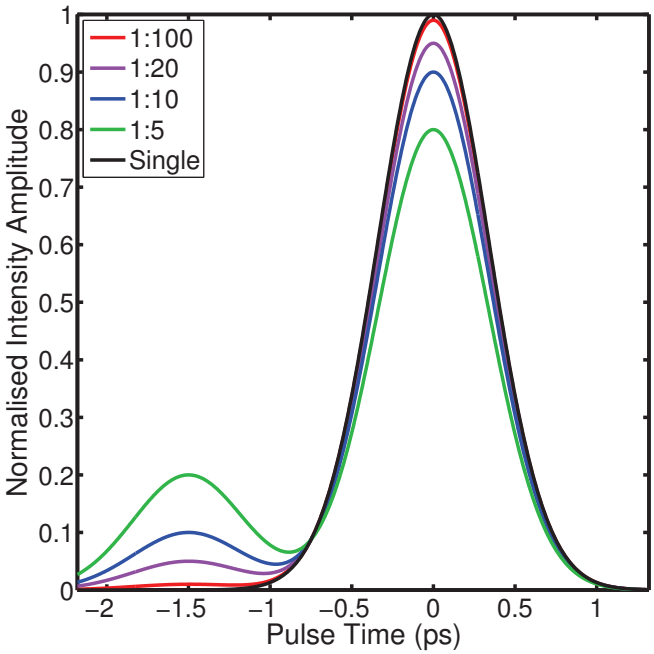

Figure 5.1: Schematic showing intensity profiles modelled in the simulation runs for pre-pulses ratios $E_1/E_2 = 0$ to 0.2 with intensity normalised to the $2{\times}10^{20}$ Wcm^{-2} single pulse case.

The interaction is simulated within a simulation box extending from -10 μm to 350 μm with the target centred at X=0 μm. As noted previously, although the key characteristics of the interaction are observed in 2D, the detailed study requires the greater numerical, spatial and temporal resolution achievable in 1D.

The 1D simulations had a particle number density of 7755 particles per cell. The simulation box consisted of 381540 cells giving a spatial resolution resolution of 0.8 nm and the temporal output of the simulation was 4 fs to enable detailed study of the temporal evolution of the shock formation.

A dual laser pulse is modelled by defining two co-propagating linearly polarised laser pulses of wavelength λ_L= 1.054 μm . The pulses are given a Gaussian temporal profile of 0.8 ps FWHM centred at 0.68 ps and 2.18 ps respectively, giving a peak-to-peak separation of 1.5 ps. The total energy given to the laser

pulse was fixed, $E_L(=E_1 + E_2)$, and the energy-ratio was varied for pre-pulse ratios in the range $E_1/E_2 = 0$ to 0.5. The single pulse peak intensity was equal to 2×10^{20} Wcm^{-2}. The pulse parameters were chosen to mimic those achievable with the Vulcan laser, and similar experimental conditions as those presented in chapter 4.

The EPOCH code includes a field ionisation model which was implemented. This was used to account for the effect of additional ionisation of the bulk plasma that occurs at the point of the target becoming transparent and the laser propagates through the expanding plasma.

To account for the expansion of the laser pulse after focus the E_Y (laser) field is given an exponential damping term equivalent to the Rayleigh length of the TAP focussing parabola, λ_R=30 μm, to address the issue of the laser field spatial decay in 1D, and is shown in figure 5.2.

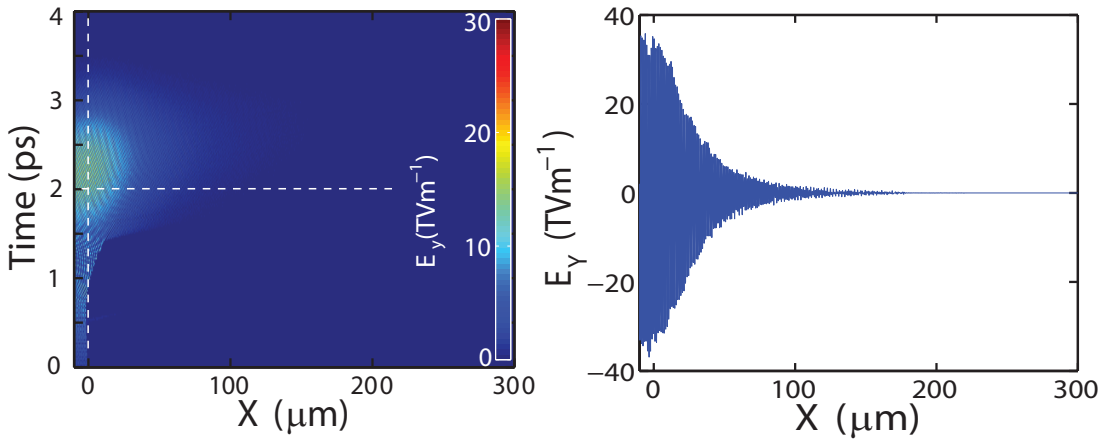

Figure 5.2: (a) Time space plot of simulation output of E_Y field from 0-4 ps, (b) Line-out of E_Y field at 2 ps (after the target has become transparent to the incoming laser pulse) and illustrates the decay of the field beyond 0 μm.

A range of target thickness and pre-pulse ratios were modelled to investigate the transition from TNSA to alternative acceleration processes. Target thickness's of 40 nm and 100 nm initially with single pulse laser configuration were investigated. Initially a 100 nm Al foil target is simulated under the single pulse conditions as a reference case for a single pulse interaction for which relativistic transparency does not occur. The acceleration of ions occurs in a number of phases during the temporal evolution of the interaction. On the rising edge of

the main pulse, heating of the target electrons results in expansion and an initial phase of TNSA is observed to occur, up until ∼0.5 ps into the simulation. The electrostatic sheath, and the differing charge-to-mass ratios (q/m) of the expanding ions, results in differing expansion rates and subsequent layering of the ion species.

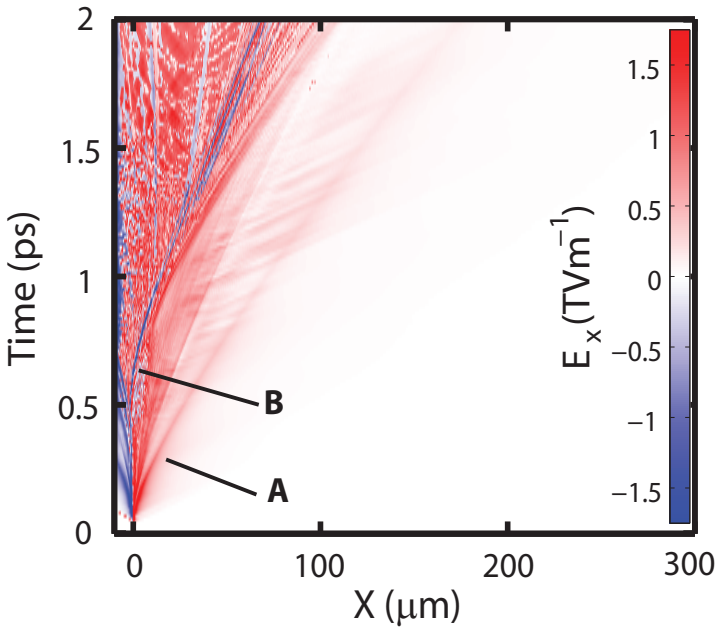

Figure 5.3: Time-space plot of the longitudinal electric field (E_X) from 1D simulation with a 100nm-thick Al foil irradiated by a single laser pulse with $I_L = 2 \times 10^{20}$ Wcm^{-2} and duration $\tau = 0.8$ ps. Two electric field structures are observed corresponding to TNSA, **A**, and Hole-Boring RPA, **B**, phases.

As sheath expansion continues, a second acceleration phase occurs. At this point the target is accelerated by the radiation pressure in the hole boring mode (HB), due to the reduction in density from target expansion, until the laser pulse has decayed. This can be seen looking at the temporal evolution of the longitudinal electric field components (E_X) as shown in figure 5.3. From the $X = 0$ μm point of the simulation, the initial sheath field, labelled **A**, leading to expansion of the rear of the target can be seen, resulting in the layering of the ion species, with the higher q/m protons at the fore of the expansion. At $t = 0.6$ ps, still on the rising edge of the pulse and with increasing laser intensity, the front surface of the target begins to be accelerated forward under the laser pressure, resulting in a second propagating electric field structure, labelled **B**.

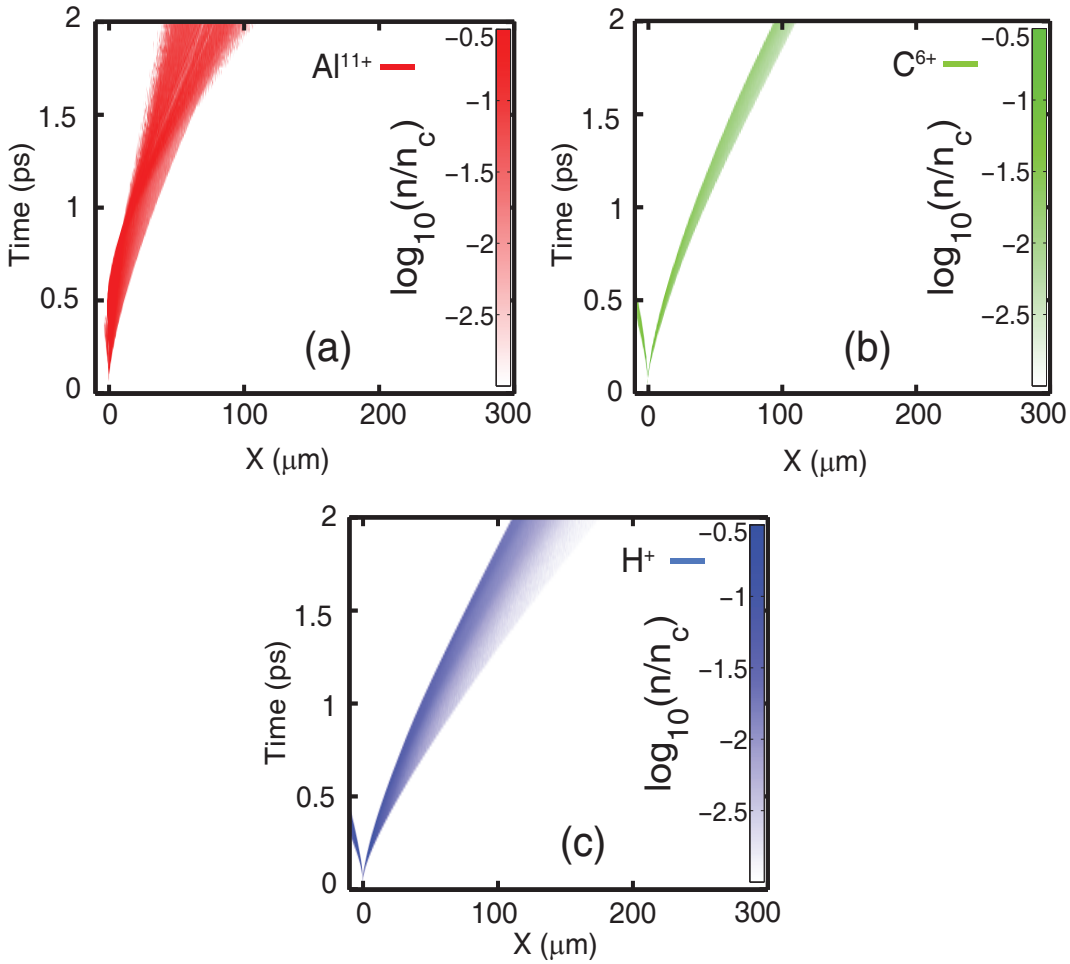

Figure 5.4: Time-space plot of (a) Al^{11+}, (b) C^{6+} and (c) H^{+} ion densities for the single pulse, $L = 100$ nm case.

The bulk Al^{11+} ions initially expand via sheath expansion until the point where radiation drive becomes significant. Due to the increased intensity of the laser pulse coupled with expansion of the target, a phase is reached where the rear of the expanding layer is driven forwards through the expanding proton population by the radiation pressure accelerated electrons and two distinct populations expanding with different velocities can be observed as in figure 5.4(a). This RPA ion population is only accelerated between 0.6 ps and 1 ps, after which the laser pulse has decayed and the electric field from the accelerated electrons propagates through the simulation box.

The target in this case does not become relativistically transparent to the laser pulse. It is seen from figure 5.4 that although the target undergoes RPA during

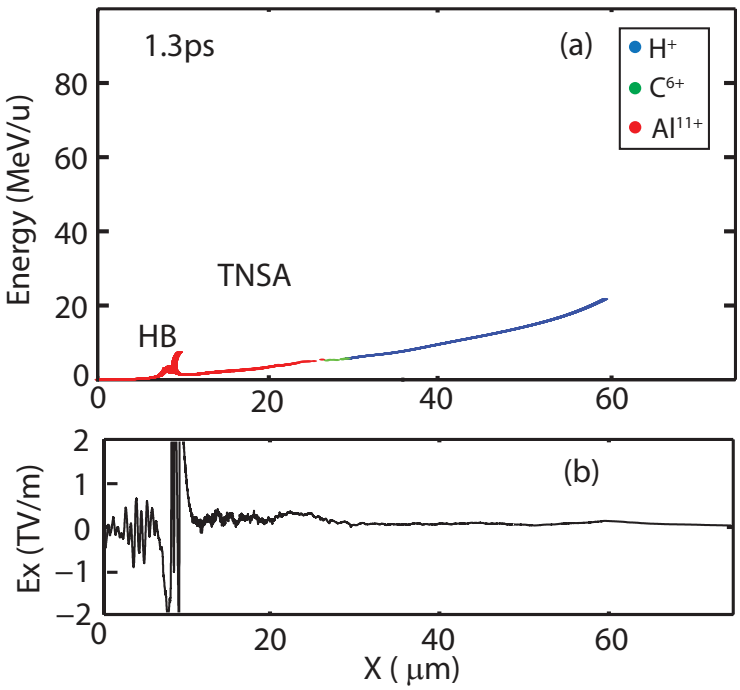

Figure 5.5: Plot of the (a) ion phase space from 1D simulation for the single pulse, $L = 100$ nm target, showing the TNSA expansion and HB RPA phase(red - Al^{11+}, green - C^{6+}, blue - H^{+}), and (b) corresponding longitudinal electric field (E_X) at 1.3ps into the simulation.

the envelope of the laser pulse, the carbon and proton expanding layers are not affected by this phase as they have already expanded significantly. Figure 5.5 shows the magnitude of the longitudinal (E_X) field structures of the TNSA and RPA acceleration phases. After the laser pulse is no longer present in the interaction, these field structures propagate with a constant velocity. The acceleration can therefore be seen as a hybrid TNSA-RPA scheme.

A second case considers the same single pulse laser conditions, incident on a thinner $L = 40$ nm Al target. In this case, RIT of the target occurs near to the peak of the pulse. Under these conditions, similar to the $L = 100$ nm, a hybrid TNSA-RPA acceleration scheme is experienced by the ions up until the point of transparency at $t = 0.45$ ps. These two acceleration phases are shown as features **A** and **B** in E_X shown in figure 5.6.

During the transparency phase, volumetric heating of the target electrons results in a fast propagating E_X field structure leading to enhanced energies of all ion species, labelled feature **C** in figure 5.6. This is observed as a change in the gradient of the expanding carbon and proton densities, shown in figure 5.7(b)

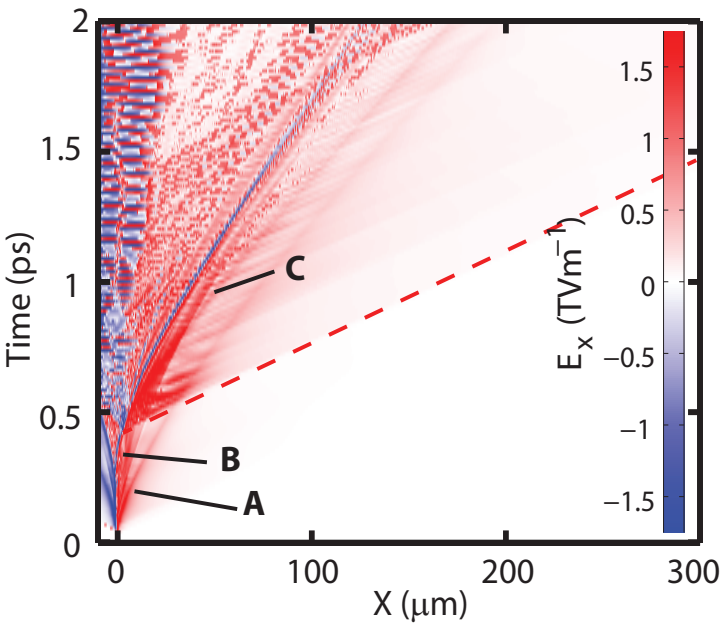

Figure 5.6: Time-space plot of the longitudinal electric field (E_X) from 1D simulation with a 40 nm-thick Al foil irradiated by a single laser pulse with $I_L = 2 \times 10^{20}$ Wcm^{-2} and duration $\tau = 0.8$ ps. Two electric field structure are observed corresponding to target normal and radiation pressure acceleration phases in addition to a third corresponding to a propagating shock, labelled **A**, **B** and **C** respectively.

and (c). In the aluminium density plot, figure 5.7(a), this can be seen clearly as two distinct populations, the TNSA and also a more energetic fast Al population ahead of the expanding layer after t = 0.6 ps.

The carbon and proton density plots both show a similar feature, as a faster population, though to a lesser degree due to the larger spatial extent of these layers. The propagation of the laser pulse front after the target has become transparent is marked in figure 5.6 by the dashed red line.

A third scenario takes the same $L = 40$ nm target irradiated with the same total laser energy, but in the dual pulse configuration with the energy split between two pulses with ratio $E_1/E_2 = 0.1$. The temporal evolution of the electric field structures during these phases can clearly be seen in figure 5.8.

The lower intensity of E_1 means that the C^{6+} ions are produced predominantly after the target has become transparent and the lower charge states are further ionised in the presence of the laser field. This is illustrated in figure 5.9(b). Similar to the single pulse shown before, the interaction evolves through a TNSA-

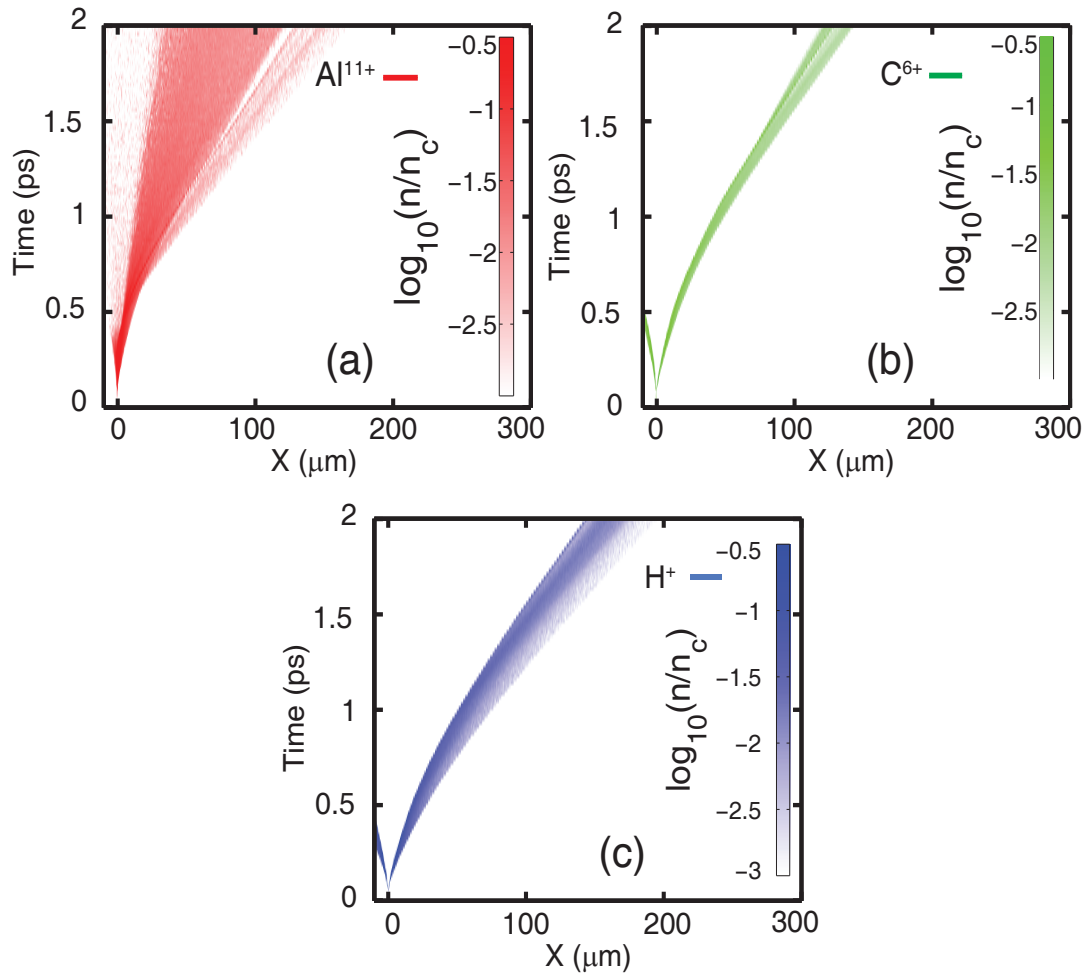

Figure 5.7: Time-space plot of (a) Al^{11+}, (b) C^{6+} and (c) H^{+} ion densities for the single pulse, $L = 40$ nm case.

RPA hybrid acceleration scheme until the point of transparency, shown as the field structures **A** and **B** in figure 5.8. During the transparency phase of the simulation, rapid heating of the electrons in the presence of the laser pulse results in an electrostatic shock being launched in the forward direction corresponding to the electric field structure **C** in figure 5.8. The travelling field structure is dampened as it passes through the expanding aluminium population and energy is transferred to the Al ions which are reflected from the shock front.

As well as field structures associated with TNSA, RPA and shock accelerations, labelled **A**, **B**, and **C**, respectively, another is observed to propagate later in time during the simulation. The electric field, **D**, grows from the shock acceleration phase and propagates through layered ion species, exchanging energy

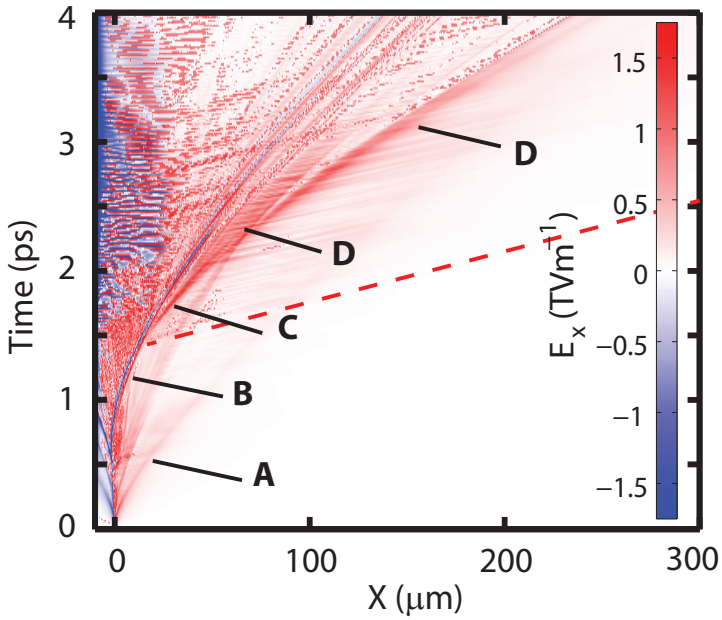

Figure 5.8: Time/space plot of the longitudinal electric field (E_X) from 1D simulation with a 40 nm-thick Al foil irradiated by a dual laser pulse with $E_1/E_2 = 0.1$. Three electric field structures are observed corresponding to target normal, radiation pressure acceleration and shock acceleration phases, labelled **A**, **B** and **C**. In addition, a fourth field structure is shown to grow later in time, labelled **D**.

to them in the process. At the point of transparency, a shock front is launched that propagates into the expanding Al layer, reflecting the upstream ions. The reflected ion population is low in flux, $\approx 2\%$ of the total ion number, gains significant energy from the shock wave and propagates into the expanding higher q/m ion populations.

Figure 5.9 shows the temporally evolving ion density distributions of the expanding target. At 1.5 ps, the shock accelerates a proportion of the expanding Al ions to higher energies and this can be observed as a clear secondary population in the ion density map in figure 5.9(a), and the gradient of the population shows that it is much faster than the transparency enhanced TNSA expansion. Comparison with the corresponding carbon and proton density maps shows that this low flux high energy population is able to penetrate into these layers. The carbon ions gain some energy from the movement of the high energy aluminium ions passing through them. However when the fast aluminium population reaches the back of the proton expansion layer, the lower energy protons are shown to

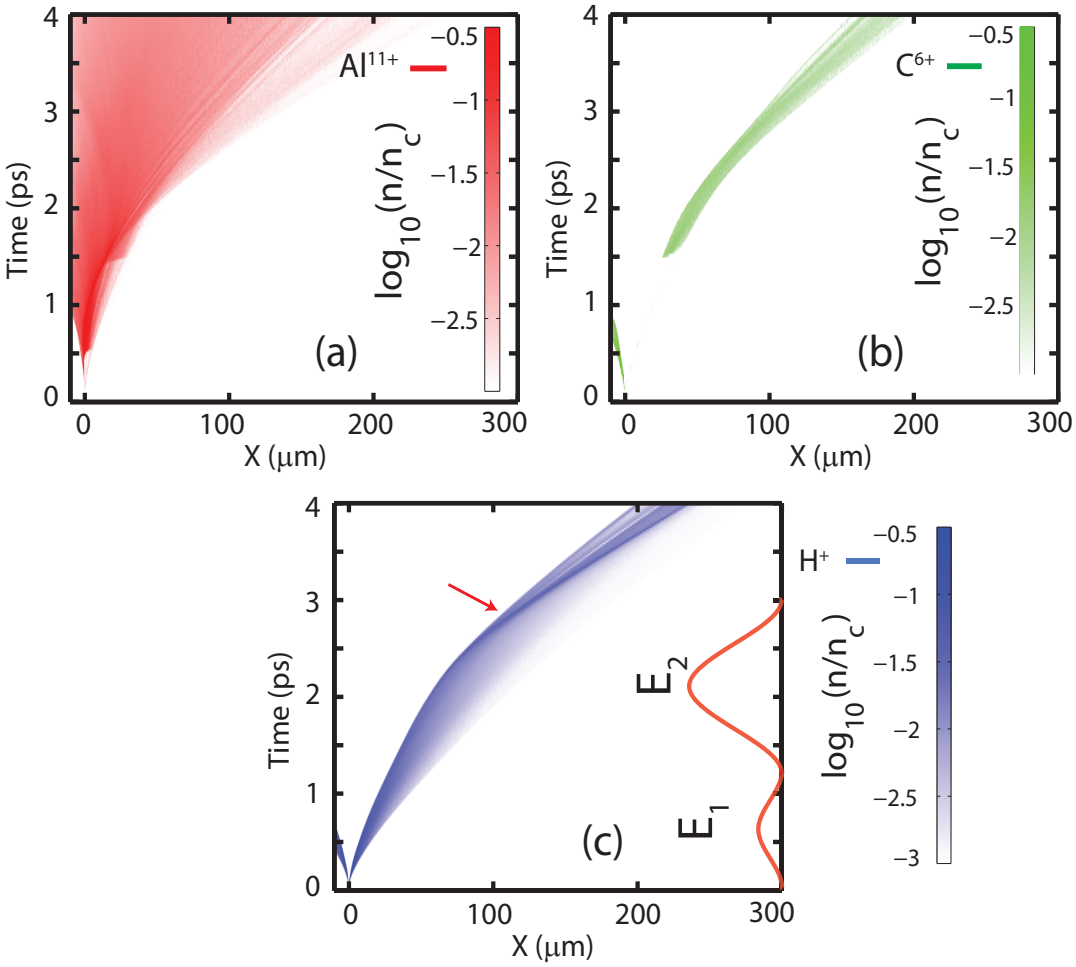

Figure 5.9: Ion density maps of (a) Al^{11+} ,(b) C^{6+} and (c) H^+ for a $L = 40$nm target irradiated by dual laser pulses where $E_1/E_2 = 0.1$, as a function of time. Inset in (c) is the temporal intensity distribution of the double pulse

gain considerable energy.

A population originating from the rear of the proton layer, labelled **D** in figure 5.9, gains a much higher velocity than the background population and begins to move through and overtake the expanding protons. Comparison with the temporal longitudinal electric field, E_X, shows that originating from the point at which shock acceleration of the bulk Al occurs, a strong field grows with the propagating ions.

To investigate this field structure further, it is necessary to look at the phase space of the particles. The phase space is shown in figure 5.10 for two time steps during the simulation, corresponding to both before, at 2.4 ps, and after, at 3.6 ps, the interaction of the shock accelerated aluminium ions with the proton

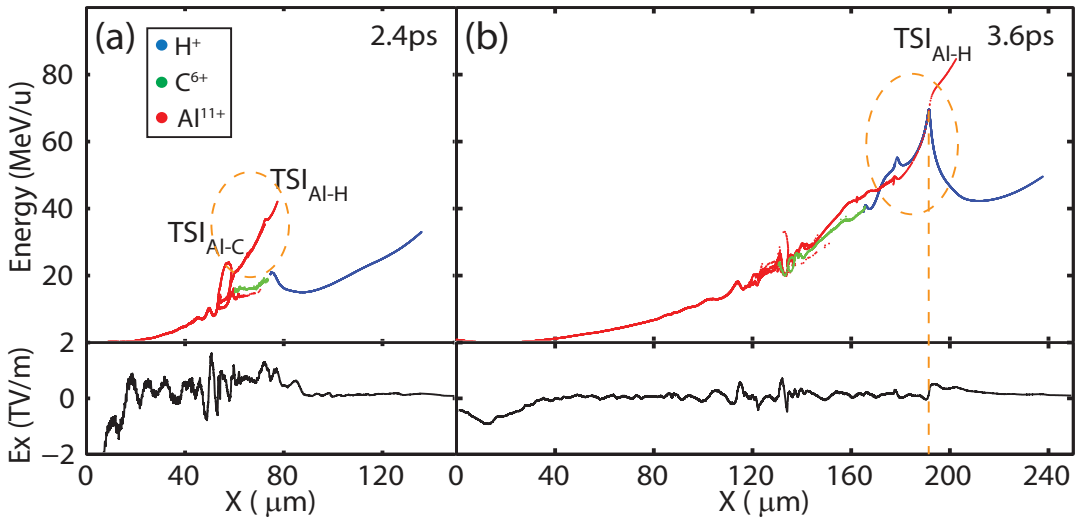

Figure 5.10: Plot of the ion phase space (red - Al^{11+}, green - C^{6+}, blue - H^+) from 1D simulation of $L = 40$nm target and $E_1/E_2 = 0.1$ at two time steps,(a)$t = 2.4$ ps and (b) $t = 3.6$ ps, in the simulation as well as the corresponding longitudinal electric fields (E_X).

expansion, in (a) and (b), respectively.

Figure 5.10 shows the electrostatic shock as well as the shock accelerated aluminium ions, highlighted by the dashed orange ring, as they propagate through the aluminium and carbon layers. As they reach the back of the proton layer, the velocity of the low energy tail of the proton expansion is boosted in energy. By looking at the longitudinal electric field, plotted below the phase space in figure 5.10(a), electric field growth can be seen at the interface between the two populations which acts to accelerate the protons.

Further propagation of the fast aluminium into the proton layer, at 3.6 ps, shows significant modulation of the proton phase space, and boosted proton energies above that of the high energy TNSA expansion. Correspondingly, the aluminium phase space shows a hollowed region, in figure 5.10(b) and highlighted by the orange ring between $X = 150 - 200\mu$m, where energy has been lost to the protons.

The transfer of the energy from the aluminium to the protons is caused by the ion two stream instability (TSI) that results in a strong longitudinal electric field that is maintained over hundreds of microns and ultimately results in an additional acceleration phase of the protons as is seen by the change in slope

after 3 ps, and illustrated by the red arrow, in figure 5.9(c).

The acceleration of ions from the shock, feature **C**, lasts for a finite time due to loading of the shock and in this sense is different from idealised shock acceleration schemes. The shock structure that reflects the population of aluminium ions can still be seen, though with a lower field strength at $X \simeq 130$ μm in figure 5.10(b), and thus it cannot be the propagating shock that causes the proton enhancement observed. The resulting fast Al ions stream through the slower expanding Al layer resulting in the growth of an additional electrostatic field. As this field grows in time there is a resonant energy exchange between the two ion populations whereby the wave eventually reaches a saturation point in which a component of the fast Al population begins to decelerate resulting in an acceleration of the slower Al ions.

This acceleration would ordinarily result then in a dampening of the field, however due to the onset of transparency at a critical point on the rising edge of the main laser pulse, the field of the propagating laser pulse volumetrically heats the electrons in the expanded particle layers. This results in an increase in the ion acoustic velocities and thus an additional increase in particle expansion and shock velocities.

When the fast Al ion population streams through the expanded layers, as in figure 5.10(a), further streaming instabilities grow due to the existence of multiple ion populations with differing relative velocities. The most notable of these instabilities occurs when the accelerated Al ions reaches the expanded proton layer, as shown in figure 5.10(b).

Compared to the equivalent interaction driven by a single laser pulse of the same total energy, the pre-expansion driven by the pre-pulse results in reduced plasma densities and thus ensures that the growth rate of the instability is much lower temporally and spatially. This feature of the dual pulse configuration enables efficient energy exchange between ion species to occur over an extended distance, resulting in significant proton energy enhancement as shown in figure 5.10(b).

Figure 5.11 shows a comparison of the ion spectra corresponding to two dif-

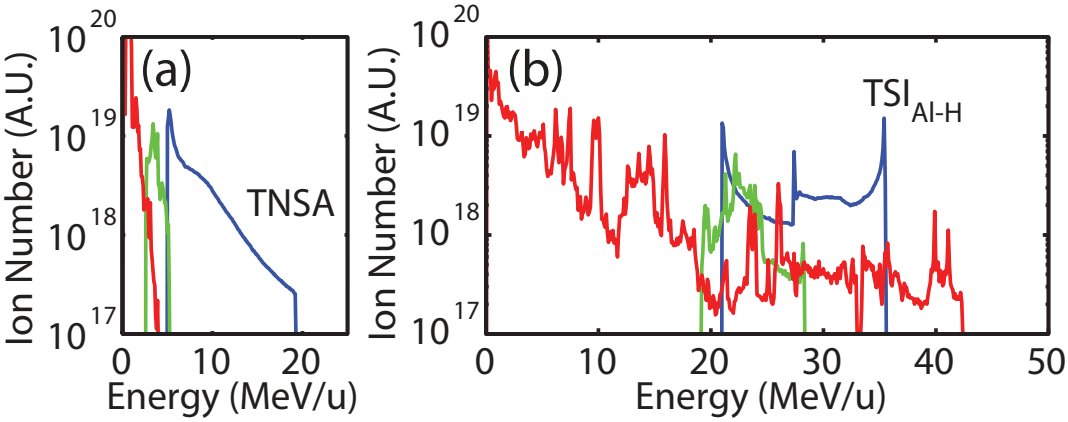

Figure 5.11: Ion energy spectra (red - Al^{11+}, green - C^{6+}, blue - H^{+}) extracted from the simulation at (a) 0.8 ps and (b) 3.8 ps, for $L = 40$ nm and $E_1/E_2 = 0.1$.

ferent points in time. The first, shown in (a) corresponds to the TNSA phase at 0.8 ps from the start of the simulation where the ions show a typically thermal distribution expected from TNSA expansion. Part (b) shows the energy spectra of the ions sampled at a time of $t = 3.8$ ps from the start of the simulation and shows the Al ions extending up to high energies and the effect of the streaming of these ions on the proton spectrum resulting in enhanced energies.

The resulting proton spectrum shows multiple peaked features and displays a non-thermal distribution in contrast to spectra from earlier in time as in figure 5.11(a).

5.2.2 Instability analysis

The relative role that both the relativistic Buneman and the ion two stream instability play in the transfer of energy to ions in targets undergoing RIT, and under dual pulse conditions is examined by considering the (ω, k) spectra from the simulation results of the dual pulse condition ($E_1/E_2 = 0.1$) shown in figure 5.8 and 5.9.

The spectra are obtained at two pivotal time and space intervals: (1) 1.4-2.2 ps and 10-50 μm, corresponding to the period immediately after transparency; and (2) 2.2-3.8 ps and 80-250 μm, corresponding to the phase of enhanced proton acceleration.

Figure 5.12(a) shows (ω, k) plots of the simulation for the temporal and spatial

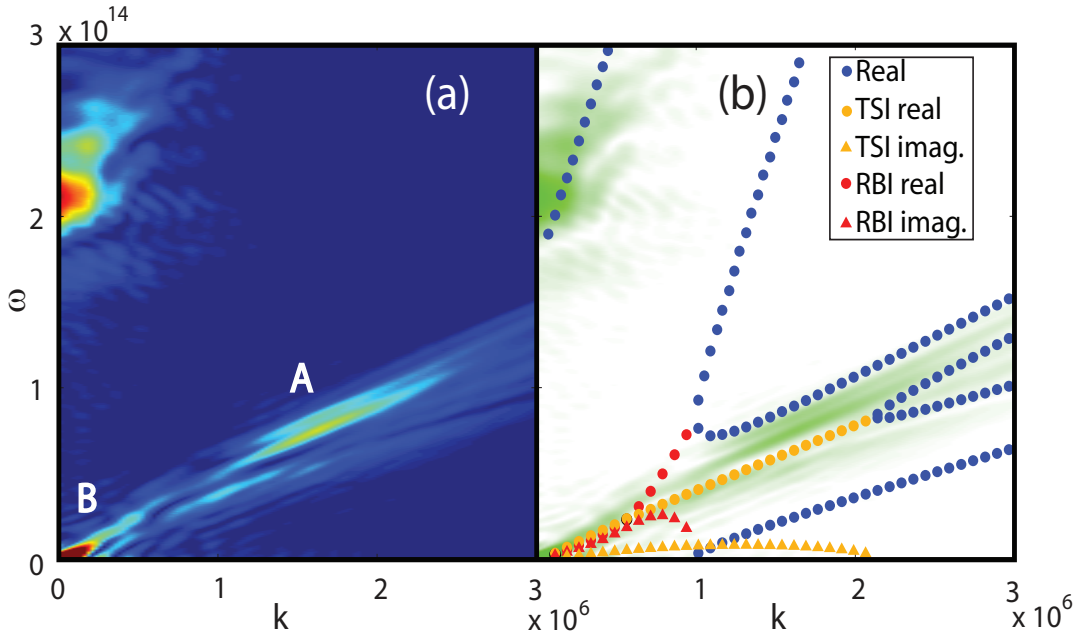

Figure 5.12: (a) Spectral power as a function of frequency and wavenumber for t=1.4-2.2 ps and X=10-50 μm. Instability excitation is observed at A and B. (b) Analytic solutions to the combined dispersion relation for the ion-TSI and RBI. The spectral power is reproduced in the background (faint green) to aid the comparison.

extent (1). The Fourier transform of the waves excited in the plasma over this temporal range yield ω and k. The main excitation modes are shown labelled as A and B. Figure 5.12(b) shows the linear plasma dispersion relation, solved to yield roots $\omega(k)$ and the corresponding growth rate $\gamma(k)$ for the combined ion two stream and relativistic Buneman instabilities, given by:

$$\frac{\omega_{pi1}^2}{(\omega - kv_{i1}^2)} + \frac{\omega_{pi2}^2}{(\omega - kv_{i2}^2)} + \frac{\omega_{pe1}^2}{(\omega - kv_e^2)} = 1 \tag{5.1}$$

where ω_{pe1} and v_e are the plasma frequency and velocity of the electron population, ω_{pi1} and v_{i1} are the plasma frequency and velocity of the aluminium population, and ω_{pi2} and v_{i2} are the plasma frequency and velocity of the proton population. This equation has been solved for the relativistic electron population streaming with the fast and slow Al ions and the fast Al ions streaming with the protons.

The electron Lorentz factor, ion velocities and densities are extracted from the simulations within the corresponding time and space regions to produce the approximate linear solutions to equation 5.1 and shown in figure 5.12(b).

The real solutions correspond to waves that can propagate due to the coupling of plasma oscillations of the different particle populations. However, the instabilities grow in the region where there are complex solutions to the dispersion equation. The real component shows the unstable wave properties whereas the imaginary component corresponds to the wave growth.

In figure 5.12(b), the solutions are plotted with the spectral power from the simulation reproduced in the background to aid comparison. The dotted blue circles correspond to the real solutions, the orange and red circles are the real solutions for the ion-TSI and RBI instabilities respectively. The triangles mark the imaginary solutions, and growth rates, of the ion-TSI and RBI, given by the orange and red, respectively.

The main excitation modes A in figure 5.12(a), correspond to the ion-TSI branch with comparison to the analytic solutions presented in figure 5.12(b). The values and gradient are in good agreement with the numerical solution. The excitation, B, is more likely to result from a RBI-like instability growth mode due to the presence of a high frequency real wave, corresponding to the blue dotted line at $\omega = 2 - 3 \times 10^{14}$ s^{-1}.

Figure 5.13(a) shows the (ω, k) of the transformed data taken from the simulation over the temporal and spatial region (2) described above, with the corresponding analytic solutions to the plasma dispersion, in equation 5.1, given in figure 5.13(b) with the spectral power plotted for comparison.

The strong excitation modes labelled C and D at this later temporal period are also consistent with the ion-TSI and RBI solutions, respectively. The close proximity of the complex solutions however means that there may be additional coupling between these two streaming instabilities.

The dispersion solutions are indicative of a set of fixed plasma frequencies and velocities, whereas in the numerical simulation these values are constantly evolving. Nevertheless, this approximation shows the growth of the E_X fields arising from the streaming populations of both relativistic electrons and fast ions through the lower temperature ion background.

The analysis above indicates that ion-TSI in addition to RBI is a possible

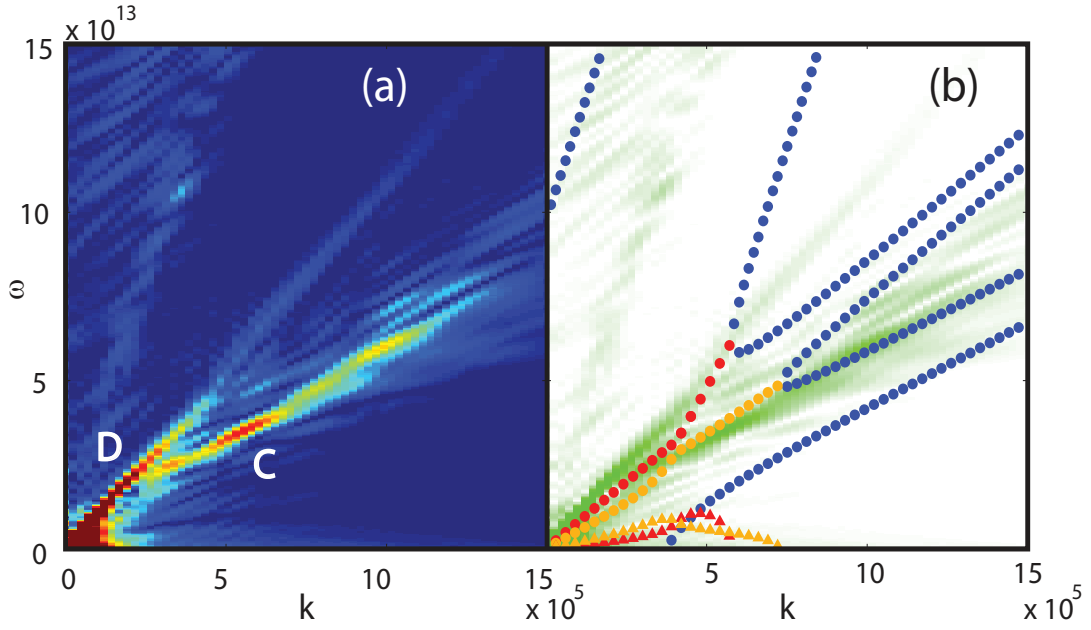

Figure 5.13: (a) Spectral power as a function of frequency and wavenumber for t=2.2-3.8 ps and X=80-250 μm. Instability excitation is observed at C and D. (b) Analytic solutions to the combined dispersion relation for the ion-TSI and RBI. The spectral power is reproduced in the background (faint green) to aid the comparison.

energy transfer mechanism in the case of targets simulated undergoing significant pre-expansion, driven by the dual laser pulses, evidenced in the dominant modes observed in the dispersion solutions and in the interaction of the ion species as shown in figure 5.10.

5.2.3 Scaling with target pre-expansion

Considering the effect of the rising edge profile of the laser explored in the previous chapter, a range of dual pulse ratios are also simulated to investigate the extent to which the role streaming play in expanded plasmas. In the case presented previously $E_1/E_2 = 0.1$, however ratios in the range of $E_1/E_2 = 0.01 - 0.5$ were also simulated.

The scaling of the maximum measured energy of the streaming protons from the simulations with E_1/E_2 is shown in figure 5.14. It is found that with the addition of increasingly larger pre-pulses, conditions for efficient shock formation and launch are reached resulting in effective Al energy gain. The pre-expansion resulting from the larger pre-pulse enables densities to be reached for substantial

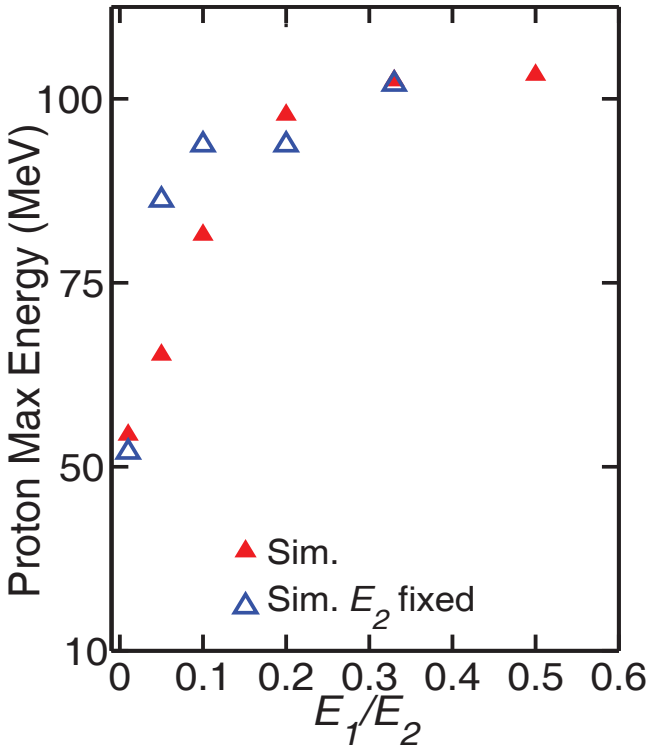

Figure 5.14: Scaling of the maximum proton energy of the streaming enhanced population, with target pre-expansion (E_1/E_2), from 1D simulations.

coupling of energy from the fast Al to be achieved. Saturation of the proton maximum energy is observed to occur as large E_1/E_2 are reached due to the increased expansion and dispersion of the ion species at early times. The increased expansion of the protons means that the fast Al ions reflected from the shock front have to catch up with the protons, by which point the conditions for energy transfer via ion-TSI are less favourable due to the decreased density and the relative velocities between the species.

The single pulse condition shows significantly higher energies than any of the dual pulse schemes simulated. This has been found to be due to the reduced expansion of the layered ions before the onset of transparency, similar to the discussion in chapter 4. In this case, when transparency occurs the proton layer is much closer to the simulation zero, interaction point. When the laser pulse breaks through, rapid volumetric heating of the electrons in the dense proton layer occurs. In this scenario, considerable energy transfer to all ion species is observed to occur via the RBI mechanism.

5.2.4 2D simulations

The detailed study of the possible mechanisms of energy coupling from the laser to ions in the transparency regime has been done in 1D simulations due to the high increase temporal, spatial and particle number resolution that can be achieved, and is necessary to investigate these processes in detail. It has been shown that post-transparency, additional electron heating and enhancement of the bulk ion species results in an enhancement in the maximum energy of the protons via streaming instabilities.

To investigate multi-dimensional effects on these processes, 2D simulations under the same conditions have also been performed. The 2D simulations used a $\lambda = 1.054$ μm laser pulse with a 0.8 ps FWHM and an intensity of 2×10^{20} Wcm^{-2}. The laser had a Gaussian spatial intensity distribution of diameter d =7 μm FWHM, comparable with experimentally achievable focal spot measurements. In the dual pulse mode, two pulses with varying intensity ratios are separated temporally by 1.5 ps.

The interaction is simulated within a simulation box extending from -10 μm to 350 μm with the target centred at X=0 μm. The 2D simulations had a particle number density of 100 particles per cell. The simulation box consisted of 381540 cells giving a spatial resolution resolution of 4 nm $\times$ 8 nm and the temporal output of the simulation was 100 fs. Due to the size of the output files, output frequency was reduced, which means that fine temporal resolution of the interaction evolution is not possible. The simulations considered both single and dual pulse conditions for $L = 40$ nm targets.

Figure 5.15 shows the temporal evolution of the ion densities. The Al^{11+}, C^{6+} and H^{+} ion densities are represented by the red, green and blue plots respectively. In the early time steps, the target expands with behaviour that is expected in the TNSA regime, with the ion species layered by q/m. At $t = 2.2$ ps, the effect of transparency has acted to boost the Al^{11+} ions, accelerating them to higher velocities than the back of the expanding C^{6+} ion layer. The rapidly expanding Al pushes and deforms the rear of the expanding carbon layer.

It was found that, like the 1D, at the point of transparency a shock is launched

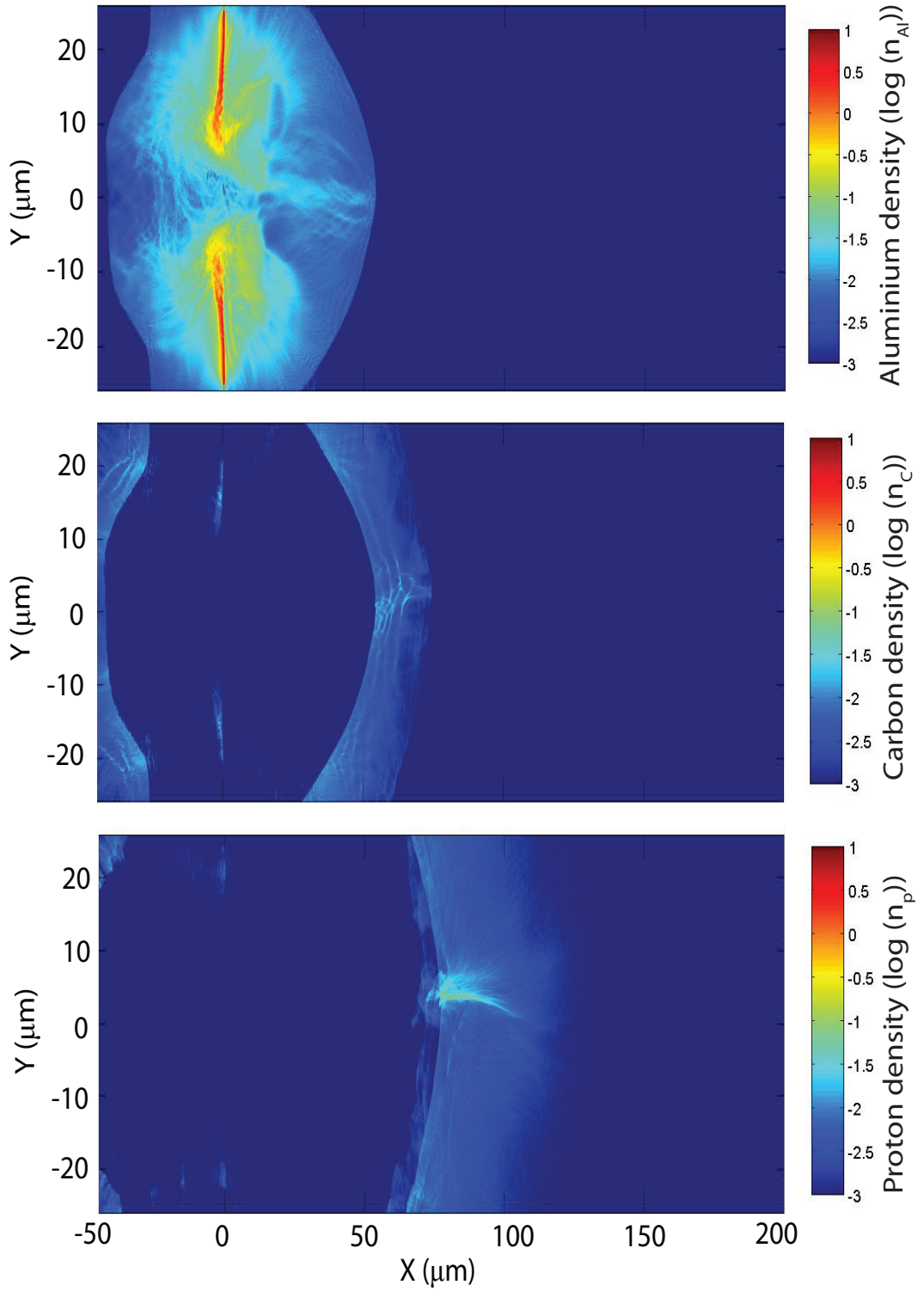

Figure 5.15: 2D maps of the (a) Al^{11+}, (b) C^{6+} and (c) H^{+}, sampled at a time $t = 2.5$ ps into the simulation.

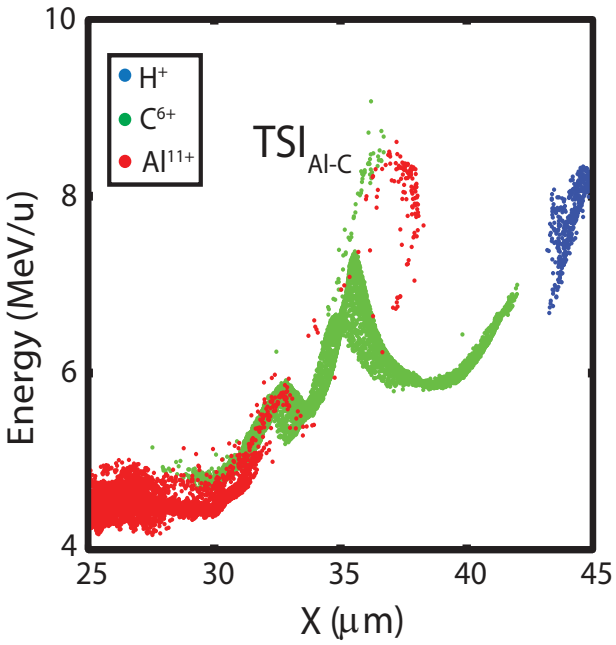

Figure 5.16: Example phase space showing the interface of the expanding ion species and streaming between the fast Al^{11+} ions that have propagated into the C^{6+} layer, labelled TSI_{AL-C}.

in the forward direction, however the efficiency of the shock in the acceleration of Al was low, resulting in much lower energies and fluxes of the population. The lower velocity of the shock accelerated ions means that they do not catch up and propagate through to the proton layer in the time and spatial scale explored in these simulations. The fast aluminium's do however propagate into the carbon layer, and two-stream instability interaction between the two species is observed.

Figure 5.16 shows the phase space zoomed into the spatial window of $X = 25 - 25$ μm at $t = 1.2$ ps, showing the carbon layer and the interfaces between all three ion species. It is seen that the fast population of ions is of low flux, but does result in a coupling of energy into the carbon population, resulting in a similar phase space feature as that of the Al-H observed in the 1D simulations.

It is evident then that the streaming of a faster ion population through a slower population, resulting in energy exchange between the species, occurs in higher dimensions.

Looking at the ion density at 3.2 ps, as shown in figure 5.15, close to the axis of the laser, there are filaments of density going through all three ion species. The beginnings of this can also be seen within the Al alone at earlier time steps,

and propagating through to the higher q/m ions with the temporal evolution of the simulation. These regions also correspond to that of enhanced ion energies observed in chapter 4 due to channel formation, and it is found that during transparency, all ion species experience a boost in energy.

The 2D simulations show that the conditions are not optimal for efficient shock acceleration of the bulk Al ions. The laser pulse is tightly focussed and a quasi-1D scenario has not been met for efficient shock acceleration.

The Al ion velocity after reflections is not sufficient to catch up with and drive them through the proton layer and hence ion-TSI of the Al and protons is not observed during the time of the simulation. This may however occur at later times when the Al reaches the proton layer.

When the 2D ion density maps are compared with the electron density and energy maps, shown in figure 5.17(a) and (b), it is seen that the density filaments are overlaid with regions of high electron density and the most energetic electrons.

The 2D simulations show that a jet of energetic electrons are produce in the vicinity of a plasma channel. The electrons within the channel receive a boost in energy, to the $\sim$30 MeV level, resulting from direct laser acceleration due to the propagating laser pulse, as discussed in chapter 4.

In the electron energy map, there are two side bands that correspond to regions of electron density that are volumetrically heated by the laser pulse, whereas the centre region of highest energy is as a result of direct acceleration of the electrons in the laser field.

The plasma channel is sustained longitudinally through the expanding ion layers and enables exchange of energy over the extended length. Comparison with figure 5.17(c), the 2D proton energy map, shows that a localised region within the expanding layer is enhanced in the presence of the high energy electrons indicating a coupling between the two populations. Similar effects are also seen within both the aluminium and carbon populations. Figure 5.18 shows the temporal evolution of the ion density throughout the simulation. It is seen from (c) and (d), corresponding to time steps 2.2ps and 3.0ps that the ion density is modulated by the propagation and enhancement in the vicinity if the plasma channel.

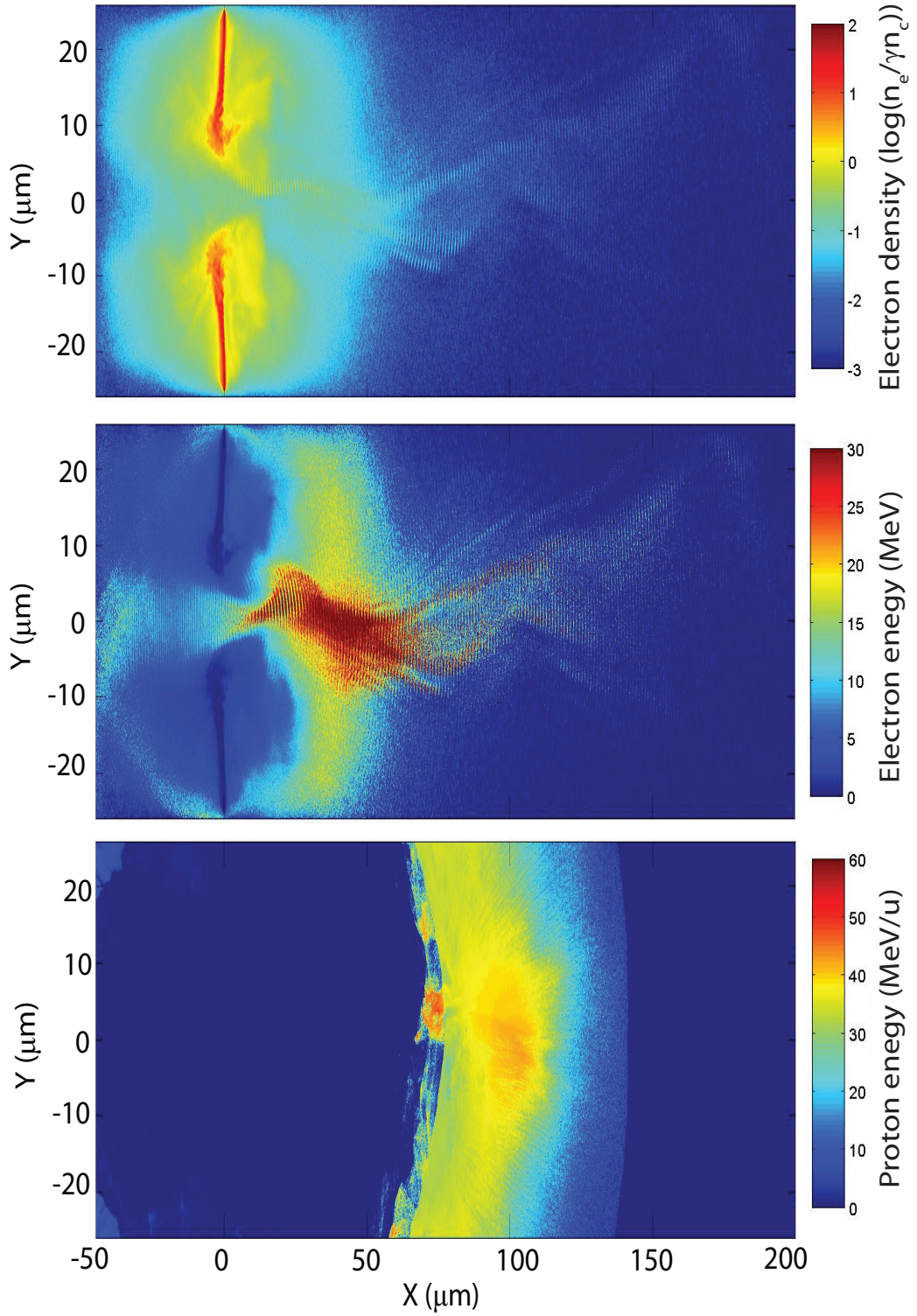

Figure 5.17: 2D maps of the (a) electron density, (b) electron energy and (c) proton energy taken at a time $t = 2.5$ ps into the simulation.

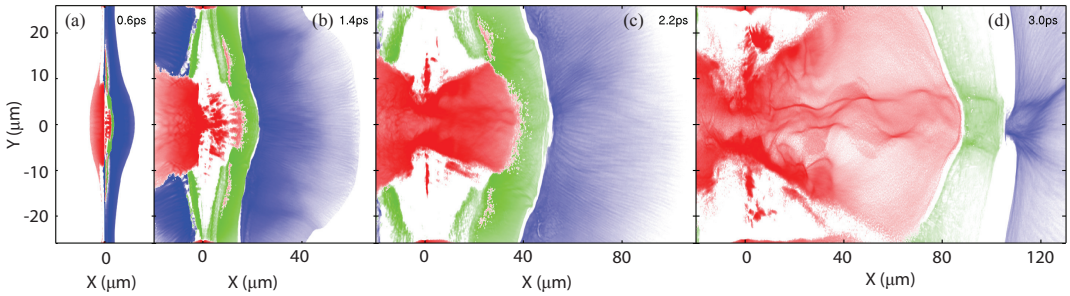

Figure 5.18: Temporal evolution of the 2D ion density (Al^{11+} - red, C^{6+} - green and H^{+} - blue) taken at (a) 0.6 ps, (b) 1.4 ps, (c) 2.2 ps, and (d) 3 ps.

Coupling of energy between the laser and the ion populations during transparency was observed to be mediated primarily through the relativistic Buneman instability (RBI). It was also observed that energy exchange occurs between high energy heavy ions, Al, with the higher q/m carbon ions via the two-stream instability. Due to the restraint on the temporal output frequency from the 2D simulations, it was not meaningful to produce a (ω, k) spectrum. As such the temporal dynamics and the growth of the instabilities could not be investigated in detail.

It is shown that there is additional coupling of laser energy into the expanding ions via streaming instabilities after transparency has occurred, both ion-TSI and RBI, resulting in an overall energy enhancement. It is observed that although there is an element of inter-species ion streaming, the largest enhancement is as a result of the transparency enhanced electron population streaming under the conditions that were simulated in this study.

5.3 Summary and conclusion

Using 1D and 2D simulations it has been demonstrated that during RIT, a boost in the energy of sheath-accelerated ions occurs and that this arises due to electron-ion and ion-ion two stream instabilities.

In addition to streaming of the volumetrically heated electrons with the co-propagating ions, streaming between transparency enhanced heavy ions moving through the expanding ion populations was also observed resulting in significant

energy transfer. The 2D simulations also showed streaming between the heavy ion species, however decreased efficiency of the acceleration of the heavy ions from the shock launched at the point of transparency, meant that within the temporal window simulated, this population had not reached the proton layer.

The primary energy transfer mechanism observed in the 2D simulations was from the electrons via the RBI in a plasma channel extending out through the expanded ion layers. The channel formation is discussed in chapter 4.

For significant ion-ion two-streaming to occur in 2D, much higher heavy ion energies and fluxes are required for the population of fast aluminium to stream with the protons. One potential reason for the decreased efficiency of the shock accelerated aluminium population is the large spatial intensity gradients with a tightly focussed laser pulse. Efficient shock acceleration requires quasi-1D drive conditions [125]. The role of ion streaming as an energy transfer mechanism could be explored by reaching a 1D-like condition such that efficient shock acceleration can occur. This could be achieved by using a larger focal spot, albeit this results in reduced peak intensity if the laser pulse energy is conserved.

Though this work has looked primarily at the excitation of longitudinal instability growth, it is likely that streaming in 2D will also result in the growth of transverse instabilities such as the Weibel instability [63, 152–154]. These could result in breakup of the ion beam, resulting in 2D spatial intensity profiles similar to the Rayleigh-Taylor unstable beams shown in chapter 4.

In summary, it was found that streaming instabilities play a key role in the transfer of energy to ions in the RIT regime. As well as the RBI instability growth from electron-ion interaction, it was found that the ion-ion two-stream instabilities may also play a role as an energy exchange mechanism in expanded plasmas.

Chapter 6

Conclusions

6.1 Summary

This thesis presents experimental and numerical investigations of the acceleration of protons and heavier ions from intense laser interaction with ultra-thin foils in the relativistic transparency regime. It has been demonstrated experimentally that the rising edge profile of the main pulse is crucial in controlling the expansion of the target for efficient coupling of laser energy into protons. It has also been demonstrated that in this regime by shooting the target at oblique incidence, separation of different proton beam components arising from different acceleration mechanisms, enables measurements of each to be made and to be separately optimised. The transparency enhanced proton population was found to dominate in the target and laser parameter scan presented.

The mechanisms of transfer of energy to ion species in the transparency regime have been investigated numerically and it has been shown that streaming of volumetrically heated electrons and also heavy ions could result in additional transfer of energy from the laser pulse to lighter ions.

6.2 Acceleration of ions from relativistically transparent targets

Recent experimental and numerical investigations of laser interactions with ultra-thin foils have revealed that several distinctly different mechanisms can be responsible for the acceleration of ions, with arguments for both RPA and BOA playing a key role in producing the highest energy ions. The work presented in chapter 4 has identified that in pico-second laser interactions, no single mechanism is solely responsible. By spatially separating multiple components of the proton beam, signatures of a radiation pressure accelerated component identified by the characteristic Rayleigh-Taylor instability bubble profile and laser-directed beam, indicate that an RPA phase exists during the interaction. A component of the beam is also centred around the target normal axis, indicating that there exists a phase dominated by sheath acceleration.

A third component located in the angular region between both the target normal and laser axis was found to contain the highest energy proton populations. Transverse optical probing images at two different temporal steps showed the formation of a plasma channel at the target rear surface, which extends tens of microns into the vacuum. Numerical simulations in both 2D and 3D indicate also confirm the formation of an extended plasma channel and confinement of the laser pulse within, resulting in enhancement in electron and thereby ion energies over the extended length of the channel.

It has been found that numerically, the highest proton energies are obtained for a single ideal Gaussian pulse. This condition could not be achieved experimentally. Investigation of the TAP pulse profile from a sequoia third order scanning auto-correlator in addition to on-shot auto-correltaion measurements indicate that true single pulse conditions such as that modelled numerically are not replicable experimentally (at this time) and that at a reference time 1.5 ps prior to the main pulse the laser intensity $\sim$5% of the main pulse intensity. This results in expansion of the target prior to the arrival of the peak of the main pulse.

Experimentally it was found that by tailoring the rising edge of the main pulse, by addition of a controlled pre-pulse, the condition could be met such that extended channel formation could be achieved and enables energy transfer from the laser pulse into the expanded proton population during the relativistic transparency phase. This hypothesis is supported by 2D and 3D numerical PIC simulations in which the target pre-expansion has been varied by tailoring of the relative intensity of a pre-pulse prior to the main pulse, and an increase in maximum proton energy by a factor of $\sim$2 observed in the range investigated experimentally.

6.3 Mechanisms of energy transfer in the transparency regime

Previous work has shown that in the relativistic transparency regime, enhancement of the initial TNSA expansion mediated by the relativistic Buneman instability, can result in efficient transfer of energy from the laser-accelerated electrons into the bulk ion population in a relativistically underdense plasma, resulting in enhanced conversion efficiency and maximum energy [61].

Numerical studies of the effect of target pre-expansion on the energy transfer in the relativistic transparency regime show instability growth modes corresponding to the Buneman instability. This is corroborated by analytical solutions to the Buneman instability corresponding to electron-proton streaming mode instability growth.

Instability growth modes were found that indicate that streaming also occurs between the ion species, in particular between fast aluminium and proton species. Phase space analysis showed that energy is transferred between the low flux shock-accelerated aluminium ions as they stream through the expanding higher q/m ions species and in particular energy transfer to the proton population occurs resulting in increased maximum energy.

Higher dimensional 2D simulations also show these features. However efficient shock acceleration of the aluminium ions was not achievable due to the 2D spatial

intensity profile of the laser pulse. The aluminium ions reflected from the shock front did not reach sufficient velocity such that they were able to stream with the proton population, though streaming with the lower q/m carbon ions was observed.

It has been shown that although the Buneman instability plays a role in the exchange of energy from the laser to the ions in the transparency regime, streaming between the transparency enhanced ion species may also play a role. In particular it results in energy transfer from the heavier transparency enhanced bulk ion population to the expanded higher q/m ions.

6.4 Future work

The present state of the art high power laser systems have been used to investigate ion acceleration in thin foils. The results presented in this thesis have shown that the maximum ion energies achievable depend critically on the rising edge profile of the laser pulse, in particular for high charge to mass ratio ions such as protons.

With future multi-petawatt laser systems such as the proposed Vulcan 10PW project [155, 156] and the proposed ELI facilities [157–159], much shorter pulse durations of ∼50 fs with similar nominal energy as Vulcan (∼500 J) mean that much steeper pulse profiles will be achievable. This should produce much higher ion energies.

For current laser facilities and technology, improvement in laser pulse contrast, in particular on the pico-second time-scale, are predicted to yield much higher ion energies and recent experimental evidence has pointed towards this.

The streaming of electrons and ions which occur in targets undergoing RIT also present a unique prospect for probing astrophysical and high altitude geophysical ion acceleration phenomena in the laboratory. Many of the plasma dynamic processes present in such interactions such as two-stream instabilities are analogous to those observed in supernova explosions. The injection of ions accelerated in the transparency regime into tenuous plasma is one possibility of probing such events.

Appendix A

Methods

In this chapter the methods and techniques commonly employed in experimental and numerical studies of ultra-intense laser interactions with solid targets are described. In previous chapters the fundamental physical concepts of the interaction of an intense laser pulse with solid density targets have been discussed. Observation of these processes experimentally requires a range of tools, not least of which is the laser itself, and a range of diagnostics to investigate the properties of the plasma. Putting the experimental measurements into the context of theoretical predictions also requires the use of computational modelling techniques to understand the interaction dynamics.

In this chapter we will describe the laser system, and the laser technology therein, used to produce the high intensity pulses which enabled the study of the ultra intense interactions presented. Common plasma diagnostics, specifically those used in the acquisition of the data presented in the following chapters will then be described in addition to numerical modelling methods used in the interpretation and analysis of the physical data.

A.1 Overview

Experimental laser plasma physics provides a rare opportunity to get first hand experience of working with large scale science experiments at the forefront of technology and the field. Though experimental campaigns can be both mentally

and physically demanding in that the proposed scientific objectives must be completed within the allotted experimental time, typically 5-6 weeks. The race to understand the underlying processes within the experiment then requires careful but swift analysis, understanding of the possible processes and explanations, coordination and planning of shots and resources (targets and laser parameters), and team work.

An experimental laser-plasma physicist, should have the physical and technical understanding of the physics and diagnostics with which to perform measurements, and also be able to communicate this effectively with the team members. This pooling of technical expertise and minds means that seldom during an experiment is there a problem that cannot be overcome.

A typical experimental campaign involves months of work and planning which culminates in 5-6 weeks of beam time in which to deliver the experimental objectives. Of this, setup of the beam-line, defining and referencing of target chamber centre (TCC), and subsequent alignment and installation of diagnostics to TCC may take 1-3 weeks dependant on the complexity of the experiment setup. The experiment itself however is only one half of the story as none of the physics we probe would be attainable, except perhaps on paper, were it not for the laser itself.

A.2 High power laser technology

In ultra-intense laser-plasma physics the laser is simply a tool used in the research, particularly at user facilities where there are entire teams that develop and maintain the laser system, so there can sometimes be an unintentional ignorance toward the generation of the high power pulses used. Of course there are key laser parameters that must be defined such as the pulse duration, energy, wavelength and intensity such that one can probe and examine the underlying physical processes in the interaction either through analytical or numerical modelling. It is important however to understand the limitations of the laser system, particularly in the context of the desired interaction physics that we want to

probe. One such example is the study of ultra-thin foil interactions such as those presented in chapter 4, where the gradient of the rising edge of the pulse is of critical importance, meaning an ultra-high contrast pulse is essential. In the study presented in chapter 4, an ultra-high contrast pulse was necessary as well the introduction of a controlled pre-pulse to the system in the study of the effect of the pulse rising edge on the acceleration of fast ions from ultra-thin foil targets. To have somewhat of an understanding as to how this condition can be achieved it is necessary to have some practical knowledge of the laser system and the processes for the generation of these intense pulses.

In this chapter the technology used in the generation of high power laser pulses in large scale laser systems is discussed. Typical oscillator pulses contain an energy of approximately 10 nJ that must be amplified many orders of magnitude to 100's J to reach petawatt output power.

A.2.1 Chirped pulse amplification (CPA)

Chirped pulse amplification was the paradigm in laser technology that for the first time enabled relativistic intensities, greater than 10^{18} Wcm^{-2} for $\lambda = 1$ μm lasers, to be achieved, driving relativistic electron motion in the laser field [127]. This was a key milestone in the study of relativistic plasmas and compact accelerator technology. To reach these relativistic intensities when focussed at the target, the initial seed pulse with energy of the nJ level, must be amplified by many orders of magnitude up to the 100's J to reach such intensities for a picosecond laser system.

With high power lasers, the pulse passes through the gain medium, gaining energy in the process from the population inversion. However the refractive index becomes intensity dependent for a fluence greater than the saturation fluence of the gain medium, and is given by:

$$n = n_0 + n_2 I \tag{A.1}$$

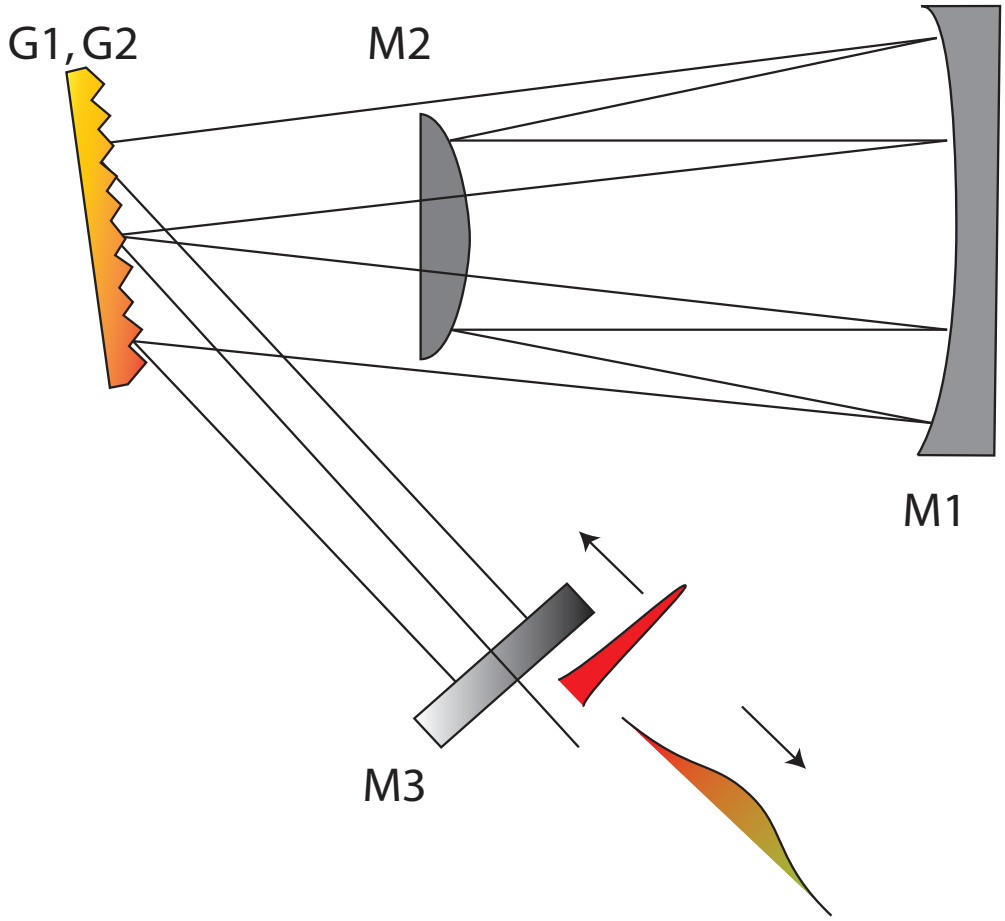

Figure A.1: Reflective Offner triplet, as used on Vulcan Petawatt, for pulse stretching

The saturation fluence for a given material is given by:

$$F_{sat} = \frac{\hbar\omega_L}{\phi} \tag{A.2}$$

where $\hbar$ is plancks constant, ω is the angular frequency of the laser and ϕ is the stimulated emission cross section of the material.

F_{sat} is equal to 4 J/cm^2 for Nd:glass amplifiers [127]. For a picosecond pulse this means a power density of 4×10^{12} Wcm^{-2}, above which the refractive index of the gain medium becomes non-linearly intensity dependent.

The spatial extent of the pulse is non uniform meaning that the contribution of the intensity dependent term refraction depends on the spatial intensity profile, distorting the wavefront of the beam in the process in what is known as B-Integral. In the case of a beam with a Gaussian spatial intensity profile this results in self-

focussing of the beam and damage to the optic [127]. The B-integral is given by:

$$B = \frac{2\pi}{\lambda} \int_0^L n_2 I dx \tag{A.3}$$

At this power density level, the intensity is great enough to induce ionisation that would result in damage of the optics. Therefore it is necessary to reduce the power density to prevent the build up of B integral and any chance of burning optics whilst extracting the maximum amount of energy from the gain medium. For short pulses, one such way of doing so is by employing the CPA technique. In order to keep the input intensity to a level that prevents damage to the optical system the pulse is stretched in time by a factor of $10^3 - 10^5$ taking the pulse from femtoseconds to nanoseconds in duration. Importantly by doing this the fluence is kept the same but the power density for amplification is reduced. The pulse is stretched by using a paired diffraction grating configuration to spectrally disperse the pulse in the time domain, therefore increasing the length of the pulse, known as chirping. The chirped pulse is of a lower intensity and can then be amplified by many orders of magnitude without risk of damage to optics. In figure A.1, one design of pulse stretcher is shown, known as a reflective Offner triplet. This is the design as employed on the Vulcan Petawatt system [128]. The pulse is incident on the grating and diffracted. The diffracted beam is reflected by a paired concave and convex mirror (M1 and M2) back onto the grating and diffracted to form a parallel beam [128, 129]. This is collected and reflected back onto the grating at a different height using a roof prism (M3) for a second pass through the grating system. The output beam after a second pass is then sent to the next amplification stage. Once the pulse has been amplified, it must be re-compressed to give a short pulse output. This is achieved by use of paired diffraction gratings matched to the stretcher with the exact opposite dispersion to deliver a pulse of width close to the original.

A.2.2 Amplified Spontaneous Emission (ASE)

Spontaneous emission is a process inherent to all lasing or gain media [129]. Minimising the degree of spontaneous emission and it's subsequent amplification is of key importance in the generation of intense laser pulses. This can be accomplished to a degree passively by implementation of pulse cleaning and amplification techniques in the laser chain itself or in the extreme case by employing a plasma optic in the final focussing beam just before target. In laser solid interactions, particularly with ultra thin targets, amplified spontaneous emission is seriously detrimental to the interaction due to it's inherently random nature. ASE manifests itself as a pedestal to the main laser pulse and can stretch temporally to many nanoseconds preceding the main intense laser pulse. With high intensity pulses of the order of 10^{21} Wcm^{-2} , with a pedestal intensity level $10^{6} - 10^{7}$ less than the main pulse, the ASE intensity is of the order of 10^{14} Wcm^{-2} and well above the threshold for ionisation of matter. In the case of a solid or dense plasma this results in target pre-expansion and introduces a plasma density gradient at the front surface of the target, and in the extreme case of ultra thin solids, the target can be destroyed completely before the arrival of the main pulse. The ratio of the ASE to main pulse peak intensity is what is known as the laser 'Intensity contrast', and is a critical parameter in laser solid interactions.

In a laser amplifier, the gain medium is first pumped causing the majority of electrons in the medium to transition to an excited state, known as population inversion. After a certain lifetime, if the emission is not stimulated, the electrons will fall to their ground state and emit photons of a wavelength characteristic of the transition energy, in all directions. Even when the emission is stimulated, over a time scale greater than the seed pulse, there will be a degree of spontaneous emission and this depends on the transition rate and the radiative lifetime of the medium. This can be calculated from the rate equation as:

$$R = \phi \frac{I}{hv} \tag{A.4}$$

where R is the transition rate, I is the intensity, ϕ is the transition cross

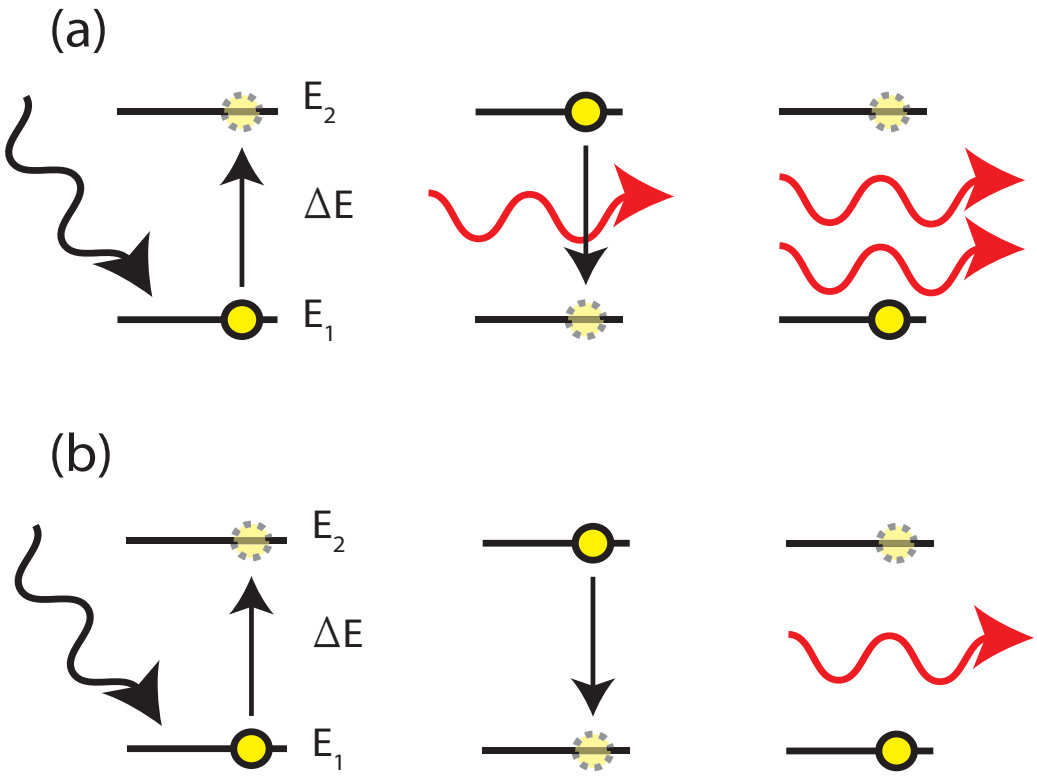

Figure A.2: Schematic showing the process of (a) excitation of an electron to an excited state and the stimulated emission from an incident photon, and (b) the spontaneous emission of a photon without stimulation by another photon. Photons that are spontaneously emitted can then be amplified by stimulating emission as in (a).

section of the gain medium and hv is the photon energy

Of the spontaneously emitted light, of particular interest is the light that is emitted in the direction of the propagating seed laser pulse [129]. The spontaneous emission that is co-directional with the stimulated emission will also act to stimulate further emission, resulting in amplification [129]. Both stimulated emission and spontaneous emission are shown schematically in figure A.2. Spontaneous emission as we have stated is inherent in all gain media. It is the amplification of the spontaneous emission that must be avoided, or at least minimised. Operation of the amplifier with a lower gain is just one way of reducing this. For a single pass through the gain this might seem counter intuitive as maximum amplification of the pulse is the aim. It is for this reason that multi-pass and regenerative amplification techniques are used as they enable multiple passes through the gain medium, extracting energy each time. One way to clean the

pulse is to use a pockels cell to gate out the ASE pedestal on the nanosecond time scale. However due to the electro-optical switching, gating on timescales less than this is not possible and measures must be taken to minimise ASE from an early stage in the laser system. One such way to minimise the level of ASE at an early stage is to utilise optical parametric amplification in the pre-amplifier stages of the laser chain [2] (rather than a regenerative or multi-pass amplifier). As parametric amplification is not achieved through population inversion in a conventional gain medium, spontaneous emission is not inherent in the process. In this way the pulse can be amplified without seeding significant ASE until the main amplification stage, resulting in enhanced laser contrast. The need for high contrast has driven the development of OPA in high power laser systems and will be discussed in greater detail in section A.2.4.

A.2.3 Amplification

Once the initial seed pulse has been chirped a common method of amplification used is regenerative amplification. Regenerative amplifiers are typically used in the oscillator or pre-amplification stages with gain achieved on each pass through the gain medium. As discussed in the previous section (A.2.2), in media where the gain is high, this can act to amplify spontaneous emission as well as stimulated. Having a lower gain, in other words pumping the gain medium less, but instead making many passes of the seed pulse through it, can help to reduce both the spontaneous emission and it's amplification.

In this example, an initial pulse is injected into the optical cavity and passes through the gain medium multiple times whilst extracting energy from the population inversion with each consecutive pass. As seen in figure A.3, if a pulse enters the cavity with a linear polarisation and no voltage applied to the pockels cell, after a single round trip it will be ejected from the cavity. If a voltage is applied to the pockels cell that allows it to behave in $\lambda/4$ wave function, which after reflection from the cavity mirror, a second pass reverses the polarisation such that it will be transmitted by the thin film polariser and be amplified with each pass of the gain medium.

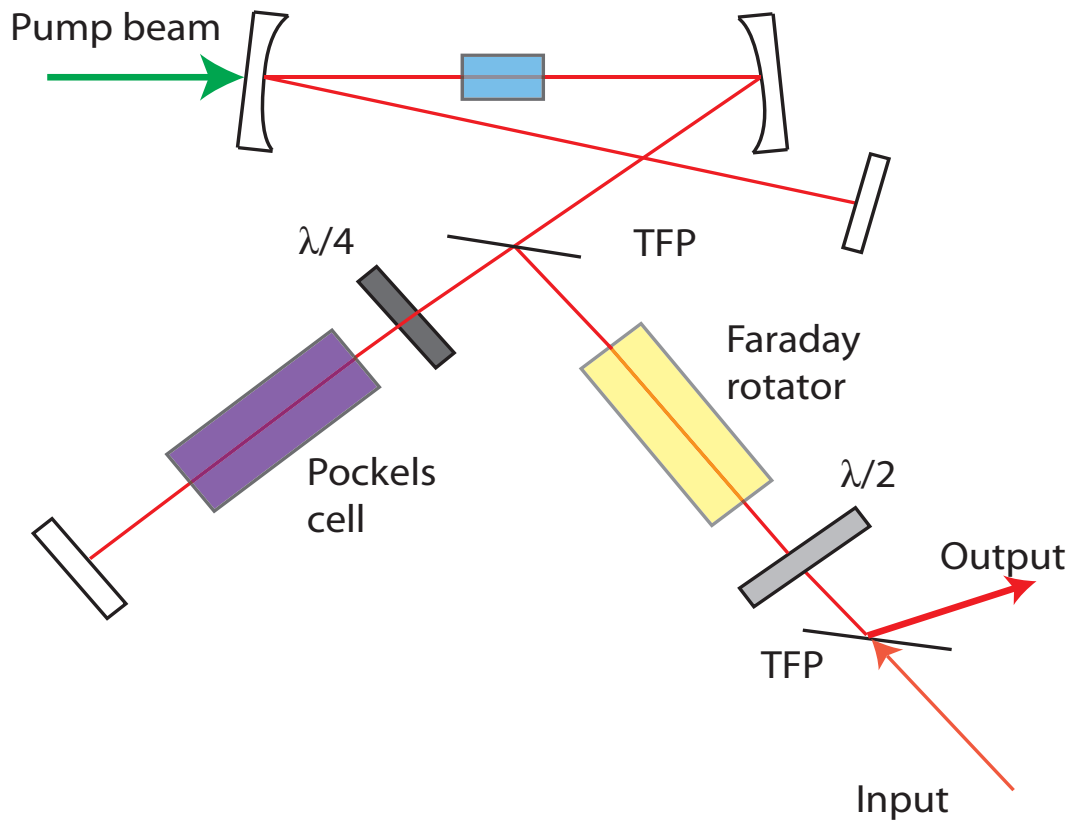

Figure A.3: Regenerative amplifier setup

Once the pulse has made the necessary number of passes through the gain medium to achieve the desired amplification, the pockels cell can apply a second $\lambda/4$ to the pulse which after the double pass rotates to the original polarisation and is reflected out of the cavity. The faraday rotator then acts as an optical switch changing the polarisation to the condition for reflection from the TFP and onto the next stage in the laser system, separating the input and output. In this way the output coupler of the optical cavity is the pockels cell that controls the polarisation and can be changed depending on the desired level of amplification by control of the number of passes.

Another amplifying technique commonly used is the multi-pass amplifier. In this arrangement, as with the regenerative amplifier, the pulse makes multiple passes through the gain medium but this time by purely geometrical means as opposed to by optically switching out of a cavity. The pulse is passed multiple times through the gain medium of a series of mirrors as illustrated in A.4. Due

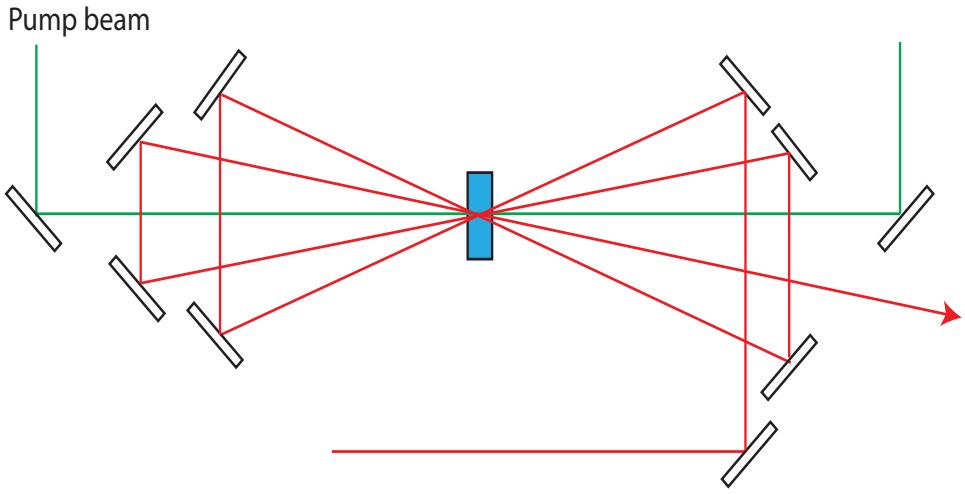

Figure A.4: Multipass amplifier setup

to the fact the gain medium is not within an optical cavity, larger gains can be achieved per pass of the pulse.

Both of these techniques are commonly implemented in CPA lasers, however as the highest gain is typically achieved in the pre-amplification stages of the laser system and due to the nature of the amplification and the inherent ASE in these types of amplifiers, for high contrast pulses it is necessary to look at other amplification techniques such as parametric amplification.

A.2.4 Optical parametric amplification

Optical parametric amplification is a different type of amplification typically used in high power laser systems and has many advantages over conventional amplifying media [130]. Non-linear crystals that exhibit χ^2 non-linearity [129] are used in the parametric transfer of energy between a weaker and stronger pulse, the signal and pump, within the crystal known as optical parametric amplification. One of the key advantages of OPA is the high quality and contrast of the amplified pulses as well as the high efficiency conversion of the pump pulse which consequently means there is very little thermal energy deposited into the medium. Due to the nature of the amplification ASE, which is inherent in normal amplification media such as glass amplifiers, is eliminated. Optical parametric amplifiers are typically

used in the pre-amplification stages of large scale facilities to amplify the seed pulse from the oscillator, from the nano-joule to the milli-joule level, to provide a high quality pulse for amplification in the glass amplifying chain.

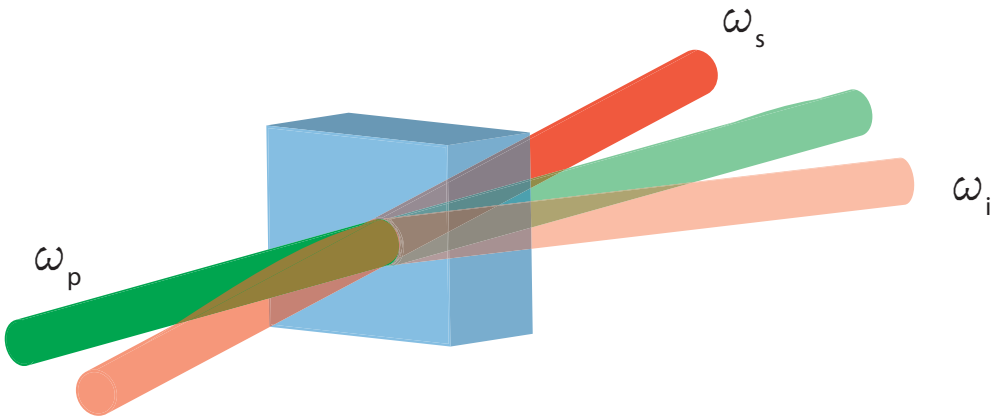

Figure A.5: Optical parametric amplification in a non-linear crystal

In an OPA, a low energy signal pulse is passed through the nonlinear crystal in the presence of a high energy and higher frequency pump pulse. In the crystal, under the correct phase matching condition, the pump pulse is converted to the same frequency, ω_p, as the signal pulse, ω_s, as well as a third pulse with a frequency, ω_i, equal to that of the difference between the pump and signal.

$$\omega_p = \omega_s + \omega_i \tag{A.5}$$

It is due to this fact that the pump pulse is converted almost totally into the signal and idler that there is very little heating of the crystal itself. There are a number of advantages that OPA's provide over conventional amplification media. One is that unlike laser amplifiers no energy is stored within the medium itself and amplification only occurs in the presence of both the signal and pump pulse meaning that a very high contrast pulse is obtained, minimising problems such as ASE. This is one of the main reasons that OPCPA is utilised to significant effect in the pre-amplification of pulses for high power laser systems. Another advantage of this method of amplification is that it can support amplification over large bandwidth pulses and does not suffer from gain narrowing [2, 128].

A.2.5 Plasma mirror

Although steps have been taken to minimise the effect of ASE, it is a process that cannot be eliminated completely, and although it's contribution may be $10^6 - 10^7$ less than the main pulse intensity, when focussed onto a target with an intensity of 10^{20} Wcm^{-2} the pedestal of the pulse is still sufficient to cause ionisation and expansion of the target. The presence of ASE or pre-pulses cannot be fully characterised for every shot, and so it introduces a degree of uncertainty in the target conditions for the main pulse interaction.

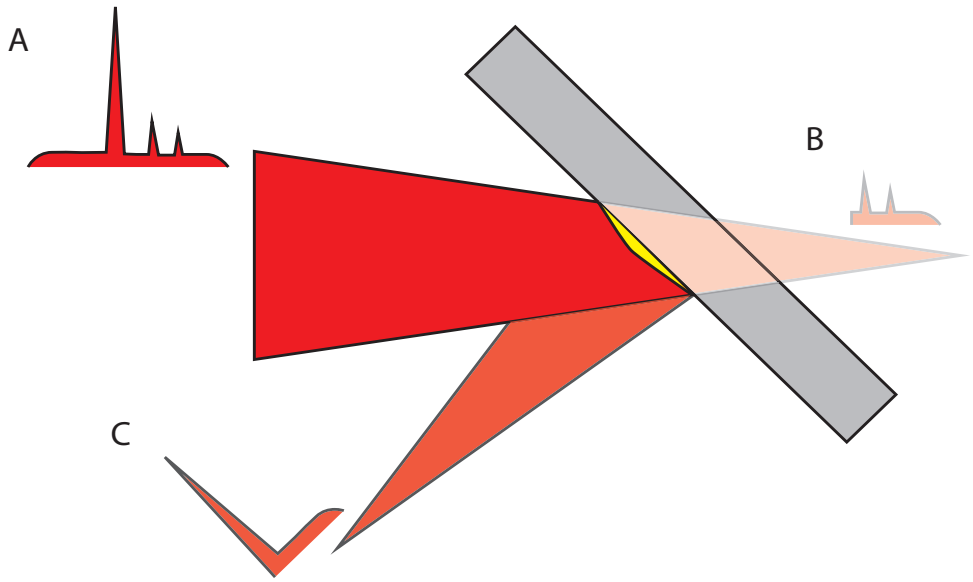

Figure A.6: Schematic of intense laser pulse incident on a plasma mirror, showing transmission of low intensity pedestal and reflection of the main intense laser pulse

One way to minimise this effect is to implement a plasma mirror within the main focusing beam. The plasma mirror is essentially a slab of anti-reflection coated glass that acts as an 'intensity shutter', transmitting the low intensity pedestal and pre-pulses and reflecting the high intensity main pulse [131, 132]. This acts to transmit the low intensity portion of the pulse occurs, as the intensity is below the threshold for ionisation of the glass. However on the rising edge of the main pulse the intensity increases sharply to above the ionisation threshold, forming a plasma that quickly increases the reflectivity and effectively switches on the mirror such that the main pulse is reflected. In this way the intensity contrast

between the pedestal and the main pulse can be improved by $10^2 - 10^3$ [131] on the tens of picosecond time scale. The position of the plasma mirror is optimised such that both the intensity of the main pulse corresponds to a maximum in the reflectivity and also that the pedestal and any pre-pulses are below the ionisation threshold. For a 500fs pulse this equates to a maximum intensity of 3×10^{15} Wcm^{-2} as shown by Dromey *et al* [131] and Ziener *et al* [3]. As a consequence of the plasma formation and subsequent reflection from the plasma surface, some of the initial pulse energy is lost in the interaction although a typical reflectivity of the order of 60-80% is achievable.

A.3 High Power Lasers

In the process of my PhD project, experimental experience was gained on a number of laser systems, from short pulse femtosecond systems such as the Astra Gemini to picosecond systems like Vulcan Petawatt. Although both lasers can achieve peak intensities up to 10^{21} Wcm^{-2}, the energy contained in each pulse is much different. With this in mind, each system lends itself to the probing of various processes depending on the sensitivity to the rising edge profile of the laser and interaction time. The results presented in the following chapters were obtained on the Petawatt arm of the Vulcan laser system, which will be discussed more rigorously below.

A.3.1 Vulcan Petawatt

The Vulcan laser system delivers pulses to two target areas, Target Area West (TAW), and Target Area Petawatt (TAP). In the case of the latter, the laser is sent to another final stage of amplification bringing it to the nominal level of 1PW. Target Area Petawatt can receive two beams, a short pulse PW beam, with 600 J energy delivered in a pulse length of 0.8 ps, as well as a long pulse beam of pulse length 0.5-8 ns and 50-300 J dependent on operating pulse length. The Vulcan laser begins with a Ti:Sa oscillator providing $\sim$120 fs pulses of 5 nJ operating at 1055 nm, as a seed pulse. The seed pulse is stretched to 3 ps

and undergoes pre-amplification in a ps-OPCPA stage [2]. The pulse is amplified from ∼5 nJ to ∼70 μJ level at this stage of pre-amplification. It is after this point that, if in use, the double pulsing system is introduced. The dual pulser will be discussed in more depth in the next section. The picosecond stretched pulse then undergoes further stretching to 4.5 ns for further pre-amplification in a nanosecond OPCPA chain consisting of 3 stages that take the pulse energy to the ∼10 mJ level [133].

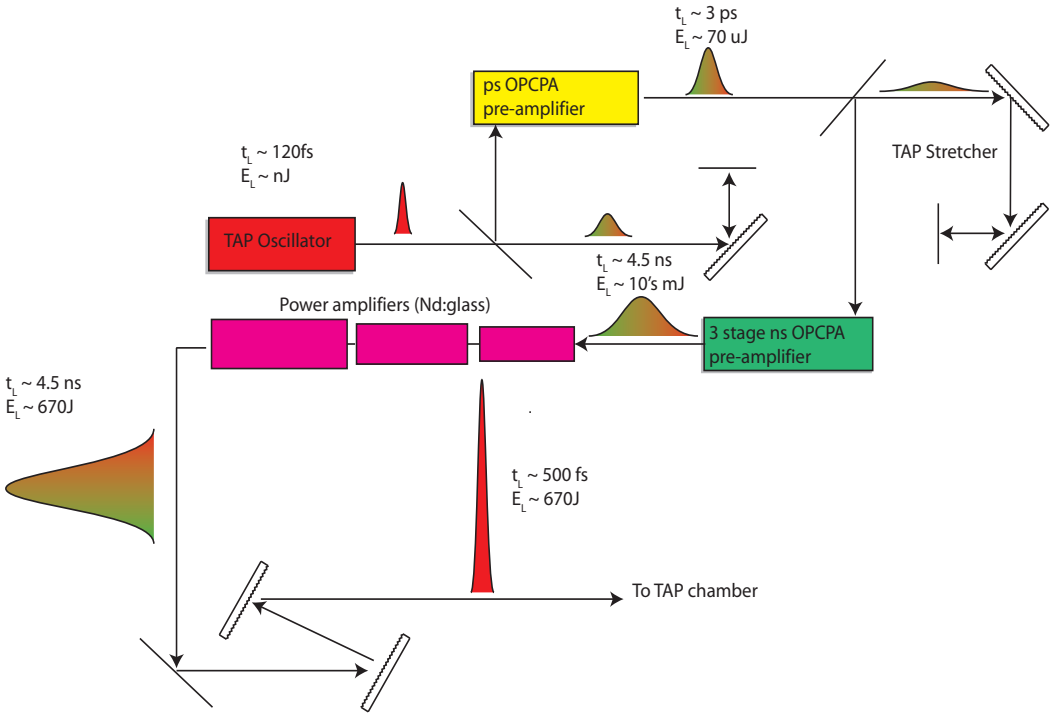

Figure A.7: Schematic of Vulcan laser system and amplification chain

The beam is then injected into the rod and disc amplification chain, known as the 'power' amplifiers. These consist of flash lamp pumped Nd:glass rods to increase the pulse energy to Joule level and Nd:glass discs, of continuously increasing diameter (100, 150 and 208 mm) to cope with the increased energy fluence and prevent damage, to take the final pulse energy up to 670 J.

After amplification the beam is expanded in a vacuum spatial filter to 600 mm diameter to reduce the energy fluence and simultaneously improve the beam quality, and relayed to the compressor [128]. The compressor itself re-compresses the pulse from 4.5 ns to approximately 500 fs using two gold coated gratings of 1480

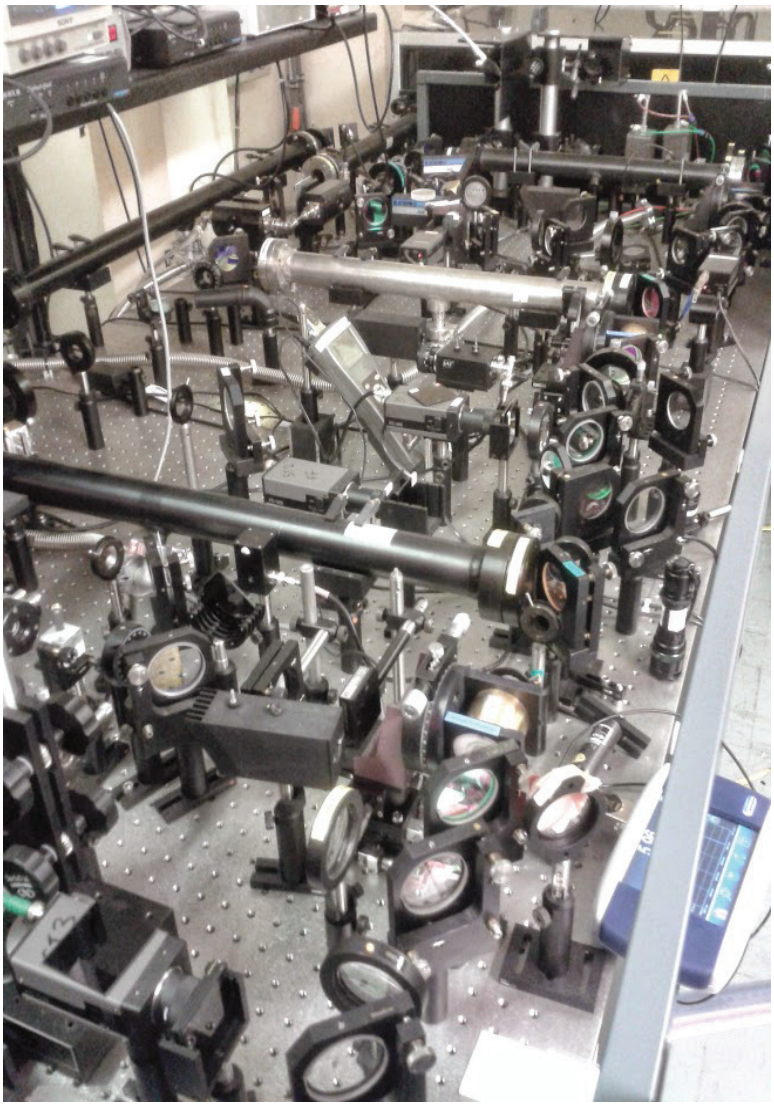

Figure A.8: Three stage nano-second OPCPA system used on the petawatt beam line

lines/mm and separated by 13 m before being sent to the target chamber and the final focussing optic by two 1 m diameter dielectric mirrors. The final focussing optic, a 600 mm diameter f/3.1 off-axis parabola, focusses the full aperture beam to a diffraction limited spot of ∼5 microns.

A.3.2 Vulcan Petawatt in dual pulse mode

The Vulcan laser system provides a unique platform to deliver user tailored pulse conditions in the probing of intense laser plasma interactions. One such mode that the Vulcan laser can operate in is to provide dual intense laser pulses that are of interest in the acceleration of fast ions. This system of dual intense laser

pulses has been employed previously in the context of ion acceleration in the Target Normal Sheath Acceleration regime [92, 93], where the first pulse initiates the acceleration and the second pulse provides a secondary drive to the ions by inducing a further current of fast electrons, resulting in enhancement of the sheath field and thus ion energy.

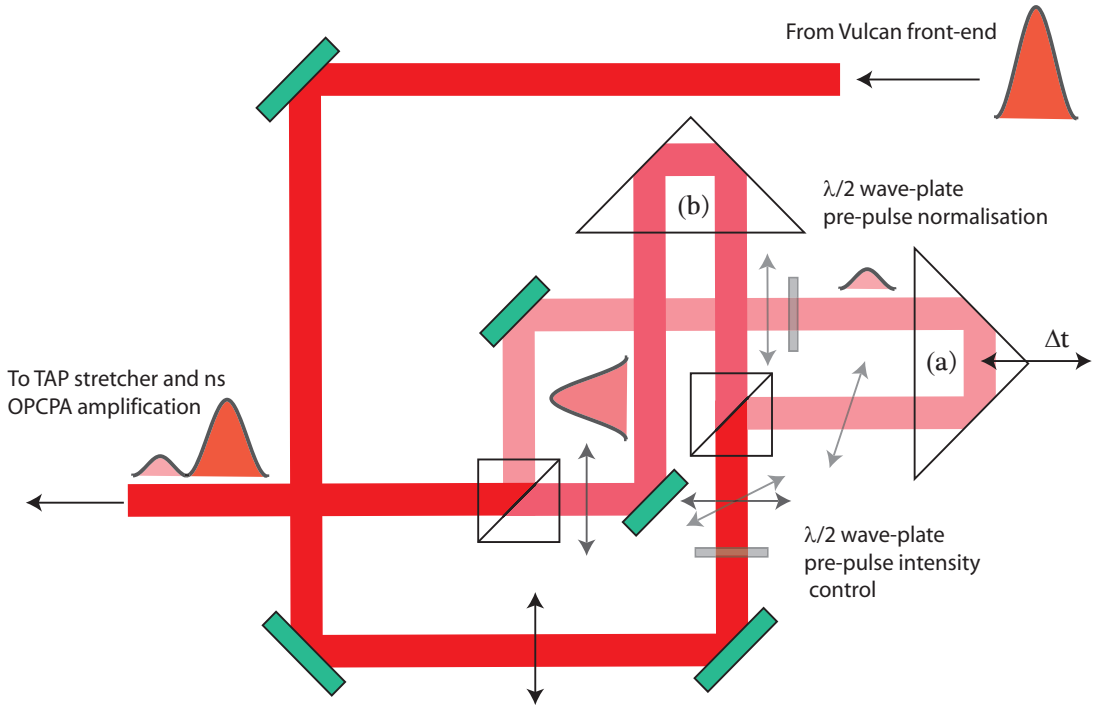

Figure A.9: Schematic of TAP double pulser

Unlike the scheme described above where a relatively thick target of the order of 10-100's microns are studied and the dual pulse provides an additional fast electron source, in the study of ultra-thin targets in the 10's of nanometers the addition of a controlled pre pulse can be utilised to pre-expand the target to near critical densities for the interaction of the main intense pulse, opening up the possibility to study mechanisms of ion acceleration predicted in this regime. The method of dual pulsing is achieved by first splitting the laser pulse into two separate pulses and applying a temporal separation as defined by the requirements of the user.

The initial oscillator pulse from the Vulcan TAP front end provides a train of 100 fs pulses of which one is selected and passes to the stretcher and amplification

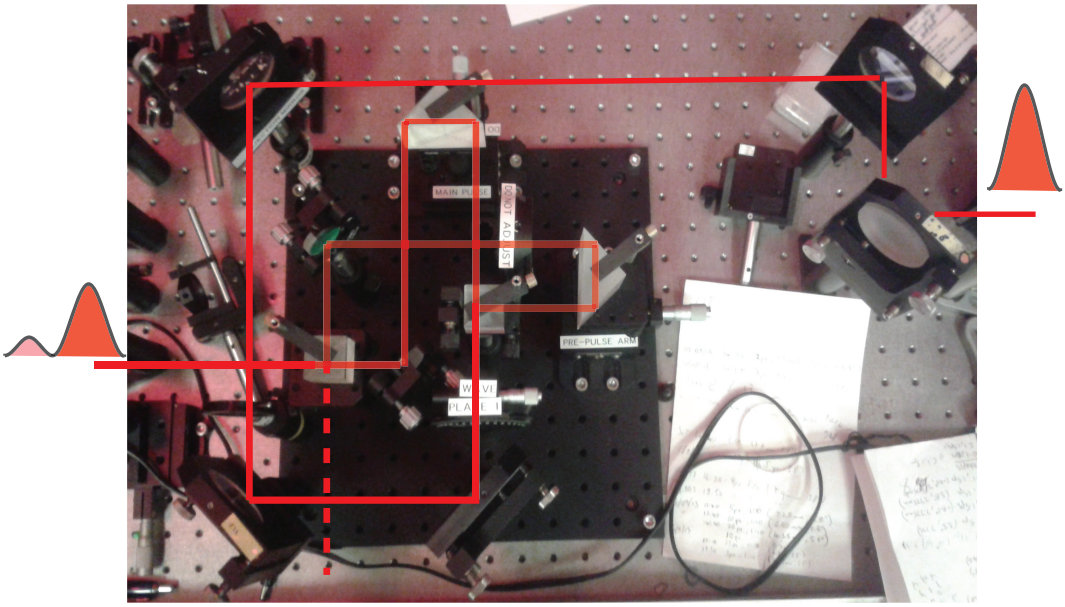

Figure A.10: Experimental setup of the TAP double pulser

chain as illustrated in figure A.7. The set up of the dual pulser is inserted at this point, after the oscillator and before the stretcher, enabling the minimisation of the error in temporal separation and recovery of lost pulse energy by use of the ns OPCPA stage the reason for which will be explained in further detail. The dual pulsing set-up consists of an interferometer coupled with polariser and polarising beam splitter to give relative amplitude control of the two pulses. There are two arms to the double pulser, both with independent path length control. A polariser is used to set the polarisation of the seed pulse before a polarising beam splitter, where the transmittance and polarising angle are characterised, and a fraction is reflected to the pre-pulse arm. The reflected component of the beam will have a polarisation determined by the rotation of the half wave plate. After the delay slide the polarisation is rotated to its initial orientation with second wave plate of opposite angle, such that the same polarisation is maintained for both the pre-pulse and main pulse. A roof prism on a translation stage enables temporal control via alteration of the relative path differences between the two pulses before recombination via a non polarising beam splitter. The system itself is fairly high loss with only ~40% throughput of the initial pulse energy, however the output from the ps-OPCPA provides sufficient gain to overcome this without

adversely affecting the TAP operation.

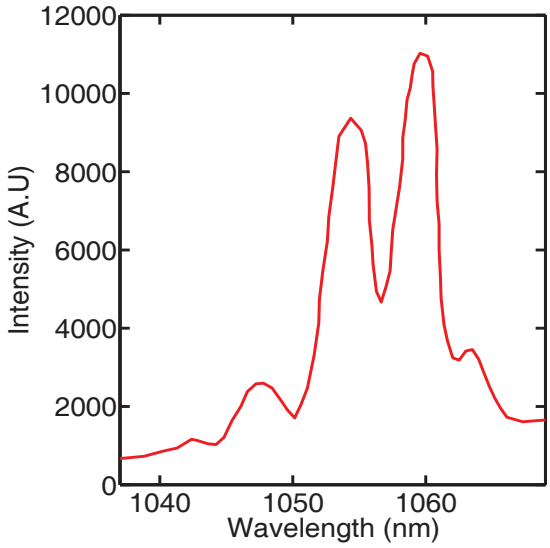

Figure A.11: Modulation of spectrum during double pulser alignment, when both arms are spatially and temporally overlapped, setting the zero delay point.

The two pulse arms are set to equal path lengths, with the beam transmitted through the PBS being the main pulse and the reflected the pre-pulse passing through the delay stage. Temporal and spatial overlap of the pulses must first be achieved before the path difference is introduced to define temporal pulse separation. Spatial overlapping of the beams is achieved by adjustment of the two final turning mirrors to align with the stretcher, using the near and far field diagnostics. Temporal overlap of the pulses is achieved by introduction of a tilt to the beam that introduces fringes to the near field only when the two beams are overlapped both spatially and temporally, enabling the zero delay position to be defined. Another manifestation of temporal overlap is the observation of diffraction in the spectrum, which due to the broadband nature of the Ti:Sapphire oscillator is possible.

This is one of the key issues with the system as is currently employed as at this stage half of the beam energy from both components is transmitted or reflected resulting in a dual seed pulse, although the intensity ratio between them is as required the total pulse energy of the combination is half. This can be recovered however after the pulse stretching within the 3 stage nanosecond OPA system.

A.4 Plasma Diagnostics

Until this point, the technology needed to get to the point of interaction itself has been discussed. The following section will describe some of the methods and diagnostics implemented in the probing of the interaction itself and enables us to underpin the physical processes that take place. The interaction of an intense laser pulse with a solid is highly complex and there are a multitude of competing processes that must simultaneously be considered. This requires a large suite of diagnostic techniques working together with the goal to better understand the physical processes taking place. There are a number of techniques employed in a typical experimental set-up measuring discrete properties of the interaction. Firstly there are fast ion diagnostics to measure both the spatial extent of the beam and the spectral properties.

A.4.1 Thomson Parabola ion spectrometer

Of particular interest in the context of this work is the measurement of the fast ion population and in particular the spectral dynamics of the different species as this can tell us about the interplay between the species and the dynamics of the acceleration of these particles. The Thomson parabola has the benefit of being able to separate out the different charge states and spectrally resolve them [134]. The Thomson parabola itself is a fairly simple diagnostic consisting of a pinhole, to select a solid angle to be sampled, a solid state magnet, to energy resolve the particles, an electric field, to separate out the ions by charge state, and a detector to detect the ions. A typical Thomson parabola set-up as used on TAP is shown in figure A.12.

The ions will be deflected in the magnetic and electric fields, the magnitude of which will be dependent on their incident energy and their charge to mass ratio. The deflection at the imaging plane, assuming uniform fields along the length of both the magnet and the electric field plate and neglecting the fringe fields, can be calculated by the following, where D_B is the deflection due to the B field and

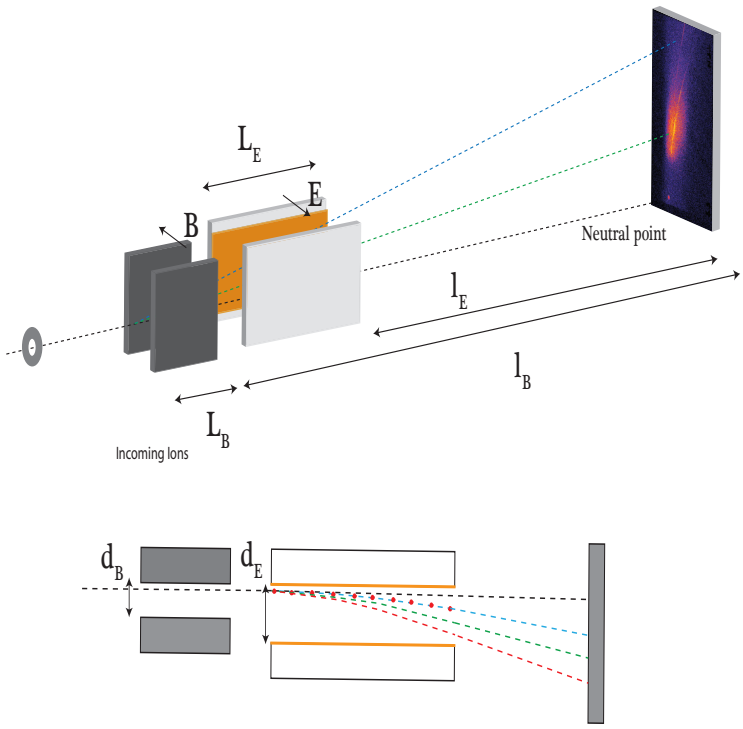

Figure A.12: Schematic of Thomson parabola and the trajectories the ions will take due to deflection in the magnetic and electric fields

D_E is the deflection due to the E field:

$$D_B = \frac{qBL_B}{m_i v_z}(\frac{1}{2}L_B + l_B) \tag{A.6}$$

$$D_E = \frac{qBL_E}{m_i v_z^2}(\frac{1}{2}L_E + l_E) \tag{A.7}$$

where L_B and L_E are the length of the magnet and electric field plates, l_B and l_E are the drift distances from the magnetic and electric fields respectively, B and E are the magnetic and electric field strengths, m_i is the ion mass and v_z the ion velocity. As can be seen, towards higher energies, the tracks begin to come closer together and merge. The maximum energy resolution is set by the alue at which it is no longer possible to distinguish species by q/m due to merging of the tracks. The maximum energy and charge-to-mass resolution can be increased in a number of ways. Firstly by applying a larger electric field to the field plates. As this increases however, the likelihood of discharge between the plates increases.

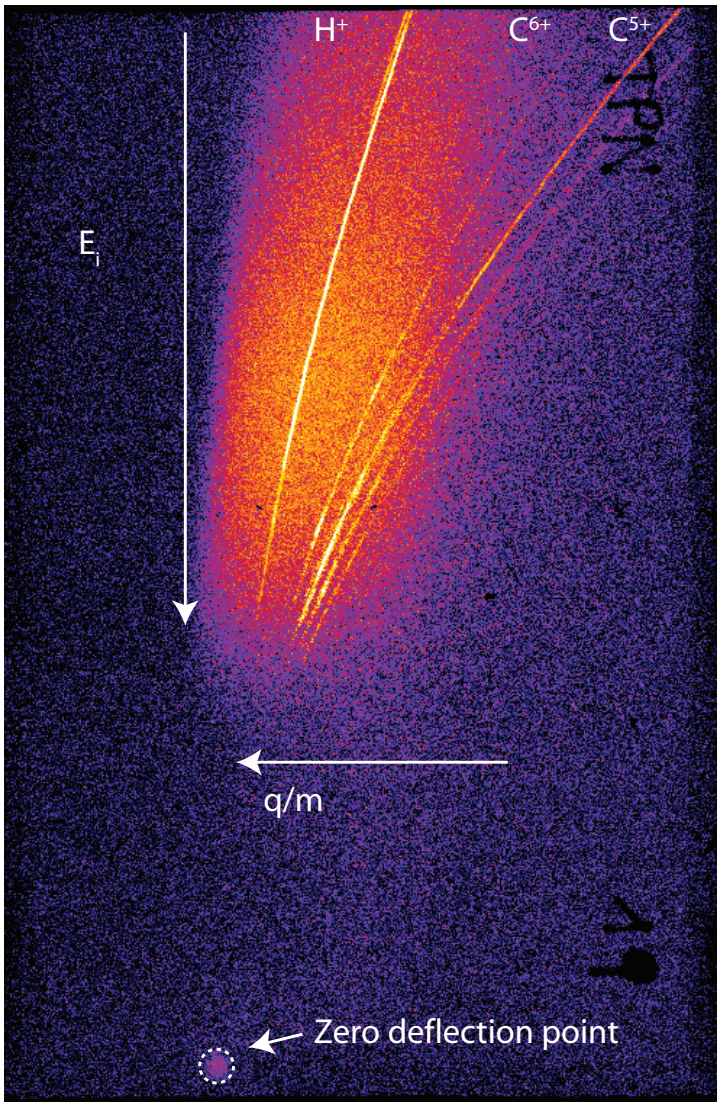

Figure A.13: Raw experimental data from Fujifilm imaging plate detector showing dispersed ions from TP spectrometer and zero deflection point

Another option is to increase the length of the plates so that the ions feel the effect of the field over a longer distance, though this has the problem that the most deflected ions (lowest energy) begin colliding with the plates. Carroll *et al* [135] presented a novel solution to this by simply angling one of the field plates. The third option to consider is simply to increase the drift distance between the field plates and detector and by geometrical projection the resolution will enhance both in terms of charge-to-mass ratio and energy. To keep the same energy resolution window, ie E_{min} - E_{max} the detector size must be increased accordingly. There are number of detection techniques that may be employed with Thomson parabolas (TP), each with their own merits and corresponding drawbacks and

will be discussed further. The results presented in chapter 4 were obtained using a high dispersion TP [136] to enable the measurement and dispersion of high energy ions of the order of 10's-100 MeV/u. To achieve this, a number of the parameters were changed to facilitate these requirements. Firstly the magnetic field was increased to B=1T, almost the limit of conventional permanent magnets, the electric field increased to E=200 Vm^{-1}, and the drift distance, l_B and l_E, increased. In this way, the high energy resolution cut off was increased. However this is at the sacrifice of the low energy end of the ion spectra, due to the fixed detector dimensions.

A.4.2 Imaging plate

Figure A.13 shows an example use of imaging plate as a detector for ions in a Thomson parabola spectrometer. Imaging plate is a reusable detector developed by Fujifilm that is sensitive to a range of ionising radiation and is used in the laboratory for detection of high energy x-rays, electrons and ions. It is widely used in the field of medicine, in particular for X-ray radiography [137], and has the advantage over conventional x-ray film of being quick to read and obtain data as well as being reusable. The active component of the image plate is the phosphor, crystalline BaFBr:Eu^{2+} with grain size of approximately 5 μm, coated onto a support layer.

Imaging plate works by absorbing the energy of incident radiation and exciting electrons in the active material into a metastable state, in this case Europium. The electron is trapped in a metastable state within a colour-centre in the phosphor. To extract the information embedded in the metastable state, the image plate is developed by photo-stimulating the emission using a scanning laser typically in the visible with $\lambda = 632$ nm. The photo-stimulated luminescence of the crystal is of $\lambda = 390$ nm [137], and this is detected by a photomultiplier tube.

Once scanned, the data can be erased from the plate by exposure to a white light source ready for re-use. The crystalline structure of the phosphor as stated previously is of the order of 5 μm, setting the lower bound of spatial resolution. However the scanning laser used for PSL typically sets the minimum spatial res-

olution based on the minimum focal spot that can be achieved. This typically gives a spatial resolution of 25 μm. Image plate is the detector of choice for a number of diagnostics including X-ray spectrometers, electron spectrometer and as shown in the previous section TP spectrometers. Careful calibration of the response of the image plate to different types of ionising radiation as a function of energy is important in determination of the flux of particles and can be achieved by using a calibrated source. A number of methods can be used, in particular for calibration as an ion detector for TP spectrometers,. One commonly used technique is to use slotted CR39, a nuclear track detector which enables absolute flux calibration measurements [138]. Absolute calibration measurements for different types of image plate have also been made for protons in the energy range 0.5-20MeV [139].

A.4.3 Radiochromic film

Unlike the TP which only samples a small solid angle of the interaction and spectrally resolves the ion species according to their q/m ratio, radiochromic film enables the measurement of the spatial characteristics of ion beam [140, 141]. Radiochromic film is a dosimetric film normally containing an active layer, a radiation sensitive dye, and a plastic backing and protective layer. Typically in high power laser plasma experiments, GAFCHROMIC HD-V2, or EBT2 is used.

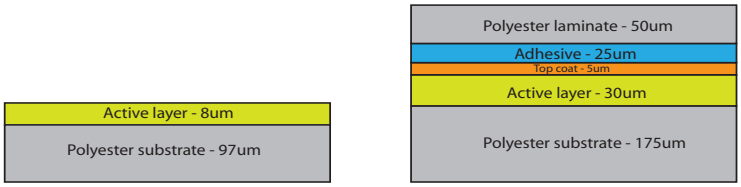

Figure A.14: Composition of GAFCHROMIC a) HD-V2 and b) EBT2 film as used in dosimetry stacks

Upon exposure, the film is self developing making it an extremely easy to use and versatile diagnostic enabling instantaneous measurement (though the film continues to develop fully over a period of 24 hours) of the experimental conditions. Principally, HD-V2 is used for proton measurements and consists

of an 8 μm-thick active layer backed by a 97 μm-thick polyester substrate, the composition is illustrated in A.14. The film is sensitive to doses between 10-1000 Gy and has a spatial resolution of 5 μm. However in real terms the spatial resolution is set by the device used to scan the film, which typically gives a resolution of the order of $\sim$40 μm.

By stacking multiple layers of RCF, the spatial profile can be energy resolved at discreet intervals due to the unique stopping characteristics of ions in matter, illustrated in A.15(a). The RCF itself consists of a front aluminium foil layer, to stop heavy ions and prevent exposure of the RCF to any transmitted laser light. The RCF is typically stacked with aluminium or copper filters of a selected thickness to sample the spatial profile of the beam at discreet energy intervals.

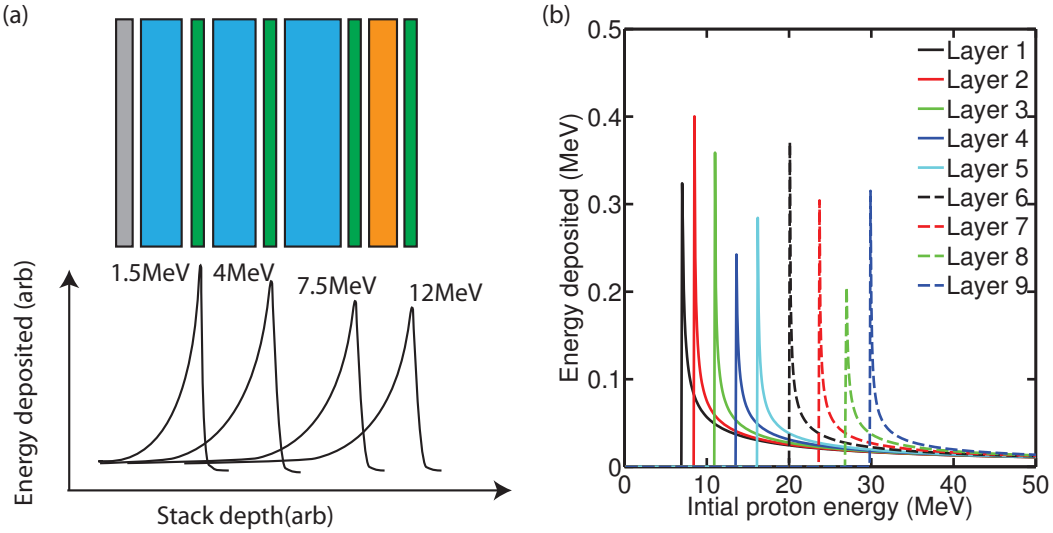

Figure A.15: (a)Energy deposition as a function of material depth (b) Response curves showing energy deposition in each stack layer as a function of proton energy

The thickness of the filters can be adjusted to tailor the energy sampled by RCF layer in the spectral region of particular interest. The filtering used in the stacks serves a dual purpose. By using copper as a filter material, the activating properties due to the protons, enable verification of beam profile or particle flux measured on the RCF and can be made by either contact radiography or activation measurements of the copper [142]. Due to the Bragg peak stopping of ions in matter, a calculation of the energy deposited in the active layer for a given ion energy can be made using SRIM (**S**topping **R**anges of **I**ons in **M**atter), a

software package which calculates the stopping and range of ions in matter [143]. In this way, using the data for ion stopping, the energy deposited in the active layer for a range of ion energies can be calculated, which when coupled with the film response to dose, enables a response curve to be generated for a given design of stack. An example response curve for a stack design used on a recent experimental is shown in A.15(b). This enables the flux for each stack layer to be determined and a coarse proton energy spectrum to be extracted.

A.4.4 Laser transmission diagnostics

In the study of ultra-thin foil interactions, measurement of the transmitted laser light is of key importance as often these targets will become relativistically transparent, particularly in the thinnest of targets of the order of tens of nanometres. By quantifying the degree of transmitted light, an estimate of the level of transparency can be obtained and is invaluable in pinning down the contribution this plays in the acceleration of fast ions.

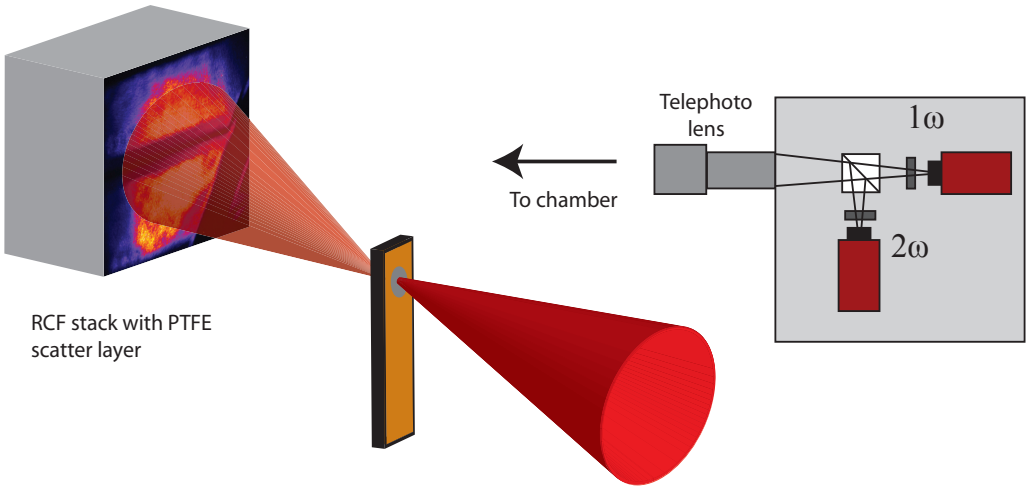

Figure A.16: Transmission imaging setup of scatter screen on front of the RCF stack. A telephoto lens images the stack with beam splitter separate into two channels and filters for transmission of 1ω and 2ω to two independent CCD cameras.

The degree of transmitted laser light is captured on a $\sim$400 μm PTFE scatter screen that is inserted into the front of the RCF stack that is located 75 mm behind the rear of the target. This enables the full aperture of the f/3 re-expanding

beam to be captured within the scattering material. The scattered light from the transmitted beam is then imaged in both fundamental and 2nd harmonic from out-with the interaction chamber, looking through a window using a large aperture mirror, avoiding direct line of sight to TCC. The primary reason for this is to protect the CCD cameras from the EM pulse inherent with petawatt laser solid interactions. The imaging system itself consists of a telephoto lens coupled with a beam splitter and two CCD cameras. This common imaging system ensures that the images are both identical. Narrowband filters centred around the laser fundamental and second harmonic wavelength enable imaging of the spatial intensity profile of the transmitted light at both wavelengths to be obtained simultaneously.

A.4.5 Transverse optical probing

Transverse optical probing of laser produced plasmas is a commonly employed diagnostic technique that enables a measurement, of the dynamics of the interaction. In a probe line there are typically two techniques used, shadowgraphy and interferometry. By introducing a beam splitter in the imaging system these can be split into two separate channels with CCD camera detectors. Shadowgraphy simply gives a backlit image of the overdense plasma expansion and is often a quick method of diagnosing the expanding plasma. This measurement coupled with modelling of the plasma expansion by ASE can be used to estimate the level of ASE present prior to the main pulse arrival.

Interferometry can then be used to make detailed measurements of the electron density in the expanding plasma due to the refractive index differences from varying electron densities and the optical path difference that light takes within the plasma. Experimentally, a pick-off from the main CPA beam line is taken before the target. The beam is frequency doubled, enabling probing of plasma to higher densities according to the increase in critical density for shorter wavelength light. A half wave plate is used to rotate the polarisation to 45 degrees, giving an equal S and P component, before going to a timing slide. The timing slide enables the relative timing of the probe beam with respect to the main beam at

the interaction point to be set. The timing slide simply consists of two 45 degree mirrors mounted on a translation stage and is used to add or remove path length to the probe beam line. Adjustment of the relative path length between the probe and main beams enables probing of the target expansion at different temporal steps with respect to the main pulse. The probe beam is passed transversely across the surface of the target, after which a lens images outside of the chamber.

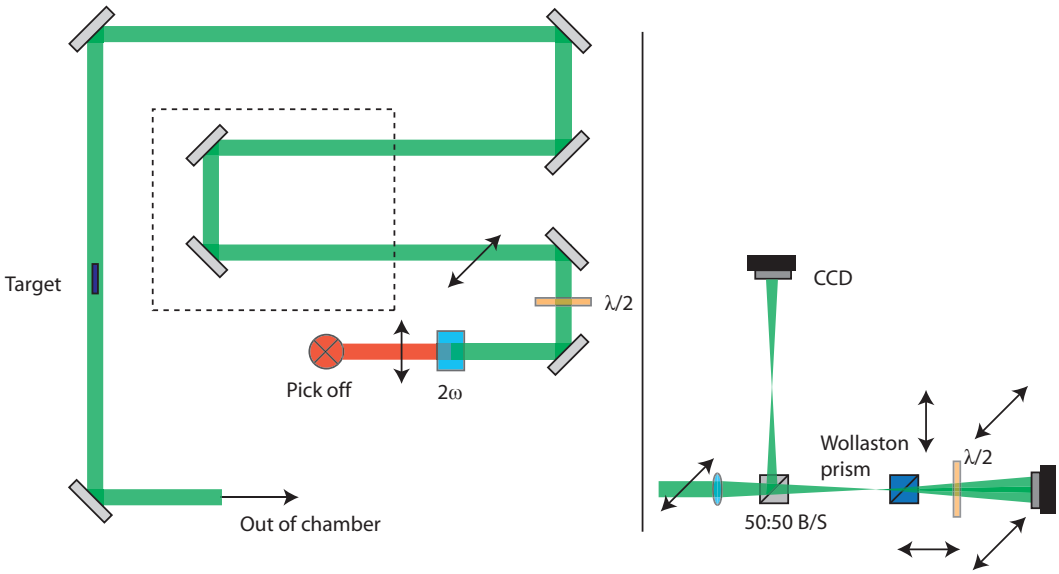

Figure A.17: Probe and interferometer setup. A pick-off is taken from the main beam via a periscope and the beam frequency doubled. The polarisation is rotated by a $\lambda/2$ wave plate before being passed transverse over the target surface and relayed out of the chamber. The beam is split by a beam splitting cube and focussed onto two separate CCD cameras. On one, a Wollaston prism separates the polarisation components before second $\lambda/2$ wave plate.

At the focal distance of the first lens, L_1, the beam is re-imaged by a second lens, L_2, before a beam splitter separates it into two channels, one imaged onto a CCD camera for shadowgraphy and one to the interferometer setup onto another CCD camera. The interferometer consists of a Wollaston prism that acts to spatially separate the orthogonal polarisation components of the beam [144] and a second polariser at 45 degrees returns the polarisation to the original state. This results in a interference pattern where the two images overlap on the CCD. One advantage of this setup of the interferometer is that the path length of the two components is the same resulting in a stable setup [145]. For a prism at distance,

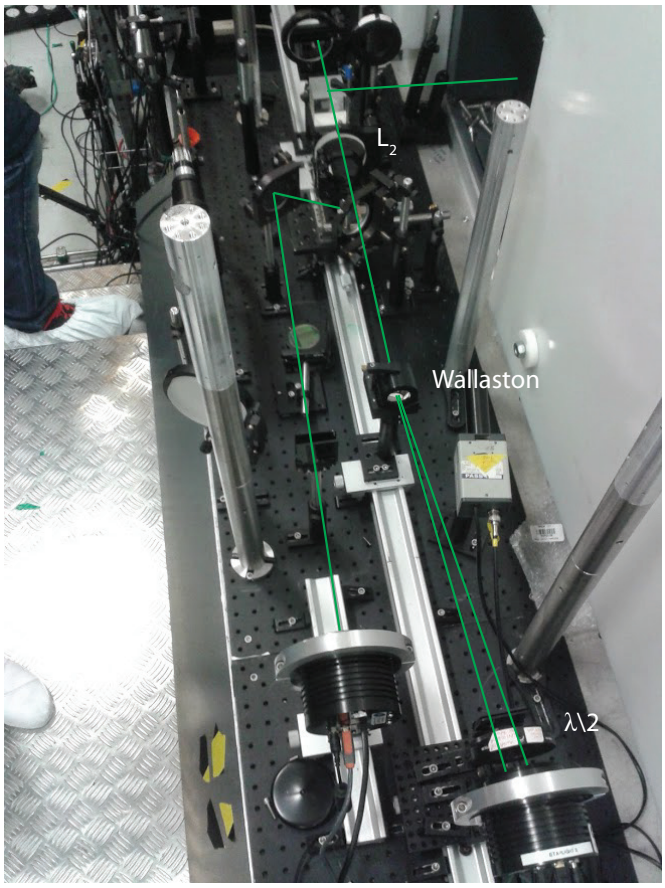

Figure A.18: Experimental arrangement of final shadowgraphy and interferometery setup

p, from the lens focus, p' from imaging plane, with a divergence angle θ the fringe separation at the imaging plane can be calculated for a given wavelength [145] as:

$$i = \frac{\lambda}{\theta}\frac{p'}{p} \tag{A.8}$$

where p' is the distance from the focus of the first lens to the Wollaston prism, p is the distance from the Wollaston to the imaging plane at the detector and θ is the divergence angle of the Wollaston prism.

As explained in chapter 2, the refractive index of a plasma is dependent on the electron density, therefore a plasma density gradient will have a corresponding refractive index gradient. Light travelling through this gradient will then have a different path length dependent on the electron density. This effect manifests in a shift of the interference fringes in the presence of plasma. Assuming cylindrical

symmetry around the axis of the laser, Abel inversion can be applied to extract the electron density map [145].

A.5 Numerical simulation

In the previous sections we have discussed the experimental methods concerned with laser plasma physics. Interpretation and understanding of the physical principals underlying such interactions is equally important and challenging. The complexity of laser plasma interactions and the myriad of factors that influence them mean that often some problems simply cannot be deconvolved through merely the consideration of analytical modelling.

A.5.1 Particle in Cell codes

Numerical modelling, particularly using the particle-in-cell method (PIC), provides the plasma physicist with a powerful tool with which the plasma dynamics can be studied in the interpretation of experimental data. For a single particle in the kinetic description of a plasma, the temporally and spatially evolving nature of the velocity distribution function $f(\mathbf{r}, \mathbf{v})$ is given by the Vlasov equation [38].

$$\frac{\partial f}{\partial t} + \mathbf{v} \cdot \frac{\partial f}{\partial x} + q(\mathbf{E} + \frac{\mathbf{v}}{c} \times \mathbf{B}) \cdot \frac{\partial f}{\partial \mathbf{p}} = 0 \tag{A.9}$$

In this form there are 3 spatial and 3 velocity dimensions to consider, making it unfeasable to solve due to the computational demands.

Instead the PIC method introduces macro-particles that represent the particle distribution function. These macro-particles have a finite density and charge attributed to them based on the number of real particles they represent. These macro-particles are mapped onto a simulation grid enabling the density and current to be determined such that Maxwells equations, given below as equations A.10 and A.11, can be solved.

$$\frac{\partial \mathbf{B}}{\partial t} = -\nabla \times \mathbf{E} \tag{A.10}$$

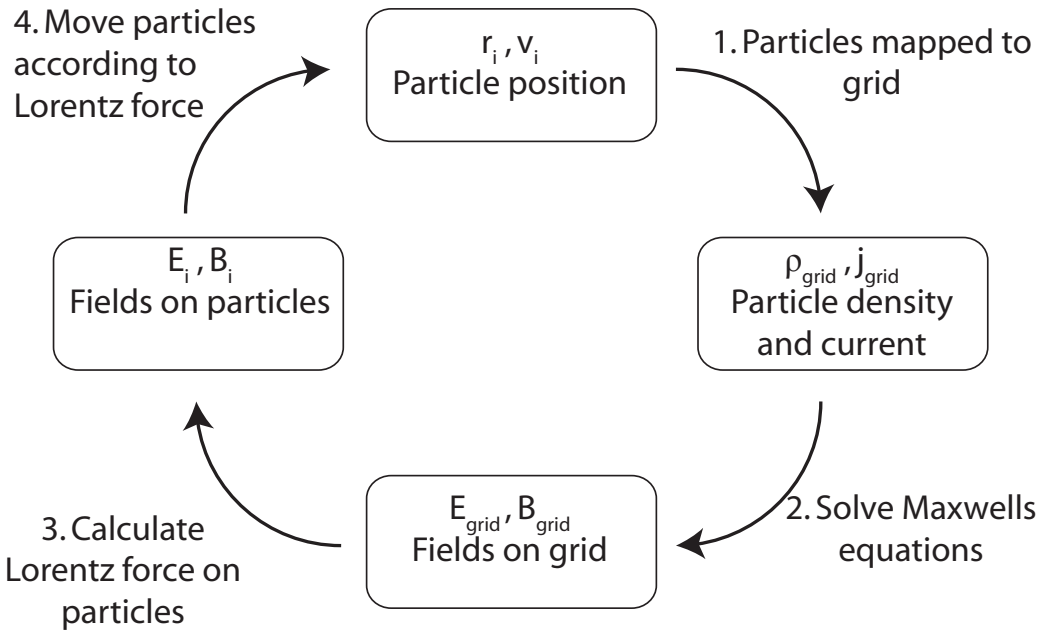

Figure A.19: Schematic diagram showing the PIC algorithm and the steps taken by it for a single iteration.

$$\frac{\partial \mathbf{E}}{\partial t} = c^2 \nabla \times \mathbf{B} - \frac{\mathbf{j}}{\epsilon_0} \tag{A.11}$$

From the integration of Maxwells equations, the electric and magnetic fields are returned for each grid point. These fields influence the particles according to the Lorentz force, and the resulting motion is calculated by the Lorentz equation:

$$\frac{d\mathbf{v}}{dt} = \frac{q}{m}(\mathbf{E} + \mathbf{v} \times \mathbf{B}) \tag{A.12}$$

The final step is then to move the particles according to the Lorentz force and a new distribution of particles with different density and current values on the grid. This process is then repeated for the duration of the simulation according to the algorithm shown schematically in figure A.19. In this way, laser plasma interactions can be simulated numerically in 1D, 2D and 3D geometries with the computational intensity increasing with dimensionality. The PIC code used in the work presented was EPOCH [146], an open source fully relativistic PIC code.

EPOCH has many features that can be added on such as QED and collisional models. The advantage of the code being open-source is that the user can make alterations to tailor it to specific applications. This feature was used in the work presented in chapter 5, where the alterations will be considered in further detail.

A.6 Summary

To summarise, the complexity of intense laser-matter interactions require that multiple diagnostic techniques work in harmony together in order to gain insight into the complex dynamics that are being investigated. An understanding of how intense pulses of light are generated and their key properties are also of key importance to determining the limitations of the experimental conditions and how they impact on the interaction physics that are being probed.

The complexity of the multiple physical processes that occur in such interactions necessitates not only experimental investigations but also numerical modelling and simulation in order to understand the experimental results in the context of the interaction physics that are being probed.

This chapter has given some background into the generation of short intense laser pulses and commonly used diagnostic techniques as well as numerical modelling techniques that are core to the underpinning physics presented in this thesis. Of particular importance are the limitations of each, which will be discussed in more detail in the following chapters.

Bibliography

[1] RJ Gray, DA MacLellan, Bruno Gonzalez-Izquierdo, HW Powell, DC Carroll, CD Murphy, LC Stockhausen, DR Rusby, GG Scott, R Wilson, et al. Azimuthal asymmetry in collective electron dynamics in relativistically transparent laser–foil interactions. *New Journal of Physics*, 16(9):093027, 2014.

[2] Ian Musgrave, Waseem Shaikh, Marco Galimberti, Alexis Boyle, Cristina Hernandez-Gomez, Kate Lancaster, and Robert Heathcote. Picosecond optical parametric chirped pulse amplifier as a preamplifier to generate high-energy seed pulses for contrast enhancement. *Applied Optics*, 49(33):6558–6562, 2010.

[3] Ch Ziener, PS Foster, EJ Divall, CJ Hooker, MHR Hutchinson, AJ Langley, and D Neely. Specular reflectivity of plasma mirrors as a function of intensity, pulse duration, and angle of incidence. *Journal of Applied Physics*, 93(1):768–770, 2003.

[4] WP Leemans, B Nagler, AJ Gonsalves, Cs Toth, K Nakamura, CGR Geddes, E Esarey, CB Schroeder, and SM Hooker. Gev electron beams from a centimetre-scale accelerator. *Nature physics*, 2(10):696–699, 2006.

[5] RA Snavely, MH Key, SP Hatchett, TE Cowan, M Roth, TW Phillips, MA Stoyer, EA Henry, TC Sangster, MS Singh, et al. Intense high-energy proton beams from petawatt-laser irradiation of solids. *Physical Review Letters*, 85(14):2945, 2000.

[6] Daniel Jung. *Ion acceleration from relativistic laser nano-target interaction.* PhD thesis, Ludwig Maximilians University Munich, 2012.

[7] Andrea Macchi, Marco Borghesi, and Matteo Passoni. Ion acceleration by superintense laser-plasma interaction. *Reviews of Modern Physics*, 85(2):751, 2013.

[8] SV Bulanov, T Zh Esirkepov, VS Khoroshkov, AV Kuznetsov, and F Pegoraro. Oncological hadrontherapy with laser ion accelerators. *Physics Letters A*, 299(2):240–247, 2002.

[9] SV Bulanov and VS Khoroshkov. Feasibility of using laser ion accelerators in proton therapy. *Plasma Physics Reports*, 28(5):453–456, 2002.

[10] P Antici, M Migliorati, A Mostacci, L Picardi, L Palumbo, and C Ronsivalle. A compact post-acceleration scheme for laser-generated protons. *Physics of Plasmas (1994-present)*, 18(7):073103, 2011.

[11] A.M. Koehler. Energetic protons from an accelerator may be used to produce radiographs showing unusually high contrast but relatively poor spatial resolution. *Science*, 160(3825):303–304, 1968.

[12] Marco Borghesi, DH Campbell, A Schiavi, MG Haines, O Willi, AJ MacKinnon, P Patel, LA Gizzi, M Galimberti, RJ Clarke, et al. Electric field detection in laser-plasma interaction experiments via the proton imaging technique. *Physics of Plasmas (1994-present)*, 9(5):2214–2220, 2002.

[13] M Borghesi, A Schiavi, DH Campbell, MG Haines, O Willi, AJ MacKinnon, LA Gizzi, M Galimberti, RJ Clarke, and H Ruhl. Proton imaging: a diagnostic for inertial confinement fusion/fast ignitor studies. *Plasma Physics and Controlled Fusion*, 43(12A):A267, 2001.

[14] AJ Mackinnon, PK Patel, RP Town, MJ Edwards, T Phillips, SC Lerner, DW Price, D Hicks, MH Key, S Hatchett, et al. Proton radiography as an electromagnetic field and density perturbation diagnostic. *Review of Scientific Instruments*, 75(10):3531–3536, 2004.

[15] Lorenzo Romagnani, Julien Fuchs, M Borghesi, Patrizio Antici, P Audebert, F Ceccherini, T Cowan, T Grismayer, S Kar, A Macchi, et al. Dynamics of electric fields driving the laser acceleration of multi-mev protons. *Physical Review Letters*, 95(19):195001, 2005.

[16] S Kar, M Borghesi, CA Cecchetti, L Romagnani, F Ceccherini, TV Liseykina, A Macchi, R Jung, J Osterholz, O Willi, et al. Dynamics of charge-displacement channeling in intense laser–plasma interactions. *New Journal of Physics*, 9(11):402, 2007.

[17] L Willingale, AGR Thomas, PM Nilson, MC Kaluza, S Bandyopadhyay, AE Dangor, RG Evans, P Fernandes, MG Haines, C Kamperidis, et al. Proton probe measurement of fast advection of magnetic fields by hot electrons. *Plasma Physics and Controlled Fusion*, 53(12):124026, 2011.

[18] L Romagnani, SV Bulanov, M Borghesi, P Audebert, JC Gauthier, K Löwenbrück, AJ Mackinnon, P Patel, G Pretzler, T Toncian, et al. Observation of collisionless shocks in laser-plasma experiments. *Physical Review Letters*, 101(2):025004, 2008.

[19] Stefano Atzeni and Jürgen Meyer-ter Vehn. *The physics of inertial fusion*. Clarendon Press, 2004.

[20] S Atzeni, A Schiavi, F Califano, F Cattani, F Cornolti, D Del Sarto, TV Liseykina, A Macchi, and F Pegoraro. Fluid and kinetic simulation of inertial confinement fusion plasmas. *Computer Physics Communications*, 169(1):153–159, 2005.

[21] Michael H Key. Status of and prospects for the fast ignition inertial fusion concepta). *Physics of Plasmas (1994-present)*, 14(5):055502, 2007.

[22] VT Tikhonchuk, T Schlegel, C Regan, M Temporal, J-L Feugeas, Ph Nicolaï, and X Ribeyre. Fast ion ignition with ultra-intense laser pulses. *Nuclear Fusion*, 50(4):045003, 2010.

[23] R Kodama, PA Norreys, K Mima, AE Dangor, RG Evans, H Fujita, Y Kitagawa, K Krushelnick, T Miyakoshi, N Miyanaga, et al. Fast heating of ultrahigh-density plasma as a step towards laser fusion ignition. *Nature*, 412(6849):798–802, 2001.

[24] R Kodama, K Mima, H Fujita, Y Kitagawa, T Miyakoshi, N Miyanaga, T Norimatsu, T Shozaki, K Shigemori, A Sunahara, et al. Fast heating of ultrahigh-density plasma as a step towards laser fusion ignition. *Nature*, 412:798–202, 2002.

[25] M Roth, TE Cowan, MH Key, SP Hatchett, C Brown, W Fountain, J Johnson, DM Pennington, RA Snavely, SC Wilks, et al. Fast ignition by intense laser-accelerated proton beams. *Physical Review Letters*, 86(3):436, 2001.

[26] BM Hegelich, D Jung, BJ Albright, JC Fernandez, DC Gautier, C Huang, TJ Kwan, S Letzring, S Palaniyappan, RC Shah, et al. Experimental demonstration of particle energy, conversion efficiency and spectral shape required for ion-based fast ignition. *Nuclear Fusion*, 51(8):083011, 2011.

[27] PK Patel, AJ Mackinnon, MH Key, TE Cowan, ME Foord, M Allen, DF Price, H Ruhl, PT Springer, and R Stephens. Isochoric heating of solid-density matter with an ultrafast proton beam. *Physical Review Letters*, 91(12):125004, 2003.

[28] RA Snavely, B Zhang, K Akli, Z Chen, RR Freeman, P Gu, SP Hatchett, D Hey, J Hill, MH Key, et al. Laser generated proton beam focusing and high temperature isochoric heating of solid matter. *Physics of Plasmas (1994-present)*, 14(9):092703, 2007.

[29] David Andrew MacLellan. *Effects of electrical resistivity on fast electron transport in relativistic laser-solid interactions*. PhD thesis, University of Strathclyde, 2014.

[30] DA MacLellan, DC Carroll, RJ Gray, Nicola Booth, Matthias Burza, MP Desjarlais, F Du, David Neely, HW Powell, APL Robinson, et al.

Tunable mega-ampere electron current propagation in solids by dynamic control of lattice melt. *Physical Review Letters*, 113(18):185001, 2014.

[31] I Spencer, KWD Ledingham, RP Singhal, T McCanny, P McKenna, EL Clark, K Krushelnick, M Zepf, FN Beg, M Tatarakis, et al. Laser generation of proton beams for the production of short-lived positron emitting radioisotopes. *Nuclear Instruments and Methods in Physics Research Section B: Beam Interactions with Materials and Atoms*, 183(3):449–458, 2001.

[32] P McKenna, KWD Ledingham, S Shimizu, JM Yang, L Robson, T McCanny, J Galy, J Magill, RJ Clarke, D Neely, et al. Broad energy spectrum of laser-accelerated protons for spallation-related physics. *Physical Review Letters*, 94(8):084801, 2005.

[33] KWD Ledingham. Laser induced nuclear physics and applications. *Nuclear Physics A*, 752:633–644, 2005.

[34] KWD Ledingham, P McKenna, T McCanny, S Shimizu, JM Yang, L Robson, Jamal Zweit, James M Gillies, J Bailey, GN Chimon, et al. High power laser production of short-lived isotopes for positron emission tomography. *Journal of Physics D: Applied Physics*, 37(16):2341, 2004.

[35] P McKenna, KWD Ledingham, T McCanny, RP Singhal, I Spencer, MIK Santala, FN Beg, K Krushelnick, M Tatarakis, MS Wei, et al. Demonstration of fusion-evaporation and direct-interaction nuclear reactions using high-intensity laser-plasma-accelerated ion beams. *Physical Review Letters*, 91(7):075006, 2003.

[36] Thomas James Morrow Boyd and Jeffrey John Sanderson. *The physics of plasmas*. Cambridge University Press, 2003.

[37] F. F. Chen. Introduction to plasma physics and controlled fusion. *Plasma Physics*, 1984.

[38] Paul Gibbon. *Short pulse laser interactions with matter*. World Scientific Publishing Company, 2004.

[39] B Wolff, H Rottke, D Feldmann, and KH Welge. Multiphoton-ionization of hydrogen atoms in intense laserfields. *Zeitschrift für Physik D Atoms, Molecules and Clusters*, 10(1):35–43, 1988.

[40] G Mainfray and G Manus. Multiphoton ionization of atoms. *Reports on Progress in Physics*, 54(10):1333, 1991.

[41] Maxim V Ammosov, Nikolai B Delone, and Vladimir P Krainov. Tunnel ionization of complex atoms and atomic ions in electromagnetic field. In *1986 Quebec Symposium*, pages 138–141. International Society for Optics and Photonics, 1986.

[42] LV Keldysh. Ionization in the field of a strong electromagnetic wave. *Sov. Phys. JETP*, 20(5):1307–1314, 1965.

[43] Andrea Macchi. *A Superintense Laser-Plasma Interaction Theory Primer*. Springer Science & Business Media, 2013.

[44] P Sprangle, E Esarey, J Krall, and G Joyce. Propagation and guiding of intense laser pulses in plasmas. *Physical Review Letters*, 69(15):2200, 1992.

[45] SC Wilks, WL Kruer, M Tabak, and AB Langdon. Absorption of ultra-intense laser pulses. *Physical Review Letters*, 69(9):1383, 1992.

[46] M Tabak, J Hammer, M E Glinsky, W. L Kruer, SC Wilks, J Woodworth, M Campbell, MD Perry, and RJ Mason. Ignition and high gain with ultrapowerful lasers*. *Physics of Plasmas (1994-present)*, 1(5):1626–1634, 1994.

[47] RJ Gray, DC Carroll, XH Yuan, CM Brenner, M Burza, M Coury, KL Lancaster, XX Lin, YT Li, D Neely, et al. Laser pulse propagation and enhanced energy coupling to fast electrons in dense plasma gradients. *New Journal of Physics*, 16(11):113075, 2014.

[48] Scott C Wilks and William L Kruer. Absorption of ultrashort, ultra-intense laser light by solids and overdense plasmas. *Quantum Electronics, IEEE Journal of*, 33(11):1954–1968, 1997.

[49] AA Andreev, K Yu Platonov, T Okada, and S Toraya. Nonlinear absorption of a short intense laser pulse in a nonuniform plasma. *Physics of Plasmas (1994-present)*, 10(1):220–226, 2003.

[50] P McKenna, DC Carroll, Olle Lundh, F Nürnberg, K Markey, S Bandyopadhyay, D Batani, RG Evans, R Jafer, S Kar, et al. Effects of front surface plasma expansion on proton acceleration in ultraintense laser irradiation of foil targets. *Laser and Particle Beams*, 26(04):591–596, 2008.

[51] M Borghesi, AJ MacKinnon, L Barringer, R Gaillard, LA Gizzi, C Meyer, O Willi, A Pukhov, and J Meyer-ter Vehn. Relativistic channeling of a picosecond laser pulse in a near-critical preformed plasma. *Physical Review Letters*, 78(5):879, 1997.

[52] Xiaofang Wang, Mohan Krishnan, Ned Saleh, Haiwen Wang, and Donald Umstadter. Electron acceleration and the propagation of ultrashort high-intensity laser pulses in plasmas. *Physical Review Letters*, 84(23):5324, 2000.

[53] V Malka, J Faure, JR Marques, F Amiranoff, C Courtois, Z Najmudin, K Krushelnick, MR Salvati, and AE Dangor. Interaction of ultraintense laser pulses with an underdense, preformed plasma channel. *Plasma Science, IEEE Transactions on*, 28(4):1078–1083, 2000.

[54] APL Robinson, M Zepf, S Kar, RG Evans, and C Bellei. Radiation pressure acceleration of thin foils with circularly polarized laser pulses. *New journal of Physics*, 10(1):013021, 2008.

[55] N Naseri, SG Bochkarev, and W Rozmus. Self-channelling of relativistic laser pulses in large-scale underdense plasmas. *Physics of Plasmas (1994-present)*, 17(3):033107, 2010.

[56] A Pukhov and J Meyer-ter Vehn. Relativistic magnetic self-channeling of light in near-critical plasma: three-dimensional particle-in-cell simulation. *Physical Review Letters*, 76(21):3975, 1996.

[57] F Cattani, A Kim, D Anderson, and M Lisak. Threshold of induced transparency in the relativistic interaction of an electromagnetic wave with overdense plasmas. *Physical Review E*, 62(1):1234, 2000.

[58] Sasi Palaniyappan, B Manuel Hegelich, Hui-Chun Wu, Daniel Jung, Donald C Gautier, Lin Yin, Brian J Albright, Randall P Johnson, Tsutomu Shimada, Samuel Letzring, et al. Dynamics of relativistic transparency and optical shuttering in expanding overdense plasmas. *Nature Physics*, 8(10):763–769, 2012.

[59] William L Kruer. *The physics of laser plasma interactions*. Reading, MA (US); Addison-Wesley Publishing Co., 1988.

[60] TE Stringer. Electrostatic instabilities in current-carrying and counter-streaming plasmas. *Journal of Nuclear Energy. Part C, Plasma Physics, Accelerators, Thermonuclear Research*, 6(3):267, 1964.

[61] BJ Albright, L Yin, Kevin J Bowers, BM Hegelich, KA Flippo, TJT Kwan, and JC Fernandez. Relativistic buneman instability in the laser breakout afterburner. *Physics of Plasmas (1994-present)*, 14(9):094502, 2007.

[62] David H Sharp. An overview of rayleigh-taylor instability. *Physica D: Nonlinear Phenomena*, 12(1):3–18, 1984.

[63] Erich S Weibel. Spontaneously growing transverse waves in a plasma due to an anisotropic velocity distribution. *Physical Review Letters*, 2(3):83, 1959.

[64] Stefano Atzeni and Jürgen Meyer-ter Vehn. *The Physics of Inertial Fusion: BeamPlasma Interaction, Hydrodynamics, Hot Dense Matter: BeamPlasma Interaction, Hydrodynamics, Hot Dense Matter*, volume 125. Oxford University Press, 2004.

[65] CAJ Palmer, J Schreiber, SR Nagel, NP Dover, C Bellei, FN Beg, S Bott, RJ Clarke, AE Dangor, SM Hassan, et al. Rayleigh-taylor instability of an ultrathin foil accelerated by the radiation pressure of an intense laser. *Physical Review Letters*, 108(22):225002, 2012.

[66] AJ Cole, JD Kilkenny, PT Rumsby, RG Evans, CJ Hooker, and MH Key. Measurement of rayleigh–taylor instability in a laser-accelerated target. *Nature*, 299:329 – 331, 1982.

[67] Sanwal P Sarraf, Edward A Williams, and Leonard M Goldman. Ion-ion two-stream instability in multispecies laser-produced plasma. *Physical Review A*, 27(4):2110, 1983.

[68] Thomas H Stix. *Waves in plasmas*. Springer Science & Business Media, 1992.

[69] T Tajima and JM Dawson. Laser electron accelerator. *Physical Review Letters*, 43(4):267, 1979.

[70] EL Clark, K Krushelnick, M Zepf, FN Beg, M Tatarakis, A Machacek, MIK Santala, I Watts, PA Norreys, and AE Dangor. Energetic heavy-ion and proton generation from ultraintense laser-plasma interactions with solids. *Physical Review Letters*, 85(8):1654, 2000.

[71] A Maksimchuk, S Gu, K Flippo, D Umstadter, and V Yu Bychenkov. Forward ion acceleration in thin films driven by a high-intensity laser. *Physical Review Letters*, 84(18):4108, 2000.

[72] Matthew Allen, Pravesh K Patel, Andrew Mackinnon, Dwight Price, Scott Wilks, and Edward Morse. Direct experimental evidence of back-surface ion acceleration from laser-irradiated gold foils. *Physical Review Letters*, 93(26):265004, 2004.

[73] J Fuchs, Y Sentoku, Stefan Karsch, J Cobble, P Audebert, Andreas Kemp, A Nikroo, P Antici, E Brambrink, A Blazevic, et al. Comparison of laser ion

acceleration from the front and rear surfaces of thin foils. *Physical Review Letters*, 94(4):045004, 2005.

[74] J Fuchs, Y Sentoku, E dHumières, TE Cowan, J Cobble, P Audebert, A Kemp, A Nikroo, P Antici, E Brambrink, et al. Comparative spectra and efficiencies of ions laser-accelerated forward from the front and rear surfaces of thin solid foils. *Physics of Plasmas (1994-present)*, 14(5):053105, 2007.

[75] AR Bell, JR Davies, S Guerin, and H Ruhl. Fast-electron transport in high-intensity short-pulse laser-solid experiments. *Plasma Physics and Controlled Fusion*, 39(5):653, 1997.

[76] JJ Santos, F Amiranoff, SD Baton, L Gremillet, M Koenig, E Martinolli, M Rabec Le Gloahec, C Rousseaux, D Batani, A Bernardinello, et al. Fast electron transport in ultraintense laser pulse interaction with solid targets by rear-side self-radiation diagnostics. *Physical Review Letters*, 89(2):025001, 2002.

[77] JR Davies, AR Bell, MG Haines, and SM Guerin. Short-pulse high-intensity laser-generated fast electron transport into thick solid targets. *Physical Review E*, 56(6):7193, 1997.

[78] APL Robinson, DJ Strozzi, JR Davies, L Gremillet, JJ Honrubia, T Johzaki, RJ Kingham, M Sherlock, and AA Solodov. Theory of fast electron transport for fast ignition. *Nuclear Fusion*, 54(5):054003, 2014.

[79] Matteo Passoni, Luca Bertagna, and Alessandro Zani. Target normal sheath acceleration: theory, comparison with experiments and future perspectives. *New Journal of Physics*, 12(4):045012, 2010.

[80] AJ Mackinnon, Y Sentoku, PK Patel, DW Price, S Hatchett, MH Key, C Andersen, R Snavely, and RR Freeman. Enhancement of proton acceleration by hot-electron recirculation in thin foils irradiated by ultraintense laser pulses. *Physical Review Letters*, 88(21):215006, 2002.

[81] SJ Gitomer, RD Jones, F Begay, AW Ehler, JF Kephart, and R Kristal. Fast ions and hot electrons in the laser–plasma interaction. *Physics of Fluids (1958-1988)*, 29(8):2679–2688, 1986.

[82] SC Wilks, AB Langdon, TE Cowan, M Roth, M Singh, S Hatchett, MH Key, D Pennington, A MacKinnon, and RA Snavely. Energetic proton generation in ultra-intense laser–solid interactions. *Physics of Plasmas (1994-present)*, 8(2):542–549, 2001.

[83] P Mora. Plasma expansion into a vacuum. *Physical Review Letters*, 90(18):185002, 2003.

[84] VT Tikhonchuk. Interaction of a beam of fast electrons with solids. *Physics of Plasmas (1994-present)*, 9(4):1416–1421, 2002.

[85] M Passoni, VT Tikhonchuk, M Lontano, and V Yu Bychenkov. Charge separation effects in solid targets and ion acceleration with a two-temperature electron distribution. *Physical Review E*, 69(2):026411, 2004.

[86] J Fuchs, P Antici, E dHumières, E Lefebvre, M Borghesi, E Brambrink, CA Cecchetti, Malte Kaluza, Victor Malka, M Manclossi, et al. Laser-driven proton scaling laws and new paths towards energy increase. *Nature Physics*, 2(1):48–54, 2006.

[87] R.J. Gray. *On Mechanisms of Laser-Coupling to Fast Electrons in Ultraintense Laser-Solid Interactions*. PhD thesis, University of Strathclyde, 2013.

[88] L Robson, PT Simpson, RJ Clarke, KWD Ledingham, F Lindau, O Lundh, T McCanny, P Mora, D Neely, C-G Wahlström, et al. Scaling of proton acceleration driven by petawatt-laser–plasma interactions. *Nature Physics*, 3(1):58–62, 2007.

[89] TE Cowan, J Fuchs, H Ruhl, A Kemp, P Audebert, M Roth, R Stephens, I Barton, A Blazevic, E Brambrink, et al. Ultralow emittance, multi-mev proton beams from a laser virtual-cathode plasma accelerator. *Physical Review Letters*, 92(20):204801, 2004.

[90] M Roth, E Brambrink, P Audebert, A Blazevic, R Clarke, J Cobble, TE Cowan, J Fernandez, J Fuchs, M Geissel, et al. Laser accelerated ions and electron transport in ultra-intense laser matter interaction. *Laser and Particle Beams*, 23(01):95–100, 2005.

[91] M Borghesi, AJ Mackinnon, DH Campbell, DG Hicks, S Kar, PK Patel, D Price, L Romagnani, A Schiavi, and O Willi. Multi-mev proton source investigations in ultraintense laser-foil interactions. *Physical Review Letters*, 92(5):055003, 2004.

[92] K Markey, P McKenna, CM Brenner, DC Carroll, MM Günther, K Harres, S Kar, K Lancaster, F Nürnberg, MN Quinn, et al. Spectral enhancement in the double pulse regime of laser proton acceleration. *Physical Review Letters*, 105(19):195008, 2010.

[93] CM Brenner, APL Robinson, K Markey, RHH Scott, RJ Gray, M Rosinski, O Deppert, J Badziak, D Batani, JR Davies, et al. High energy conversion efficiency in laser-proton acceleration by controlling laser-energy deposition onto thin foil targets. *Applied Physics Letters*, 104(8):081123, 2014.

[94] GG Scott, JS Green, V Bagnoud, C Brabetz, CM Brenner, DC Carroll, DA MacLellan, APL Robinson, M Roth, C Spindloe, et al. Multi-pulse enhanced laser ion acceleration using plasma half cavity targets. *Applied Physics Letters*, 101(2):024101, 2012.

[95] Andrea Macchi, Silvia Veghini, and Francesco Pegoraro. light sail acceleration reexamined. *Physical Review Letters*, 103(8):085003, 2009.

[96] T Esirkepov, M Borghesi, SV Bulanov, G Mourou, and T Tajima. Highly efficient relativistic-ion generation in the laser-piston regime. *Physical Review Letters*, 92(17):175003, 2004.

[97] O Klimo, J Psikal, J Limpouch, and VT Tikhonchuk. Monoenergetic ion beams from ultrathin foils irradiated by ultrahigh-contrast circularly polar-

ized laser pulses. *Physical Review Special Topics-Accelerators and Beams*, 11(3):031301, 2008.

[98] APL Robinson, Paul Gibbon, M Zepf, S Kar, RG Evans, and C Bellei. Relativistically correct hole-boring and ion acceleration by circularly polarized laser pulses. *Plasma Physics and Controlled Fusion*, 51(2):024004, 2009.

[99] APL Robinson, DH Kwon, and K Lancaster. Hole-boring radiation pressure acceleration with two ion species. *Plasma Physics and Controlled Fusion*, 51(9):095006, 2009.

[100] Emmanuel dHumières, Erik Lefebvre, Laurent Gremillet, and Victor Malka. Proton acceleration mechanisms in high-intensity laser interaction with thin foils. *Physics of Plasmas (1994-present)*, 12(6):062704, 2005.

[101] Charlotte AJ Palmer, NP Dover, I Pogorelsky, M Babzien, GI Dudnikova, M Ispiriyan, MN Polyanskiy, J Schreiber, P Shkolnikov, V Yakimenko, et al. Monoenergetic proton beams accelerated by a radiation pressure driven shock. *Physical Review Letters*, 106(1):014801, 2011.

[102] S Kar, KF Kakolee, B Qiao, A Macchi, M Cerchez, D Doria, M Geissler, P McKenna, D Neely, J Osterholz, et al. Ion acceleration in multispecies targets driven by intense laser radiation pressure. *Physical Review Letters*, 109(18):185006, 2012.

[103] B Qiao, M Zepf, M Borghesi, and M Geissler. Stable gev ion-beam acceleration from thin foils by circularly polarized laser pulses. *Physical Review Letters*, 102(14):145002, 2009.

[104] SV Bulanov, T Esirkepov, P Migliozzi, F Pegoraro, T Tajima, and F Terranova. Neutrino oscillation studies with laser-driven beam dump facilities. *Nuclear Instruments and Methods in Physics Research Section A: Accelerators, Spectrometers, Detectors and Associated Equipment*, 540(1):25–41, 2005.

[105] Hiroyuki Daido, Mamiko Nishiuchi, and Alexander S Pirozhkov. Review of laser-driven ion sources and their applications. *Reports on Progress in Physics*, 75(5):056401, 2012.

[106] F Pegoraro and SV Bulanov. Photon bubbles and ion acceleration in a plasma dominated by the radiation pressure of an electromagnetic pulse. *Physical Review Letters*, 99(6):065002, 2007.

[107] Sergei V Bulanov, Timur Zh Esirkepov, Francesco Pegoraro, and Marco Borghesi. On the ion acceleration by high power electromagnetic waves in the radiation pressure dominated regime. *Comptes Rendus Physique*, 10(2):216–226, 2009.

[108] F Pegoraro and SV Bulanov. Nonlinear relativistic dynamics of a plasma foil driven by radiation pressure. In *AIP Conf. Proc*, volume 1153, pages 263–73, 2009.

[109] Lin Yin, BJ Albright, BM Hegelich, and JC Fernández. Gev laser ion acceleration from ultrathin targets: The laser break-out afterburner. *Laser and Particle Beams*, 24(02):291–298, 2006.

[110] L Yin, BJ Albright, BM Hegelich, Kevin J Bowers, KA Flippo, TJT Kwan, and JC Fernández. Monoenergetic and gev ion acceleration from the laser breakout afterburner using ultrathin targets. *Physics of Plasmas (1994-present)*, 14(5):056706, 2007.

[111] L Yin, BJ Albright, KJ Bowers, D Jung, JC Fernández, and BM Hegelich. Three-dimensional dynamics of breakout afterburner ion acceleration using high-contrast short-pulse laser and nanoscale targets. *Physical Review Letters*, 107(4):045003, 2011.

[112] L Yin, BJ Albright, D Jung, RC Shah, S Palaniyappan, KJ Bowers, Andreas Henig, JC Fern, Björn M Hegelich, et al. Break-out afterburner ion acceleration in the longer laser pulse length regime. *Physics of Plasmas (1994-present)*, 18(6):063103, 2011.

[113] BJ Albright, L Yin, BM Hegelich, Kevin J Bowers, TJT Kwan, and JC Fernández. Theory of laser acceleration of light-ion beams from interaction of ultrahigh-intensity lasers with layered targets. *Physical Review Letters*, 97(11):115002, 2006.

[114] D Jung, BJ Albright, L Yin, DC Gautier, R Shah, S Palaniyappan, S Letzring, B Dromey, HC Wu, T Shimada, et al. Beam profiles of proton and carbon ions in the relativistic transparency regime. *New Journal of Physics*, 15(12):123035, 2013.

[115] D Jung, L Yin, BJ Albright, DC Gautier, S Letzring, B Dromey, M Yeung, Rainer Hörlein, R Shah, S Palaniyappan, et al. Efficient carbon ion beam generation from laser-driven volume acceleration. *New Journal of Physics*, 15(2):023007, 2013.

[116] Daniel Jung, L Yin, DC Gautier, H-C Wu, S Letzring, B Dromey, R Shah, S Palaniyappan, T Shimada, RP Johnson, et al. Laser-driven 1 gev carbon ions from preheated diamond targets in the break-out afterburner regime. *Physics of Plasmas (1994-present)*, 20(8):083103, 2013.

[117] Andreas Henig, Daniel Kiefer, K Markey, DC Gautier, KA Flippo, S Letzring, RP Johnson, T Shimada, L Yin, BJ Albright, et al. Enhanced laser-driven ion acceleration in the relativistic transparency regime. *Physical Review Letters*, 103(4):045002, 2009.

[118] XQ Yan, T Tajima, M Hegelich, L Yin, and Dietrich Habs. Theory of laser ion acceleration from a foil target of nanometer thickness. *Applied Physics B*, 98(4):711–721, 2010.

[119] Brian J Albright, Lin Yin, Bjoorn M Hegelich, Kevin J Bowers, Chengkun Huang, A Henig, JC Fernández, KA Flippo, SA Gaillard, TJT Kwan, et al. Ultraintense laser interaction with nanoscale targets: a simple model for layer expansion and ion acceleration. In *Journal of Physics: Conference Series*, volume 244, page 042022. IOP Publishing, 2010.

[120] J Denavit. Absorption of high-intensity subpicosecond lasers on solid density targets. *Physical Review Letters*, 69(21):3052, 1992.

[121] Luís O Silva, Michael Marti, Jonathan R Davies, Ricardo A Fonseca, Chuang Ren, Frank S Tsung, and Warren B Mori. Proton shock acceleration in laser-plasma interactions. *Physical Review Letters*, 92(1):015002, 2004.

[122] Andrea Macchi, Federica Cattani, Tatiana V Liseykina, and Fulvio Cornolti. Laser acceleration of ion bunches at the front surface of overdense plasmas. *Physical Review Letters*, 94(16):165003, 2005.

[123] Dan Haberberger, Sergei Tochitsky, Frederico Fiuza, Chao Gong, Ricardo A Fonseca, Luis O Silva, Warren B Mori, and Chan Joshi. Collisionless shocks in laser-produced plasma generate monoenergetic high-energy proton beams. *Nature Physics*, 8(1):95–99, 2012.

[124] Andreas Henig, Daniel Kiefer, Michael Geissler, Sergey G Rykovanov, R Ramis, Rainer Hörlein, Jens Osterhoff, Zs Major, Laszlo Veisz, Stefan Karsch, et al. Laser-driven shock acceleration of ion beams from spherical mass-limited targets. *Physical Review Letters*, 102(9):095002, 2009.

[125] F Fiuza, A Stockem, E Boella, RA Fonseca, LO Silva, D Haberberger, S Tochitsky, C Gong, WB Mori, and C Joshi. Laser-driven shock acceleration of monoenergetic ion beams. *Physical Review Letters*, 109(21):215001, 2012.

[126] RA Cairns, R Bingham, P Norreys, and R Trines. Laminar shocks in high power laser plasma interactions. *Physics of Plasmas (1994-present)*, 21(2):022112, 2014.

[127] Gerard A Mourou, Toshiki Tajima, and Sergei V Bulanov. Optics in the relativistic regime. *Reviews of Modern Physics*, 78(2):309, 2006.

[128] CN Danson, PA Brummitt, RJ Clarke, JL Collier, B Fell, AJ Frackiewicz, S Hancock, S Hawkes, C Hernandez-Gomez, P Holligan, et al. Vul-

can petawattan ultra-high-intensity interaction facility. *Nuclear Fusion*, 44(12):S239, 2004.

[129] C. Webb S. Hooker. *Laser Physics*. Oxford University Press, 2010.

[130] I_N Ross, P Matousek, M Towrie, AJ Langley, and JL Collier. The prospects for ultrashort pulse duration and ultrahigh intensity using optical parametric chirped pulse amplifiers. *Optics Communications*, 144(1):125–133, 1997.

[131] B Dromey, S Kar, M Zepf, and P Foster. The plasma mirrora subpicosecond optical switch for ultrahigh power lasers. *Review of Scientific Instruments*, 75(3):645–649, 2004.

[132] C Thaury, F Quéré, J-P Geindre, A Levy, T Ceccotti, P Monot, M Bougeard, F Réau, P dOliveira, P Audebert, et al. Plasma mirrors for ultrahigh-intensity optics. *Nature Physics*, 3(6):424–429, 2007.

[133] CN Danson, PA Brummitt, RJ Clarke, JL Collier, B Fell, AJ Frackiewicz, S Hawkes, C Hernandez-Gomez, P Holligan, MHR Hutchinson, et al. Vulcan petawatt: Design, operation and interactions at 5× 1020 wcm- 2. *Laser and Particle Beams*, 23(01):87–93, 2005.

[134] Joseph John Thomson. Bakerian lecture: Rays of positive electricity. *Proceedings of the Royal Society of London. Series A, Containing Papers of a Mathematical and Physical Character*, pages 1–20, 1913.

[135] DC Carroll, P Brummitt, D Neely, Filip Lindau, Olle Lundh, C-G Wahlström, and P McKenna. A modified thomson parabola spectrometer for high resolution multi-mev ion measurementsapplication to laser-driven ion acceleration. *Nuclear Instruments and Methods in Physics Research Section A: Accelerators, Spectrometers, Detectors and Associated Equipment*, 620(1):23–27, 2010.

[136] D Gwynne, S Kar, D Doria, H Ahmed, M Cerchez, J Fernandez, RJ Gray, JS Green, F Hanton, DA MacLellan, et al. Modified thomson spectrome-

ter design for high energy, multi-species ion sources. *Review of Scientific Instruments*, 85(3):033304, 2014.

[137] Y Amemiya and J Miyahara. Imaging plate illuminates many fields. *Nature*, 336(6194):89–90, 1988.

[138] Kar S Doria, D and Kakolee K. Calibration of image plate response to energetic carbon ions. *CLF Annual Report*, 2010.

[139] A Mančić, J Fuchs, P Antici, SA Gaillard, and P Audebert. Absolute calibration of photostimulable image plate detectors used as (0.5–20mev) high-energy proton detectors. *Review of Scientific Instruments*, 79(7):073301, 2008.

[140] F Nürnberg, M Schollmeier, E Brambrink, A Blažević, DC Carroll, K Flippo, DC Gautier, M Geißel, K Harres, BM Hegelich, et al. Radiochromic film imaging spectroscopy of laser-accelerated proton beams. *Review of Scientific Instruments*, 80(3):033301, 2009.

[141] Markus Roth. The diagnostics of ultra-short pulse laser-produced plasma. *Journal of Instrumentation*, 6(09):R09001, 2011.

[142] RJ Clarke, PT Simpson, S Kar, JS Green, C Bellei, DC Carroll, B Dromey, S Kneip, K Markey, P McKenna, et al. Nuclear activation as a high dynamic range diagnostic of laser–plasma interactions. *Nuclear Instruments and Methods in Physics Research Section a: Accelerators, Spectrometers, Detectors and Associated Equipment*, 585(3):117–120, 2008.

[143] James F Ziegler, MD Ziegler, and JP Biersack. Srim–the stopping and range of ions in matter (2010). *Nuclear Instruments and Methods in Physics Research Section B: Beam Interactions with Materials and Atoms*, 268(11):1818–1823, 2010.

[144] Eugene Hecht. *Optics, 4th.* Addison-Wesley, San Francisco, 2002.

[145] R Benattar, C Popovics, and R Sigel. Polarized light interferometer for laser fusion studies. *Review of Scientific Instruments*, 50(12):1583–1586, 1979.

[146] Christopher S Brady and TD Arber. An ion acceleration mechanism in laser illuminated targets with internal electron density structure. *Plasma Physics and Controlled Fusion*, 53(1):015001, 2011.

[147] Andrea Macchi, Silvia Veghini, Tatyana V Liseykina, and Francesco Pegoraro. Radiation pressure acceleration of ultrathin foils. *New Journal of Physics*, 12(4):045013, 2010.

[148] V A Vshivkov, N M Naumova, F Pegoraro, and SV Bulanov. Nonlinear electrodynamics of the interaction of ultra-intense laser pulses with a thin foil. *Physics of Plasmas (1994-present)*, 5(7):2727–2741, 1998.

[149] GG Scott, V Bagnoud, C Brabetz, RJ Clarke, JS Green, RI Heathcote, HW Powell, B Zielbauer, TD Arber, P McKenna, et al. Optimization of plasma mirror reflectivity and optical quality using double laser pulses. *New Journal of Physics*, 17(3):033027, 2015.

[150] NP Dover, MJV Streeter, CAJ Palmer, H Ahmed, B Albertazzi, M Borghesi, DC Carroll, J Fuchs, R Heathcote, P Hilz, et al. Buffered spectrally-peaked proton beams in the relativistic-transparency regime. *arXiv preprint arXiv:1406.3540*, 2014.

[151] Andrea Sgattoni, Stefano Sinigardi, Luca Fedeli, Francesco Pegoraro, and Andrea Macchi. Laser-driven rayleigh-taylor instability: Plasmonic effects and three-dimensional structures. *Physical Review E*, 91(1):013106, 2015.

[152] Antoine Bret, Anne Stockem, Frederico Fiuza, Charles Ruyer, Laurent Gremillet, Ramesh Narayan, and LO Silva. Collisionless shock formation, spontaneous electromagnetic fluctuations, and streaming instabilities. *Physics of Plasmas (1994-present)*, 20(4):042102, 2013.

[153] A Stockem, F Fiuza, A Bret, RA Fonseca, and LO Silva. Exploring the nature of collisionless shocks under laboratory conditions. *Scientific Reports*, 4, 2014.

[154] Zs Lecz and A Andreev. Shock wave acceleration of protons in inhomogeneous plasma interacting with ultrashort intense laser pulses. *Physics of Plasmas (1994-present)*, 22(4):043103, 2015.

[155] C Hernandez-Gomez, SP Blake, O Chekhlov, RJ Clarke, AM Dunne, M Galimberti, S Hancock, R Heathcote, P Holligan, A Lyachev, et al. The vulcan 10 pw project. In *Journal of Physics: Conference Series*, volume 244, page 032006. IOP Publishing, 2010.

[156] C Hernandez-Gomez, JL Collier, D Canny, O Chekhlov, RJ Clarke, M Dunne, M Galimberti, S Hancock, R Heathcote, P Holligan, et al. The vulcan 10 pw opcpa project. *CLF Annual Report*, 2007:210–1, 2006.

[157] J-P Chambaret, O Chekhlov, G Cheriaux, J Collier, R Dabu, P Dombi, AM Dunne, K Ertel, P Georges, J Hebling, et al. Extreme light infrastructure: laser architecture and major challenges. In *SPIE Photonics Europe*, pages 77211D–77211D. International Society for Optics and Photonics, 2010.

[158] Georg Korn, Bruno LeGarrec, and Bedrich Rus. Eli extreme light infrastructure science and technology with ultra-intense lasers. In *CLEO: Science and Innovations*, pages CTu2D–7. Optical Society of America, 2013.

[159] Gérard Mourou and Toshiki Tajima. The extreme light infrastructure: optics next horizon. *Optics and Photonics News*, 22(7):47–51, 2011.